
**Constructing Two-Dimensional Molecular Networks
On Metal and Semiconducting Surfaces**

A scanning tunneling microscopy study

A Dissertation Submitted to the Faculty of Graduate Studies
Lakehead University, Thunder Bay, Ontario, Canada

By

Renjie Liu

Submitted in partial fulfillment of requirements for the degree of
Doctor of Philosophy in Chemistry

Supervised by

Dr. Mark Gallagher

Lakehead University

Thunder Bay, Ontario, Canada, 2019

Renjie Liu © 2019

Statement of Originality

This statement is to certify that the all the work presented in this thesis is Renjie Liu's own original work and has not been previously submitted for a degree or diploma at any other higher education institution. The experimental part of this thesis (Chapters 4 to 6) is based upon published or to-be-published works, in which Renjie Liu was either first author or part of a collaboration.

The role of Renjie Liu in each work can be concluded as following:

All experimental procedures, from sample preparation, pre-process to molecular deposition were all planned and carried out by Renjie Liu.

The majority of the data analysis (STM data) was done by Renjie Liu with contribution from one of the summer students, Max Yuan and current graduate student Davide Marchese.

Theoretical calculations, namely the DFT simulation used in the study on the “Adsorption of TIPT on Si(111) $\sqrt{3}\times\sqrt{3}R30^\circ$ -Ag and Ag(111)” in Chapter 5, have been performed in collaboration with Dr. Robert Mawhinney. The role of Renjie Liu was to provide the initial structures and experimental data, apply the kinetic model to these data, and control the adherence of the calculations to the experimental results.

The used molecular precursors were synthesized by collaborators from The Perepichka Research Group in the Department of Chemistry at McGill University.

Abstract

The synthesis of two-dimensional organic nanostructures on metal and semiconducting surfaces is studied under ultra-high vacuum (UHV) conditions. Three halogenated organic molecules are investigated using scanning tunneling microscopy (STM) on both metal and semiconducting substrates.

The first system studied is the adsorption of brominated tetrathienoanthracene (TBTTA) molecules onto the Si(111) $\sqrt{3}\times\sqrt{3}$ R30°-Ag (Si(111) $\sqrt{3}$ -Ag) surface at room temperature. STM images reveal that at low coverage, the molecules readily migrate to step edges and defects in the $\sqrt{3}$ overlayer. With increasing coverage, the molecules eventually form compact supramolecular structures. At higher coverage (0.4 - 0.6 monolayers), the spatial extent of the supramolecular structures is often limited by defects in the underlying $\sqrt{3}$ layer. Our results suggest that the $\sqrt{3}$ -Ag surface provides a relatively inert substrate for the adsorption of TBTTA molecules, and that the supramolecular structures are held together by relatively weak intermolecular forces.

The second organic molecule investigated is 2,4,6-tris(4-iodophenyl)-1,3,5-triazine (TIPT). Molecules are deposited onto two related surfaces, Ag(111) and Si(111) $\sqrt{3}$ -Ag. On the Ag(111) surface, TIPT molecules dehalogenate spontaneously upon deposition and form organometallic structures at room temperature. Gentle annealing at ~ 100 °C leads to a more ordered molecular network characterized almost exclusively by hexagons and polymerization was confirmed after further annealing at ~ 135 °C. On the Si(111) $\sqrt{3}$ -Ag surface TIPT molecules remain largely intact and readily diffuse to step edges and defects in the $\sqrt{3}$ overlayer. At low coverage, most images display regularly spaced “fuzzy lines” which indicate molecular diffusion at room temperature. At higher coverage (0.4 – 0.8 monolayers), supramolecular domains are formed. The geometry of the cell is similar to an energy optimized 2-d free-standing TIPT layer determined by DFT indicating that de-halogenation does not occur on the Si(111) $\sqrt{3}$ -Ag surface at

room temperature and that the supramolecular domains are characterized by zig-zag rows of intact monomers held together primarily by I \cdots H hydrogen-like bonding.

Finally, the adsorption of 2,6,10-tribromo-4,8,12-trioxa-3a²-azadibenzo[cd,mn]pyrene (TBTANG) molecules is detailed on both Au(111) and Si(111) $\sqrt{3}$ -Ag surfaces. Dosing TBTANG molecules onto a Au(111) surface at room temperature leads to the self-assembly of intact molecules while deposition onto a hot Au(111) surface yields a complete polymer layer. On the Si(111) $\sqrt{3}$ -Ag surface the molecules display high mobility. With increasing coverage, TBTANG exhibits long-range self-assembly of intact molecules. As the coverage approaches one monolayer, the self-assembled layer extends over the entire surface. Defects in the $\sqrt{3}$ -Ag substrate affect the integrity of domains, but do not limit the size. Preliminary annealing experiments do not lead to polymerization of the TBTANG layer. Rather, annealing at $\sim 90^\circ\text{C}$ leads to disordered regions which nucleate primarily at step edges.

Acknowledgements

Looking back on the past seven years, there are many people I would like to thank for their help, advice and encouragement throughout my studies at Lakehead.

Firstly, I would like to sincerely thank my supervisor, Dr. Mark Gallagher, for giving me the opportunity to work on this interesting project. His generous support, helpful guidance, curiosity for knowledge, in-depth expertise, enthusiasm for science, and insight to scientific questions made a considerable impact on my success during my graduate studies. He gave me the freedom to explore new ideas while keeping me focused on my goals.

Many thanks should go to my co-supervisor, Dr. Alla Reznik. She not only supported my academic life, but also provided me a chance to be exposed to an industrial environment. She helped me getting the understanding on how to convert the experience in lab to real life applications.

Dr. Robert Mawhinney deserves my thanks for helpful discussions and calculations concerning some of the more theoretical aspects of this project.

I would also like to thank our technician Giovanni Decrescenzo. He has made my TA job easier and always got a solution whenever we need technical support from him.

Thanks to all colleagues, summer students and friends who worked with me and helped me during this period. Although too many to name individually, they all deserve recognition for their help and friendship.

At last I get to my family. My most special thanks go to my wife, Lu Li, with whom I'm sharing my life. You have always listened to my complaints and been the voice of reason when everything got too much for me. You are simply too important for me. Thanks to my Dad, and parents in law who have always been ready to support me during good time and bad time.

Unfortunately my Mum didn't get to see me complete my PhD, but I know how proud she was of me, and that she would be telling everyone she met about it. I will bring her in my heart forever.

*God made the bulk;
the surface was invented by the devil.*

- Wolfgang Pauli

Table of Contents

<i>Statement of Originality</i>	<i>ii</i>
<i>Abstract</i>	<i>iii</i>
<i>Acknowledgements</i>	<i>v</i>
<i>Table of Contents</i>	<i>viii</i>
Chapter 1 Introduction	1
Chapter 2 Background	7
2.1 Substrates	8
2.1.1 Ag(111) and Au(111)	8
2.1.2 Silicon Crystallography	9
2.1.3 Si (111) $\sqrt{3}\times\sqrt{3}$ R30°- Ag Surface	10
2.2 Molecular Self-assembly at a Surface	12
2.2.1 Thermodynamics and Kinetics of 2-d Self-assembly	13
2.2.2 Molecule-molecule and Molecule-surface Interactions	16
1) Molecule-molecule Interactions	16
2) Molecule-substrate Interactions	20
2.3 Surface Confined Polymerization	23
2.3.1 Organometallic Bonding	24
2.3.2 Ullmann Coupling	25
1) Influence of the Functional Groups	27
2) Role of the Underlying Substrate	28
Chapter 3 Experimental Techniques and Methods	30
3.1 Experimental Techniques	31
3.1.1 Ultra-high vacuum (UHV) system	31
3.1.2 Vacuum Pumps	33
3.1.3 Low Energy Electron Diffraction (LEED)	37
3.1.4 Auger Electron Spectroscopy (AES)	42
1) Auger Process	42
2) Characteristic Auger Electron Energies	42
3) Instrumentation and Spectra	44
3.1.5 Scanning Tunneling Microscopy (STM)	45
1) Introduction	45
2) Tunneling Effect	48
3.2 Density Functional Theory (DFT)	51
3.3 Sample Preparation	52
3.3.1 Si (111) $\sqrt{3}\times\sqrt{3}$ R30°-Ag	52
3.3.2 Single Crystals	54
3.3.3 Molecular Deposition	55
Chapter 4 Supramolecular structures of TBTTA on the Si(111) $\sqrt{3}\times\sqrt{3}$R30°-Ag surface	56
4.1 Introduction	57

4.2	Experiment.....	58
4.3	Results and Discussion	60
4.4	Summary	64
Chapter 5	Adsorption of TIPT on Si(111) $\sqrt{3}\times\sqrt{3}R30^\circ$-Ag and Ag(111).....	66
5.1	Introduction	67
5.2	Experiment.....	68
5.3	Results and Discussion	70
5.3.1	Adsorption of TIPT on Ag(111)	70
1)	Molecular Adsorption with Substrate at RT	70
2)	Organometallic TIPT Structures on Ag(111)	72
3)	Annealing Experiments	74
5.3.2	Adsorption of TIPT on Si(111) $\sqrt{3}\times\sqrt{3}R30^\circ$ -Ag	79
1)	Molecular Adsorption with the substrate at RT	79
2)	DFT results and discussion	85
3)	Annealing Experiments	90
4)	Effect of Deposition on Si(111) $\sqrt{3}\times\sqrt{3}R30^\circ$ -Ag Substrate	91
5.4	Summary	92
Chapter 6	Adsorption of TBTANG on Si(111) $\sqrt{3}\times\sqrt{3}R30^\circ$-Ag and Au(111).....	95
6.1	Introduction	96
6.2	Experiment.....	97
6.3	Results and Discussion	99
6.3.1	Adsorption of TBTANG on Au(111)	99
1)	Molecular Adsorption with the Substrate at RT	99
2)	Molecular Adsorption on a Hot Surface	101
6.3.2	Adsorption of TBTANG onto the Si(111) $\sqrt{3}\times\sqrt{3}R30^\circ$ -Ag Surface	103
1)	Molecular adsorption with Substrate at RT	103
2)	Effect of Annealing	109
6.4	Summary	111
Chapter 7	Conclusions and Outlook.....	114
References	120

Chapter 1

Introduction

Understanding and manipulating matter on atomic level are considered key goals in materials science. To investigate how atoms and molecules arrange themselves into novel structures upon deposition, and understand the resulting emergent behavior and interesting phenomena has attracted countless researchers [1].

The year 1981 can be considered a milestone for surface science, since the rules of the game were fundamentally changed when the first Scanning Tunneling Microscope (STM) was invented [2]. Although a large number of techniques had been applied in surface science before that, low-energy electron microscopy, scanning electron microscopy, reflection electron microscopy to name a few, with the invention of STM, scientists got a chance to observe and manipulate matter at the atomic scale.

The introduction of the term, ‘nanotechnology’, is often attributed to the talk ‘There’s plenty of room at the bottom’, by physicist Richard P. Feynman at the annual meeting of the American Physical Society in 1959 at the California Institute of Technology [3]. In the talk, Feynman suggested how it should be possible to manipulate and produce things that were many, many times smaller than the smallest miniaturization achievable at the time. He predicted that humans would be able to control matter at an atomic level by the year 2000. He was right to some extent, since the invention of the STM made his prediction come true just 30 years after his talk. Since its invention, it has become one of the most powerful tools in surface science. Moreover, the method is not only limited to obtaining the topography of a surface at an atomic level, it can also be applied to manipulate atoms and molecules on these same surfaces.

In the last several decades, STM has also proven of paramount importance in studying the self-assembly of molecules at surfaces. Supramolecular self-assembly is a spontaneous and reversible process by which single molecular species arrange themselves into ordered two dimensional structures via non-covalent intermolecular interactions. The phenomenon has been widely considered as a bottom-up approach to the patterning of surfaces [4-8]. Moreover, the self-assembly of molecules can be carried out

in a wide range of environments such as; in solution, on solid surfaces [9, 10] or at the liquid-solid interface [11, 12].

In addition to a fundamental interest in understanding the behavior of the molecules on surfaces, two dimensional (2-d) supramolecular self-assembly is of considerable importance in many practical applications. For example, a phenanthroline-containing molecule self-assembles to form a supramolecular optical sensor that is sensitive to micromolar concentrations of various hazardous metals [13]. Self-assembly also impacts the manufacturing of molecular electronic devices. For example, self-assembled guanosine derivatives are important in the fabrication of electronic nano-devices [14].

Although self-assembled molecular networks are highly ordered due to the weak nature and the reversibility of the non-covalent bonds between molecules, the weak bonds can also limit application of these molecular aggregates in some real-world applications. In order to improve thermal, mechanical and chemical stability, the potential realization of regular molecular networks held together by stronger covalent bonds has triggered increased attention. In addition, covalent nanostructures can exhibit relatively high charge carrier mobilities due to their strong intermolecular bonds. Surface confined polymerization has been widely explored as a promising route to the creation of one- and two-dimensional (1-d/2-d) surface-supported polymers with a high degree of order and electronic conjugation.

One approach to on-surface polymerization is the adsorption of halogenated aromatic precursors onto atomically flat single-crystal surfaces. The surface acts to both catalyze the de-halogenation of an aryl-halide, and to confine the subsequent polymerization reaction in two dimensions. Several successful examples of 2-d polymers have been demonstrated on single crystal surfaces [15-19], however limited work has been done to exploit surface confined polymerization on semiconducting surfaces such as silicon.

An active polymer layer on a silicon surface could form the basis of an organic-inorganic semiconductor hybrid device which could be incorporated into existing Si electronics technology [20, 21]. One significant challenge to 2-d polymerization on silicon however, is the high reactivity of the surface to organic molecules [20]. One approach is to passivate the Si surface and ensure a surface with high mobility, to allow for the supramolecular ordering of the organic precursors. For example, the Si(111) $\sqrt{3}$ -Ag surface has been demonstrated to be a weakly interacting surface, allowing a number of organic molecules to remain mobile and form well-ordered 2-d layers [22-26].

Three halogenated molecules will be examined in this thesis. One molecule is a brominated tetrathienoanthracene (TBTTA) monomer (Figure 1.1 (a)); the other two are 3-fold symmetric organic molecules: 2,4,6-tris(4-iodophenyl)-1,3,5-triazine (TIPT) (Figure 1.1(b)) and 2,6,10-tribromo-4,8,12-trioxa-3a²-azadibenzo[cd,mn]pyrene (TBTANG) (Figure 1.1(c)).

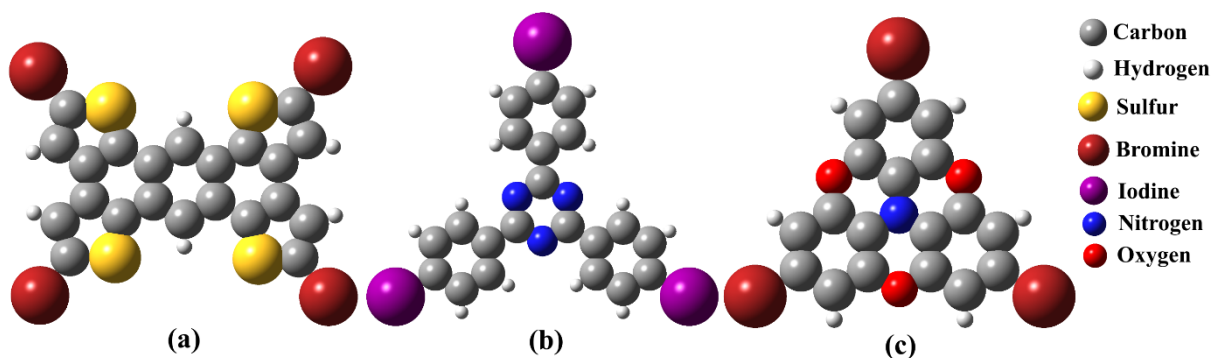


Figure 1.1. The molecular structure of (a) TBTTA, (b) TIPT and (c) TBTANG.

The initial goal of the thesis is to investigate the mobility of halogenated precursors on the Si(111) $\sqrt{3}$ -Ag surface. Our work demonstrates that the deposition of TBTTA onto the Si(111) $\sqrt{3}$ -Ag surface at room temperature leads to the supramolecular assembly of molecules. STM images reveal that at low coverage, the molecules readily migrate to step edges and defects in the $\sqrt{3}$ -Ag overlayer. With increasing coverage, the molecules eventually form compact supramolecular structures. These results indicate that $\sqrt{3}$ -Ag

adlayer acts to passivate the silicon surface and provides a high-mobility template for TBTTA adsorption [27].

We also study the adsorption of TIPT molecules onto two different, but related surfaces, Ag(111) and Si(111) $\sqrt{3}$ -Ag, to highlight the effect of molecule-substrate interactions. Ag(111) is a simple close-packed noble metal surface, while Si(111) $\sqrt{3}$ -Ag has a so-called honeycomb-chain-trimer structure, obtained after one monolayer of Ag is deposited onto the Si substrate. It consists of pseudo-hexagons of Ag surrounding Si trimers [28]. This more complex surface is less reactive than the bare Si surface but can still interact with molecules, affecting the ordering of the overlayer.

The second three-fold molecule we investigate, TBTANG, is also a halogenated molecular precursor. This molecule was deposited and diffuses freely on Si(111) $\sqrt{3}$ -Ag surface at room temperature. With increasing coverage, TBTANG exhibits a long-range self-assembled structure of intact molecules. The ordered structure is characterized by several closely packed rows of molecules. Within the rows the repeating motif is two-molecules linked together by non-covalent halogen-halogen interactions. As the coverage approaches one monolayer, the Si(111) $\sqrt{3}$ -Ag surface remains unaffected and the self-assembled layer extends over the entire surface. Defects in the Si(111) $\sqrt{3}$ -Ag substrate do affect the integrity of domains, but the size of domains does not appear to be limited by the density of these defects. We found the size and the symmetry of the unit cell on the complete layer is very close to the supramolecular layer found on the Au(111) surface [29]. However, due to differences between two substrates, the molecular structure does exhibit some interesting features which are unique to the Si(111) $\sqrt{3}$ -Ag surface.

The thesis is organized as follows:

Chapter 2 briefly reviews the up-to-date fundamental understanding of molecules at surfaces as well as the current state-of-the-art of research in 2-d supramolecular self-assembly and on-surface synthesis of 2-d polymers. The discussion will primarily focus on the influence of key parameters affecting molecular self-assembly and on-surface polymerization, such as the properties of the substrate, the types of inter-molecular interactions, and the effect of the substrate on the structure of the overlayer.

Chapter 3 gives a short outline of the significant experimental as well as theoretical techniques employed in the thesis, including ultra-high vacuum (UHV) technology, Low Energy Electron Diffraction (LEED), Auger Electron Spectroscopy (AES), Scanning Tunneling Microscopy (STM) and Density Functional Theory (DFT). A brief introduction to the molecular precursors utilized in this work is also included.

Chapter 4 discusses the supramolecular assembly of TBTTA on Si(111) $\sqrt{3}$ -Ag surface at room temperature, and Chapter 5 is devoted to TIPT deposition on the Ag(111) and Si(111) $\sqrt{3}$ -Ag surfaces both at room temperature and elevated temperatures. Chapter 6 presents the supramolecular self-assembly of TBTANG both on the Au(111) and Si(111) $\sqrt{3}$ -Ag surfaces at room temperature. The formation of a 2-d TBTANG polymer on the Au(111) surface is also discussed.

Chapter 7 provides a summary of all the experimental, and theoretical findings, and based on these results, future directions for this work are suggested.

Chapter 2

Background

2.1 Substrates

2.1.1 Ag(111) and Au(111)

Ag is a stable transition metal, and one of the few metals found abundantly in nature as a pure native element. This stability is due to its relative inertness. The crystal structure of silver is face centered cubic (fcc) (Figure 2.1a), and so the Ag(111) plane exhibits atomically flat surface with hexagonal arrangement of surface atoms (Figure 2.1b). This (111) surface has the lowest energy of the high symmetry surfaces.

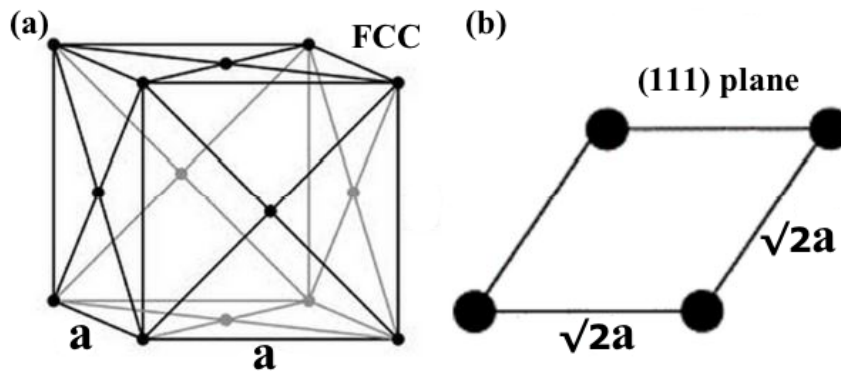


Figure 2.1. (a) FCC crystal structure of silver. (b) The (111) plane of silver

Au(111) also exhibits a hexagonal surface. However, in contrast to the other noble metals, the Au(111) surface reconstructs into a so-called herringbone structure at room temperature [30-32]. This reconstruction is due to the uniaxial compressive strain of the outermost layer such that 23 atoms are arranged over 22 bulk lattice sites underneath (see Figure 2.2). This mismatch between top layer and

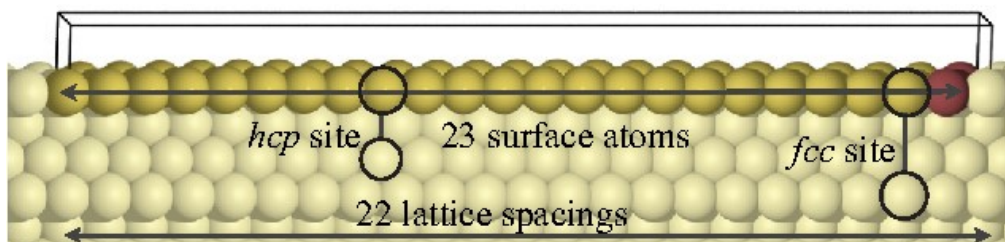


Figure 2.2. Schematic representation of a vertical cut through the first few layers of the Au(111) substrate, showing how 23 surface atoms fit into 22 lattice sites by compressing the top layer of the surface with the additional atom colored dark red. The positions corresponding to lined-up fcc and hcp sites are indicated by the vertical lines. Figure adapted from Hanke *et al.* (2013)

second layer leads to a rectangular unit cell of $(2a \times \sqrt{3}a)$ and periodically distributed areas of fcc and hcp-type stacking.

2.1.2 Silicon Crystallography

Silicon is one of the most commonly used semiconducting substrates. Silicon has a diamond lattice structure (fcc with a basis of two atoms). The primary cleavage plane, (111) as outlined in Figure 2.3, is one of the most complicated and fascinating planes and has been studied extensively in research fields ranging from fundamental surface science and materials science to nanotechnology.

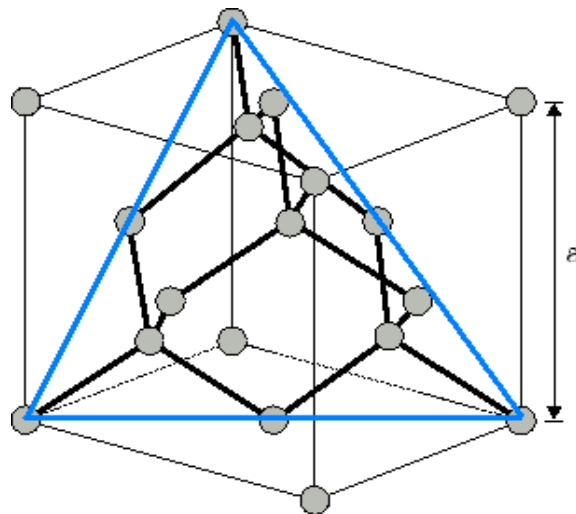


Figure 2. 3. The (111) plane of a silicon crystal (outlined in blue).

When a clean oxide-free (111)-oriented surface of Silicon is heated to sufficiently high temperatures (at least 400°C), and under UHV conditions, the surface atoms rearrange into their lowest energy 7×7 configuration which is stable at room temperature. In 1985, Takayanagi performed a comprehensive structural analysis of the Si(111) 7×7 surface reconstruction by evaluating the intensity distribution of the spots in transmission electron diffraction patterns and was able to propose a model that involved dimers, stacking faults and adatoms [33]. This model is known as the dimer-adatom-stacking-fault (DAS) model and remains the gold standard in our understanding of the geometry of the Si(111) 7×7 reconstruction.

As schematically shown in Figure 2.4, each supercell in the DAS model of the 7×7 reconstruction consists of three layers. The top layer contains 12 atoms (the so called adatoms); the second layer is the rest atom layer with 42 atoms, and 48 atoms are in the third layer that contains a stacking fault. Of all the surface atoms involved in the reconstruction, 19 are threefold coordinated and possess dangling bonds. In particular, there are 12 adatoms, 6 rest atoms and 1 atom in the center of the corner hole.

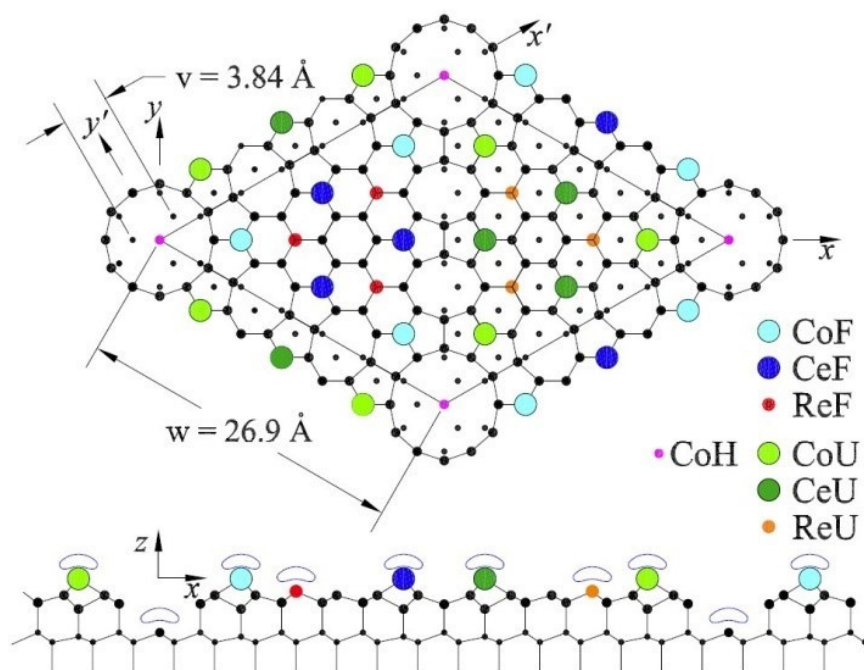


Figure 2.4. The top view and side view of the 7×7 cell. The adatoms in the DAS model fall into four symmetry classes: corner faulted (CoF), center faulted (CeF), corner unfaulted (CoU), center unfaulted (CeU). The 19 dangling bonds occur at 12 adatoms, 6 rest atoms (ReF, ReU) and the atom in the center of the corner hole (CoH). Graph reproduced from Giessibl *et al.* (2001).

2.1.3 Si (111) $\sqrt{3} \times \sqrt{3} R30^\circ$ - Ag Surface

In our research, a template with enough mobility to allow for the diffusion of organic molecules is crucial. Even though the 7×7 reconstruction reduces the dangling bond density from 49 to 19 per 7×7 unit cell, previous research has indicated that many organic molecules deposited onto this surface are not mobile enough to form ordered domains, and rather absorb randomly and “hit and stick” [34]. To overcome this problem, one solution is to passivate the Si surface. Several approaches have been explored,

i.e. Hydrogen terminated silicon surfaces [4-6], Boron terminated silicon surfaces [7-10], and an ordered monolayer of metal on silicon surfaces [11-15].

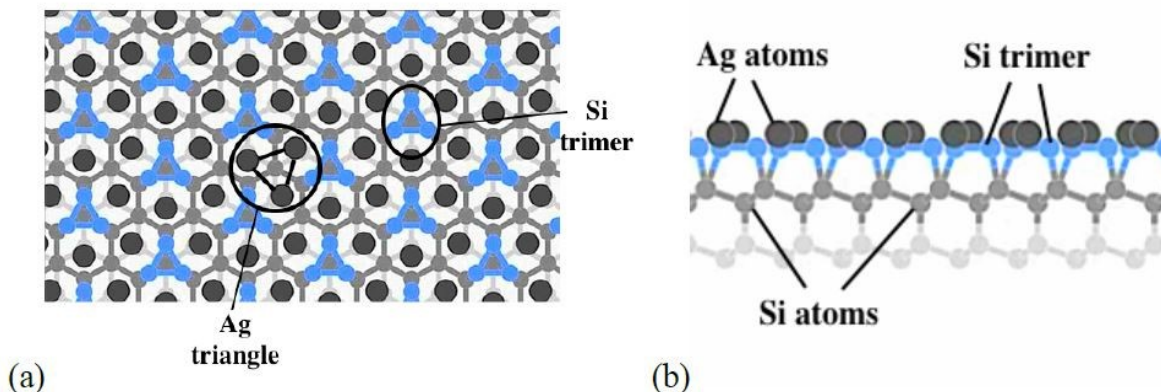


Figure 2. 5. (a) A top view of Ag - $\sqrt{3}\times\sqrt{3}$ structure on the Si(111) surface, and (b) a side view of the silicon trimers with Ag atoms on the top layer.

In our work we focus on the latter approach and in particular the Si(111) $\sqrt{3}\times\sqrt{3}$ R30°- Ag surface. It is generally accepted that the $\sqrt{3}\times\sqrt{3}$ reconstruction is obtained following the deposition of one monolayer of silver at a substrate temperature of 600°C. One monolayer (1ML) is defined here as 7.83×10^{14} Ag atoms/cm². Two popular structural models for the Si(111) $\sqrt{3}$ -Ag surface are the honeycomb-chained-triangle (HCT) model [35-37] and the inequivalent-triangle (IET) model [38]. The HCT structure is often

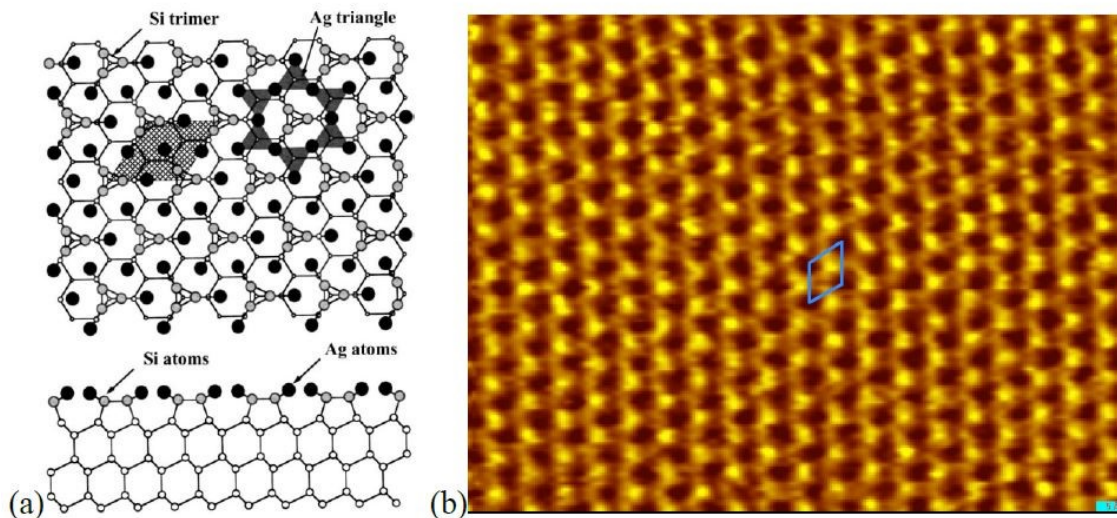


Figure 2. 6. (a) The atomic structure of the $\sqrt{3}$ -Ag reconstruction, with the hexagonal unit cell shaded. Figure reproduced from Tong *et al.* (2002). (b) A $100\text{\AA}\times 100\text{\AA}$ STM image of the $\sqrt{3}$ -Ag surface with unit cell highlighted in blue.

observed at room temperature (RT) and total energy calculations based on DFT indicate that the HCT model has lower surface energy [38]. According to the HCT model, deposition of a monolayer of silver atoms leads to the formation of the silicon trimers such that every Si atom at the surface is 4-fold coordinated and therefore there are no Si dangling bonds (Figure 2.5).

Figure 2.6 illustrates a schematic of the atomic arrangement of the $\sqrt{3}$ -Ag reconstruction (a) and an associated STM image of this reconstruction (b). The highly ordered 2-d hexagonal structure can be observed in the image.

2.2 Molecular Self-assembly at a Surface

In 1978, the term ‘supramolecular chemistry’ was first introduced by Jean-Marie Lehn in order to define, consolidate and generalize the areas of crown ether chemistry, host-guest chemistry, and the chemistry of molecular recognition. Only nine years later, the importance of supramolecular chemistry was recognized by the awarding of the 1987 Nobel Prize in Chemistry to Donald J. Cram, Jean-Marie Lehn, and Charles J. Pedersen in recognition of their work in this area.

Molecular self-assembly is a common concept in the field of supramolecular chemistry. “The spontaneous association of molecules under equilibrium conditions into stable, structurally well-defined aggregates joined by noncovalent bonds” can be considered the most general definition for molecular self-assembly as provided by Whitesides in 1991 [4]. During the self-assembly, molecules interact only with their closest neighbors and form specific organized aggregates or networks of different sizes [10].

The initial interest in self-assembly was understandable, given the fact that living cells self-assemble. In other words, the ultimate supramolecular assembly is ourselves, and understanding ourselves requires understanding self-assembly. Self-assembly has also been widely studied in non-living systems. For example, crystallization is an example of self-assembly in a 3-d system [16]. Other examples such as

surface supported self-assembled monolayers and the growth of nanowires [17] corresponds to 2-d and 1-d systems respectively.

The field of surface-supported self-assembly has received significant attention recently. Research involving a variety of organic and inorganic building blocks, on many different substrates have been reported [10, 39-42].

2.2.1 Thermodynamics and Kinetics of 2-d Self-assembly

Bottom-up and top-down are the two contrasting strategies for the fabrication of nanostructures at surfaces. Molecular self-assembly is a classic bottom-up approach to create surface patterns and devices on substrates in a controlled and repeatable manner. A great number of 2-d self-assembled structures have been explored on different substrates in vacuum, ambient, or in solution. The two major factors that influence the 2-d self-assembly are thermodynamic and kinetic effects.

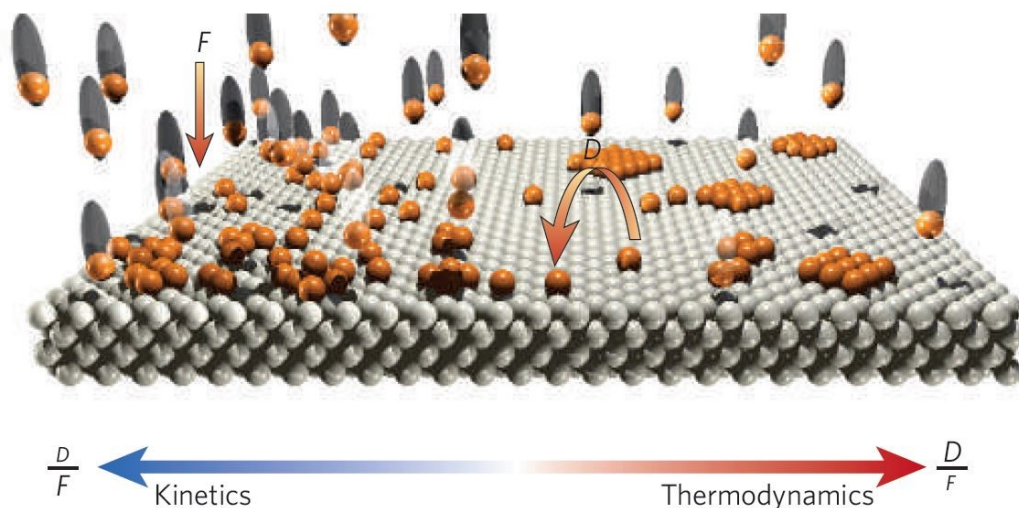


Figure 2.7. Schematic diagram showing growth processes for atoms or molecules deposited at surfaces. D = diffusivity, the mean square distance by which an adsorbate travels per unit time; F = deposition rate. The ratio D/F characterizes the growth regime: kinetically or thermodynamically controlled. Figure adapted from Barth *et al.* (2005).

Figure 2.7 illustrates how molecules or atoms deposited from the vapor phase grow into nanostructures on a surface at an atomic length scale [7]. In the figure, F is the deposition flux and D is the diffusion rate. The deposition flux, or the rate of deposition, is a relatively simple parameter. The diffusion rate on the other hand needs further explanation. Upon deposition, adsorbed species make a random walk on the surface. This motion will continue until the adsorbate is trapped at a fixed nucleation site, such as a surface defect or step edge, or until they bind to other adsorbates which allows for the formation of a stable nucleus. The diffusion rate is the mean square distance travelled by an adsorbate per unit time, and is a measure of how efficiently an adsorbate diffuses on the surface. When the deposition rate is smaller than the diffusion rate (large D/F value), adsorbates have enough time to explore the potential energy landscape of the surface such that the nucleation of new aggregates occurs at close to equilibrium conditions. This leads to so called “molecular self-assembly”. In contrast, when structures grow under conditions of high deposition rate and relatively low diffusion (small D/F values), the adsorbates are not mobile enough to reach a low energy configuration before meeting other adsorbates. Under these conditions the growth process is primarily determined by kinetics and the term ‘self-organized growth’ is used to describe this phenomenon. For example, in the study on the co-adsorption of coronene and cobalt octaethylporphyrin (CoOEP) at the phenyloctane solution/Au(111) interface, Jahanbekam *et al.* observed the competition between kinetics and thermodynamics for formation of the 1–1 (1 coronene to 1 CoOEP) surface structure [43]. By changing the relative concentration of two components in the solution, three different compositional phases (pure CoOEP, 1–1 phase and pure coronene) are observed. They found that once 1–1 surface structure is formed, it can only be converted to pure CoOEP phase by increasing CoOEP concentration but resistant to conversion to pure coronene by flooding with concentrated coronene. Thus, the conclusion on the formation of these 1–1 surface phases is controlled by kinetics was obtained. In order to control

on-surface molecular self-assembly, the respective roles played by kinetics and thermodynamics need to be carefully considered.

Like any other spontaneous process, self-assembly is the process in which the components of the system, molecules in our case, organize into ordered structures as a consequence of specific, local interactions among the components themselves, with no external direction. In other words, by noncovalent bond formation and bond breaking between molecules, the system evolves towards a minimum in the Gibbs free energy ΔG which can be expressed by equation:

$$\Delta G = \Delta H - T\Delta S$$

where ΔG is the change in Gibbs free energy, ΔH is the change in enthalpy, ΔS is the change in entropy, and T is the temperature of the molecular system. When the process takes place in vacuum, the most important interactions which contribute to an enthalpy change, ΔH , are adsorbate-adsorbate and adsorbate-substrate interaction energies. Thus, self-assembly usually emerges from an initially disorganized state and converges towards a more ordered configuration. Molecules form ordered assemblies via intermolecular interactions, which decreases the degrees of freedom, and causes a reduction of the total entropy of the system, i.e. $\Delta S < 0$. At the initial stages of the self-assembly, due to the relatively large negative values of $T\Delta S$, $\Delta G > 0$ in spite of ΔH being negative [44, 45]. The initial complexes formed are thermodynamically unstable. As the assembly increases in size, the dominance of the ΔH term over the $-T\Delta S$ term drives the Gibbs free energy of the system progressively more negative. This process continues until a minimization of free energy is obtained and the complex is thermodynamically stable.

However, during evolution towards the final equilibrium state, the system can become trapped in a state far from thermodynamic equilibrium [7, 46]. As described previously in Figure 2.7, the growth of adsorbed molecules into structures is primarily influenced by the deposition flux F and the diffusion rate

D on the surface. Non-equilibrium arrangements can form when the D/F ratio is small, and a local energetic minimum is reached faster than the thermodynamic global minimum. If the system does not have sufficient energy to overcome the energy barrier for a transition towards the global minimum, non-equilibrium arrangements will persist on the surface and result in kinetically trapped structures. One example reported by Anna *et al.* [47] demonstrates that the formation of the self-assembly of tetra-(phenylthymine)porphyrin (tetra-TP) and 9-propyladenine (PA) on highly oriented pyrolytic graphite (HOPG) is strongly related to the overall concentration and molar ratio of the molecular species. They revealed that due to the low solubility of tetra-TP in solution, it is difficult for the adsorbed tetra-TP to desorb back into solution. As a result, the adsorbed tetra-TP and PA are kinetically trapped on the HOPG surface.

2.2.2 Molecule-molecule and Molecule-surface Interactions

In surface-confined molecular self-assembly, both molecule-molecule and molecule-substrate interactions play a role in the stabilization of resultant molecular networks. By properly selecting the molecular building blocks with desired functional groups and substrates with the appropriate mobility, symmetry and electronic properties, molecular networks with different shapes, sizes and dimensionality can be constructed in a controllable manner [5].

1) Molecule-molecule Interactions

The formation of supramolecular assemblies on surfaces is a process where individual building blocks are in dynamic equilibrium with the growing structures, and the interactions holding the blocks together need to be reversible. The reversibility allows for self-correction and self-healing of the structures, and offers the possibility of obtaining nanostructures with a high degree of perfection. Herein, I present a brief discussion of the characteristics and properties of various intermolecular interactions along with several

examples to illustrate the role of these molecule-molecule interactions in molecular self-assembly at surfaces.

Van der Waals interactions

The Van der Waals (vdW) interaction is a non-covalent interaction between either; two induced dipoles, two permanent dipoles or a permanent and an induced dipole. Although vdWs interactions are weaker than hydrogen bonding (see below), they can still drive the formation of highly ordered 2-d self-assembled structures at solid surfaces [48-50]. One example is the pioneering study of the adsorption of 5,10,15,20-Tetrakis-(3,5-di-tertiarybutylphenyl) porphyrin (H₂-TBPP) on Au(111) using a low temperature STM as reported by Yokoyama *et al.* in 2001 [51, 52]. They describe how the formation of different supramolecular networks can be achieved by substituting porphyrins with either one or two cyano groups on the Au(111) surface.

Hydrogen bonding (H-bonding)

H-bonding is defined as an attractive, directional, non-covalent interaction between a hydrogen atom from a molecule or a molecular fragment and an atom or a group of atoms in the same or a different molecule [53]. Figure 2.8 is the standard representation of a hydrogen bond. The hydrogen bond donor

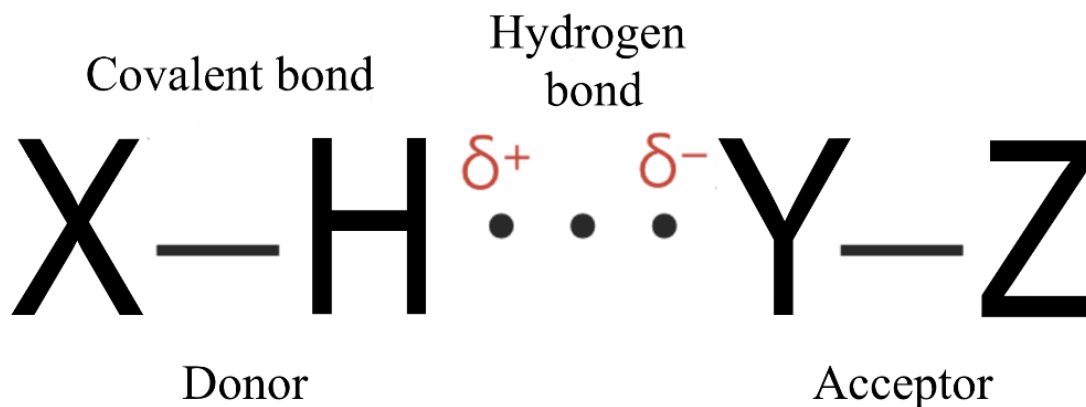


Figure 2.8. Hydrogen bond donor and acceptor atoms.

consists of a hydrogen atom (H) covalently bound to a more electronegative atom (X), thus forming a dipole in which the hydrogen atom is slightly positive. The acceptor may be an atom (Y), or a fragment or a molecule (Y-Z).

The bond strength of a hydrogen bond depends on the electronegativity of both X and A [54-56]. A typical hydrogen bond ($\sim 4.8 - 9.6 \text{ kcal}\cdot\text{mol}^{-1}$), is usually much stronger than a van der Waals interaction ($\sim 0.1 - 1 \text{ kcal}\cdot\text{mol}^{-1}$), such as in $\text{O-H}\cdots\text{O}=\text{C}$ ($7.4 \text{ kcal}\cdot\text{mol}^{-1}$) [57], $\text{N-H}\cdots\text{O}=\text{C}$ ($5.19 - 5.73 \text{ kcal}\cdot\text{mol}^{-1}$) [58] and $\text{O-H}\cdots\text{O-H}$ ($5.0 \text{ kcal}\cdot\text{mol}^{-1}$) [59, 60], where the X and A species are both strongly electronegative. H-bonding is one of the most common stabilizing interactions between functional groups in non-covalent assemblies on surfaces due to its strength and directionality [61-64]. A textbook example of a hydrogen bond stabilized 2-d self-assembly are the molecular networks formed by the co-deposition of perylene tetra-carboxylic di-imide (PTCDI) and 1,3,5-triazine-2,4,6-triamine, also known as melamine, on the $\sqrt{3}$ -Ag/Si(111) surface (Figure 2.9) reported by Beton *et al.* [25]. The network is stabilized by melamine - PTCDI hydrogen bonding represented by dotted lines in Figure 2.9(a).

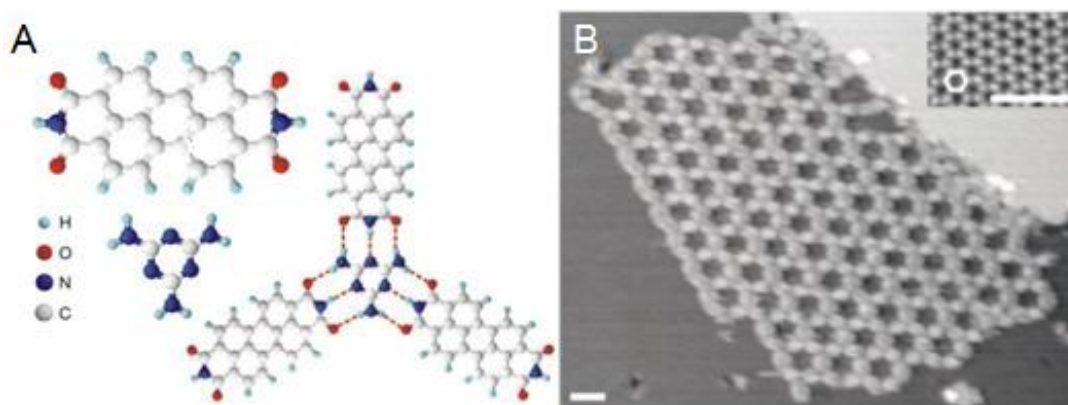


Figure 2. 9. (a) Chemical structures and H-bonding motif of PTCDI and melamine. (b) UHV-STM image of a network formed by both monomers at a silver-terminated silicon surface. Figure reproduced from Beton *et al.* 2003.

Halogen bonding (X-bonding)

The term “halogen bonding” or “halogen bond” refers to a highly directional, electrostatically-driven noncovalent interaction involving covalently-bonded halogen atoms in one molecule, to negative centers on adjacent molecules. Figure 2.10 is a schematic representation of halogen bonding which is abbreviated as $R-X\cdots Y$, where R can be carbon, halogen, nitrogen, etc., X is a halogen atom, and Y a negative site like N, O, Cl, Br, or I [40, 65]. In the context of tailored self-assembly on surfaces, one great advantage of halogen bonds compared with hydrogen bonds is that the bond strength can be tuned by choosing a different halogen termination. Moreover, halogen bonding has a higher directionality than hydrogen bonding [66, 67]. As a result, due to the selectivity, directionality, and tuneability, halogen bonding is currently receiving considerable attention as a suitable alternative to hydrogen bonding for the construction of supramolecular networks on surfaces [10, 40, 68]. For example, Walch *et al.* reported the formation of various self-assembled structures of 1,3,5-tris(4-bromophenyl)benzene on Ag(111) under UHV conditions [69]. In addition, the formation of highly-ordered self-assembled monolayers of an achiral organic semiconducting molecule at the solid-liquid interface has been demonstrated by Gutzler *et al.* [70]. In this thesis we have demonstrate the self-assembly of halogenated molecules (TBTTA, TIPT and TBTANG) on a passivated silicon surface [27] which will be discussed in Chapters 4, 5, and 6.

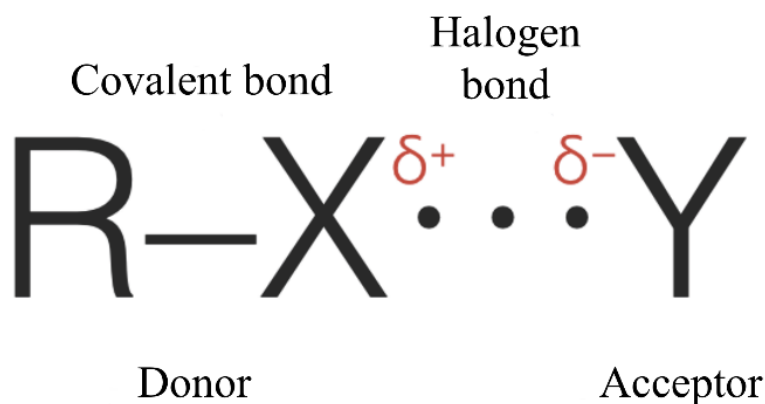


Figure 2. 10. Halogen bond donor and acceptor atoms

2) Molecule-substrate Interactions

Types of interactions

When a molecule is adsorbed onto a surface, it can bind to the surface via either a physical or a chemical interaction [71]. Physical adsorption, or physisorption, refers to a case when there is no electron

Table 2.1: A comparison between chemisorption and physisorption. (Taken from Ref. 73)

Chemisorption	Physisorption
electron exchange	polarization
chemical bond formation	van der Waals attractions
strong	weak
≥ 1 eV (100 kJ mol^{-1})	≤ 0.3 eV (30 kJ mol^{-1}), stable only at cryogenic temperatures
highly corrugated potential	less strongly directional
analogies with co-ordination chemistry	

transfer between the molecule and the substrate. In this case, the adsorbate interacts weakly with the substrate and the molecule-substrate interaction is usually of a van der Waals type [72]. Chemisorption, on the other hand, refers to the case when electron transfer or sharing, i.e. covalent bonding, occurs between the adsorbed species and the surface atoms. The main features of physisorption and chemisorption are summarized in Table 2.1.

Influence of the substrate on molecular self-assembly

In order to control 2-d molecular self-assembly on surfaces, it is crucial to exploit non-covalent intermolecular interactions. The choice of the substrate also plays an important role in the resultant overlayer structure [73]. There are two major influences the substrate can have on the self-assembly of organic molecules. First of all, the reactivity of the substrate will influence the diffusion of molecules on the surface. When the adsorbate-substrate interaction is too strong, adsorbates tend to “hit and stick” and this leads to a disordered overlayer. In general, a highly reactive surface will suppress the mobility of the molecules [74]. To reduce the reactivity of the substrate and enable the high mobility of organic molecules, atomically flat and chemically inert substrates are required. For example, Suzuki *et al.* compared the adsorption behavior of a prototypical functional molecule, Terephthalic acid (TPA), on the Si(111)- 7×7 ,

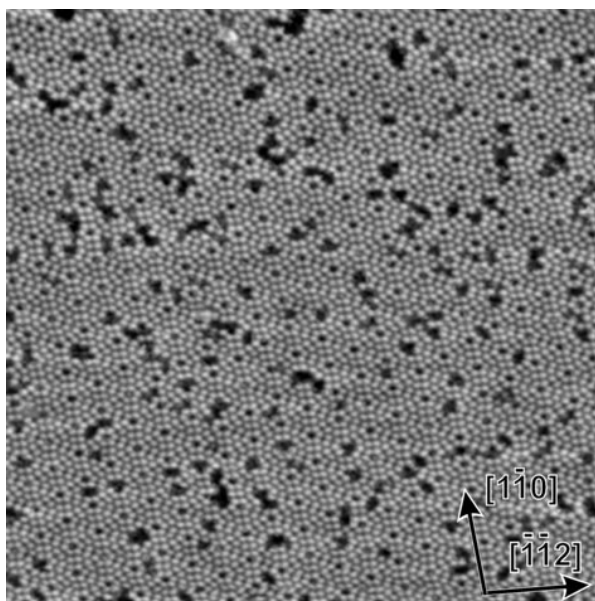


Figure 2.11. STM image after TPA deposition on the Si(111)- 7×7 surface. Dark spots are randomly adsorbed TPA molecules. Figure adapted from Suzuki *et al.* (2009).

Si(111) $\sqrt{3}$ -Ag, and Ag(111) surfaces [26]. Their results indicate that irreversible covalent bonds between the molecule and the surface are formed on the Si(111)- 7×7 due to the high density of dangling bonds. TPA adsorbs randomly on the Si substrate and does not form any ordered supramolecular structures. The observation of dark spots in Figure 2.11 attributed to adsorbed TPA monomers is an obvious clue. On the other hand, TPA forms an ordered layer on the Si(111) $\sqrt{3}$ -Ag surface (Figure 2.12a), and a brick wall-like structure on Ag(111) (Figure 2.12b).

The second effect of the substrate is to epitaxially constrain the molecular overlayer [9], by imposing an adsorption site on the molecules, and the size and symmetry of the resultant unit cell. An example is the adsorption of a particular porphyrin derivative on different metal surfaces as reported by Jung *et al.* in 1997 [75]. Results indicate that the porphyrin conformation differs on the three different surfaces: Cu(100), Au(110) and Ag(110) as shown in Figure 2.13. Different conformation configurations are due to the degree of rotation of the phenyl-porphyrin bonds. This rotation balances the intramolecular steric hindrance with the molecule-surface interactions. More recently, Liu *et al.* reported the 2-d self-assembly

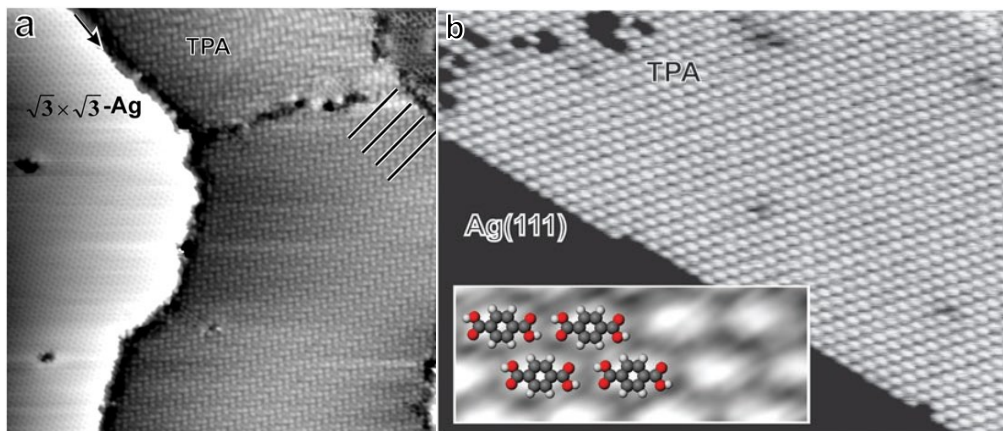


Figure 2.12. (a) STM image after the deposition of TPA on the Si(111) $\sqrt{3} \times \sqrt{3}$ -Ag surface. An atomic height step separating a bare Ag- $\sqrt{3}$ surface area and TPA region is indicated by an arrow. (b) STM image after the deposition of TPA on Ag(111). Figure adapted from Suzuki *et al.* (2009).

of 2,4,6-tris(4-bromophenyl)-1,3,5-triazine (BPT) on HOPG, and on single-layer graphene (SLG) grown on a polycrystalline Cu foil [76]. The molecules form two different self-assembled structures on the two surfaces: compact and a loose pattern on HOPG, and a porous structure with hexagonal-like cavities on the SLG surfaces. Moreover, in some cases the adsorption of molecules at preferential nucleation sites is observed. This effect is particularly interesting when the substrate can be used as a template to steer the growth of adsorbates. A good example is how the $22 \times \sqrt{3}$ herringbone reconstruction on Au(111) can lead to the ordered growth of 2-d C_{60} islands localized at the elbow sites of the reconstruction at low temperatures (~ 80 K) [77]. Following this report, a number of subsequent studies with different molecules have shown this to be a quite general phenomenon [52, 78].

Chemical reactions between substrate and adsorbates can also affect the organization of the overlayer. For example, the adsorption of organic molecules with halogen terminated functional groups on transition metal surfaces usually results in the formation of molecular coordination networks [17, 19, 69, 79] or polymerization [19, 79]. In the case of strong molecule-substrate interactions, the electronic structure of the substrate can be modified by the interaction. For example, the modification of surface state is observed

by Scheybal *et al.* in their study on the adsorption of pentacene on Cu(110) surface [80]. The interaction between molecules and substrates can also promote structural changes of the substrate surface. For example, the growth of the organic semiconductor 3,4,9,10 perylenetetracarboxylic dianhydride (PTCDA) on Cu(110) results in a restructuring of the underlying Cu(110) surface involving the addition or removal of Cu rows [81]. Another example involves the deposition of electronegative elements, such as oxygen, or halogen onto the Au(111) substrate. On adsorption, gold atoms from surface can be released from the outermost layer and locally lift the herringbone reconstruction [82, 83].

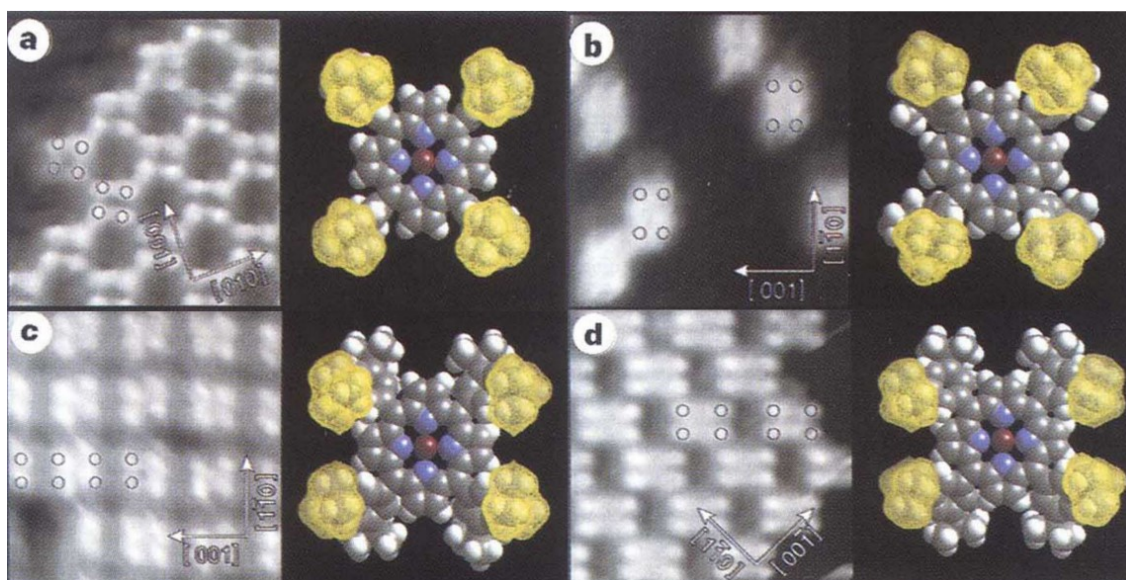


Figure 2.13. Conformational identification of Cu-TBPP in four stages on three surfaces. (a) on Cu(100). (b) on Au(110), precursors are still mobile. (c) on Au(110), final state. (d) on Ag(110). Figure reproduced from Jung *et al.* (1997).

2.3 Surface Confined Polymerization

Traditional polymerization of organic molecules involves monomers with two reactive sites per molecule which combine to form 1-d chains. Even when multiple reactive sites are involved, the resultant polymers often exhibit a disordered 3-d structure. In surface-confined polymerization multidentate monomers are deposited onto an atomically flat surface to confine the polymerization reaction epitaxially, and to produce polymers with a high degree of order and electronic conjugation in 2-d [84]. Compared

with self-assembled structures, covalently linked 2-d structures exhibit much higher chemical and mechanical stability. With tunable electronic properties, 2-d polymers are promising candidates for applications in electronic devices [85, 86]. Different approaches to synthesize 2-d polymers on surfaces have been proposed, such as Ullmann coupling, imine coupling, Glaser-Hay coupling, dehydration, dehydrogenation and Click reactions [87-91]. Of these approaches, Ullmann coupling has proven to be one of the most promising routes to the formation of 2-d covalent structures for aryl halides on single crystal noble-metal surfaces and is receiving considerable attention. In this thesis Ullmann coupling is exploited, and we are able to form highly ordered molecular overlayers linked via covalent bonds on Au(111) and on Ag(111) surfaces.

2.3.1 Organometallic Bonding

An organometallic bond can be defined as one in which there is a bonding interaction between one or more carbon atoms of an organic group or molecule and an inorganic metal species. Organometallic bonds are commonly identified as a reaction intermediate in on-surface Ullmann coupling under UHV conditions. Although an organometallic bond ($\sim 10 - 48 \text{ kcal}\cdot\text{mol}^{-1}$) is generally stronger than a H-bond ($\sim 4.8 - 9.6 \text{ kcal}\cdot\text{mol}^{-1}$), it is still weaker than a classic C–C bond with a bond energy of $\sim 85 \text{ kcal}\cdot\text{mol}^{-1}$. Thus, it exhibits sufficient reversibility during on-surface molecular self-assembly, allowing error correction by multiple bond breaking and bond reforming processes. This can be particularly beneficial for the construction of long-range ordered networks with relatively high stability [92], and makes the organometallic bond an important tool for the formation of 1-d/2-d molecular networks on metal surfaces [18, 69, 79, 93, 94].

Beyond simply linking organic molecules together, organometallic bonds have been identified as an intermediate state towards 2-d Ullmann coupling of molecules on noble metal surfaces in UHV [69, 93]. Following the carbon-halogen cleavage of halogen-terminated organic building blocks, the surface

stabilized radicals couple to adatoms of the metal substrates, resulting in metal-carbon bonds. The formation of organometallic bonds is highly dependent on the choice of metal substrate and the halogen termination of the molecules involved [95, 96]. For example, at room temperature, Iodine is spontaneously cleaved from organic molecules when deposited onto Cu, Ag and Au surfaces [97, 98]. On the other hand, Bromine is fully cleaved on Cu [17, 69] at room temperature, and only partially on Ag [19, 79]. Additional thermal activation is required to cleave C–Br bonds on Au. Ordered and disordered organometallic intermediates are commonly found on Ag [79, 99] and Cu [17, 19, 69], but only occasionally observed on gold [100].

2.3.2 Ullmann Coupling

The Ullmann reaction, or Ullmann coupling is one of the oldest heterogeneous reactions and is named after Fritz Ullmann, a German scientist who discovered it in 1901 [101]. It is a radical addition coupling reaction that takes place between aryl-halides in the presence of a copper catalyst (Figure 2.14). More recently, this well-known method has been adapted to surfaces to buildup a number of nanostructures in 1-d or 2-d on noble metal surfaces. Ullmann coupling is attracting more and more attention as bottom-up approach for the synthesis of 1-d and 2-d nanostructures, due to its high versatility, and the possibility of pre-defining the topology of the resulting covalent structure by the appropriate design of the precursor.

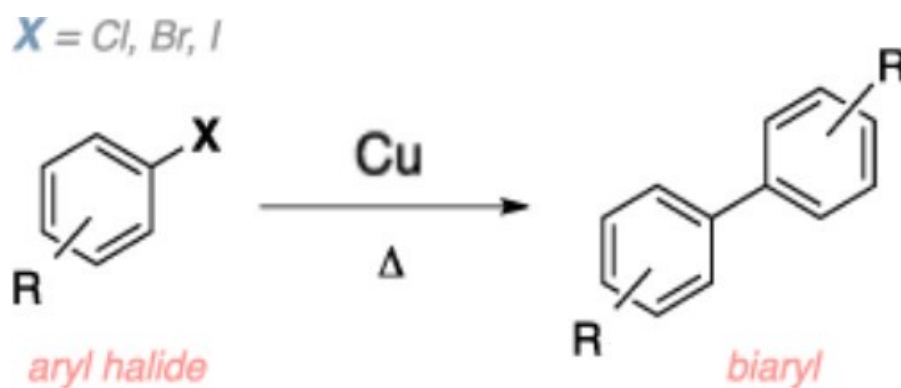


Figure 2. 14. Coupling reaction involving two aryl halides with a copper catalyst. Figure reproduced ed from Ullmann *et al.* (1901)

One excellent example was reported by Grill *et al.* in 2007, where they demonstrated the successful construction of 1-d or 2-d molecular networks by using different tetraporphyrin (TPP)-based molecules with one, two or four Br substituents [15]. Following deposition and annealing, molecules with one reactive site exclusively formed dimers, while those with two Br atoms per monomer formed linear chain structures. Finally, molecules with four reactive sites enabled the formation of 2-d networks (Figure 2.15). These results clearly demonstrate that the resultant architecture of the nanostructures can be controlled by both the number and position of reactive sites in the molecular building blocks. Generally, Ullmann based surface-confined polymerization involves two fundamental reaction steps (Figure 2.16). First, the dehalogenation of the molecular precursors, which involves cleavage of an aromatic carbon-halide bond. On many surfaces this results in an organometallic intermediate. In the second reaction step, often at elevated temperatures, covalent C–C coupling takes place. Thus, in order to control the synthesis of

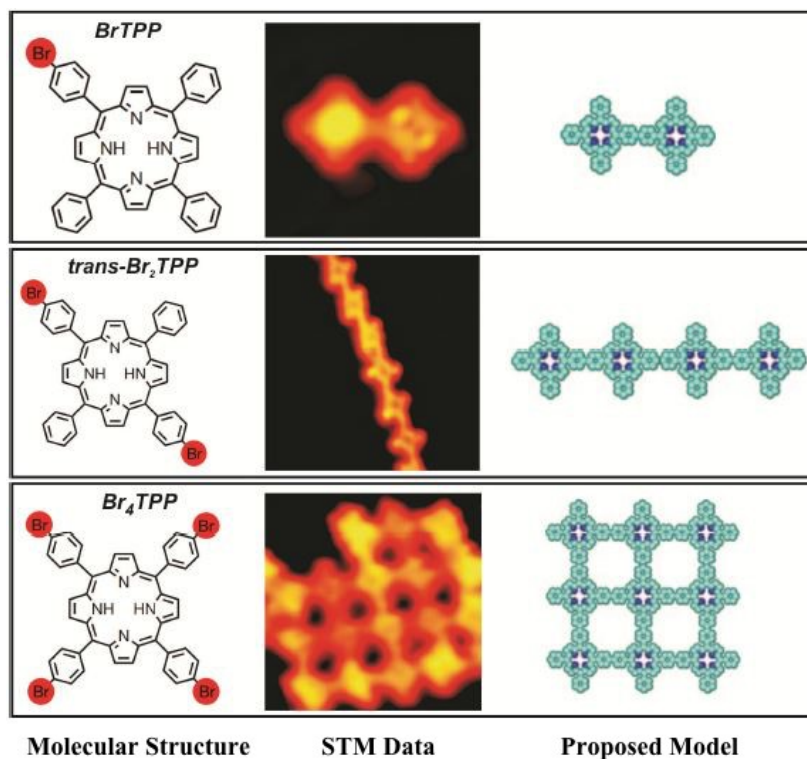


Figure 2.15. STM images and corresponding chemical structures of TPP monomers with 1,2 & 4 reactive sites on Au(111) surface. Figure adapted from Grill *et al.* (2007).

polymers with desired geometries and properties, these two steps need to be carefully considered in the Ullmann reaction.

1) Influence of the Functional Groups

In the initial step of surface-confined Ullmann coupling, halogen atoms dissociate from the precursor molecule. The bond energy of the carbon-halogen (C–X) bonds is lower compared with the carbon-carbon (C–C) bonds of the molecular backbone. The difference between these two bonds allows for the selective dissociation of the relatively weak C–X bonds without breaking the molecular backbone. The dissociation energy depends on the type of halogen atoms. To this end, molecular building blocks are often functionalized with bromine, iodine, or a combination of the two. The different chemical nature of these two halogen atoms is reflected in different halogen-carbon bond strengths where iodine (C–I bond strength is $\sim 57 \text{ kcal}\cdot\text{mol}^{-1}$) requires a lower activation temperature compared with bromine (C–Br bond strength is $\sim 66 \text{ kcal}\cdot\text{mol}^{-1}$) to dehalogenate from a molecular precursor on the same substrate [102]. The dissociated halogen can affect polymerization by “getting in the way”, or sterically hindering the long-range order of the final structures. Annealing samples to higher temperatures following dehalogenation can result in the desorption of the halogen atoms, however this thermal energy can also potentially destroy the newly formed networks [103].

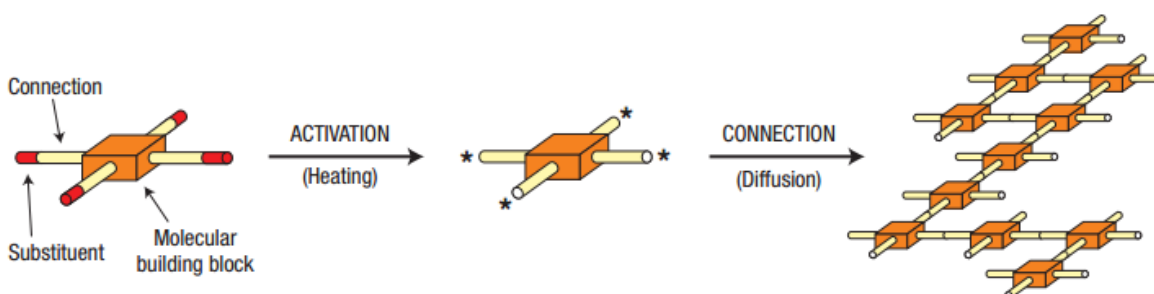


Figure 2.16. A schematic of the formation of covalently bonded networks by connecting the activated monomer building blocks. Figure adapted from Grill *et al.* (2007)

2) Role of the Underlying Substrate

In addition to the choice of halogen, the substrate also plays an important role in the Ullmann coupling reaction. Depending on the substrate material, different annealing temperatures are required to initiate dehalogenation. Björk *et al.* computationally studied the adsorption of both bromobenzene (C_6H_5Br) and iodobenzene (C_6H_5I) on the three commonly used close-packed (111) surfaces (Cu, Ag, and Au) [103]. Their results indicate that the Cu surface has the lowest barrier for dehalogenation, while Au has the largest. In addition, the catalytic activity of the substrate can depend on crystallographic orientation. Walch *et al.* [69] determined that the Br atoms of 1,3,5-tris(4-bromophenyl)benzene (TBB) split off spontaneously upon adsorption at RT on Ag(110), whereas only self-assembled structures of intact molecules are observed on Ag(111).

Following dehalogenation, the diffusion of the molecules on the substrate also plays a vital role in the structural integrity of the resultant polymers. Bieri *et al.* [97]. studied the deposition of a hexaiodo-substituted macrocycle, cyclohexa-*m*-phenylene (CHP) on three different surfaces; Cu(111), Au(111) and Ag(111). Dehalogenation in all cases occurs following deposition at RT. Subsequently the surfaces are brought to elevated temperatures to activate the polymerization step. Interestingly, the morphology of resultant molecular networks on the three surfaces is significantly different (Figure 2.17). On Cu(111), only branched low-density clusters with single-molecule-wide branches are obtained, while 2-d networks are formed on both Au(111) and Ag(111) surfaces, with a higher density and larger domain sizes observed on Ag(111). This phenomenon is due to the difference in the rates of diffusion and coupling of the CHP radicals on Ag and Cu and Au, which determines the structural order of the final product. On Cu(111), for example, the energy barrier for the diffusion of CHP radicals is significantly higher than the energy barrier for the formation of a covalent bond which leads to dendritic structures. In contrast, diffusion prevails over covalent coupling on Ag(111) and thus results in the formation of honeycomb networks.

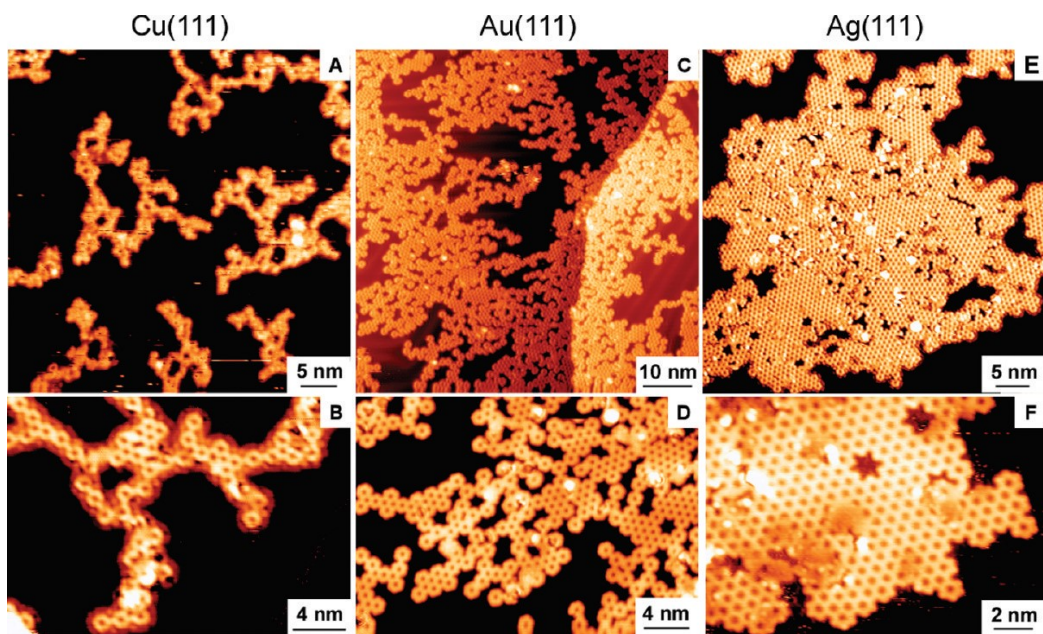


Figure 2.17. Top panels: Overview and high-resolution STM images of polyphenylene networks on Cu(111) (A,B), Au(111) (C,D), and Ag(111) (E,F). Figure adapted from Bieri *et al.* (2011).

Chapter 3

Experimental Techniques and Methods

3.1 Experimental Techniques

3.1.1 Ultra-high vacuum (UHV) system

UHV conditions are necessary for our experiments for two specific reasons: first, the silicon substrate surface is highly reactive; and second, to permit the use of low energy electron techniques without undue interference from gas phase scattering. The UHV system can reduce the contamination from background gases by reducing the number of molecules impinging on the surface. Monolayer formation time is defined as the time needed to form a single layer of molecules on a surface assuming that every molecule that strikes the surface sticks and that the molecules distribute evenly to form a single atomic layer. Considering a cube of length a . The total area of the cube faces is $6a^2$ and the volume is a^3 . With a gas density (n) and an average velocity $\langle v \rangle$, the collisions with the walls per second can be written as:

$$(na^3) \left(\frac{\langle v \rangle}{a} \right) = na^2 \langle v \rangle \quad (3-1)$$

So, the rate of arrival of atoms or molecules per unit area per second on one of the cube faces can be written as:

$$Z(\text{molecules}/\text{cm}^2/\text{s}) = \frac{1}{6} n \langle v \rangle \quad (3-2)$$

Using the kinetic theory of the gas, we know $n = \frac{P}{k_B T}$ and $\langle v \rangle = \sqrt{\frac{8RT}{\pi M}}$, thus equation (3-2) can be rewritten as:

$$Z = 3.5 \times 10^{22} \frac{P}{\sqrt{MT}} \quad (3-3)$$

Where P is the pressure in Torr, M is molecular weight in g/mole, and T is the temperature in Kelvin. At ambient temperature for air ($M=29$):

$$Z = 3.77 \times 10^{20} P \quad (3-4)$$

Assuming each nitrogen molecule occupies an area on the surface of d_0^2 (where $d_0 = 0.372 \text{ nm}$ for nitrogen) then the atomic flux can be written as:

$$Z \cdot d_0^2 = 4.84 \times 10^5 P \quad (3-5)$$

The monolayer formation time is just the inverse of the atomic flux, thus:

$$T_{ml} = \frac{1}{Z \cdot d_0^2} = 2.1 \times 10^{-6} / P \quad (3-6)$$

Therefore, at ambient temperature the monolayer formation time for air is $20,646 \text{ s}$ (5.7 hrs) in our UHV system ($P \sim 10^{-10} \text{ Torr}$). This is an acceptable value for our experiments and compares with only 2 s in a high vacuum system (10^{-6} Torr), or 2.5 ns at atmospheric pressure (760 Torr).

A couple of additional factors need to be mentioned. First, even in UHV the molecular density is still high. In other words, there are still a lot of gas molecules present. Second, the mean free path of these gas molecules is much greater than the dimensions of the vacuum chamber, which means that the gas molecules will collide with the chamber walls and other components in the vacuum many times before they meet each other.

Our UHV system contains four pumps (discussed below), a Residual Gas Analyzer (RGA), two evaporators (a metal and a molecular evaporator), a Low Energy Electron Diffraction (LEED) instrument,

an Auger Electron Spectrometer (AES) and a Scanning Tunneling Microscope (STM). A schematic of the vacuum system used in our experiments is shown in Figure 3.1.

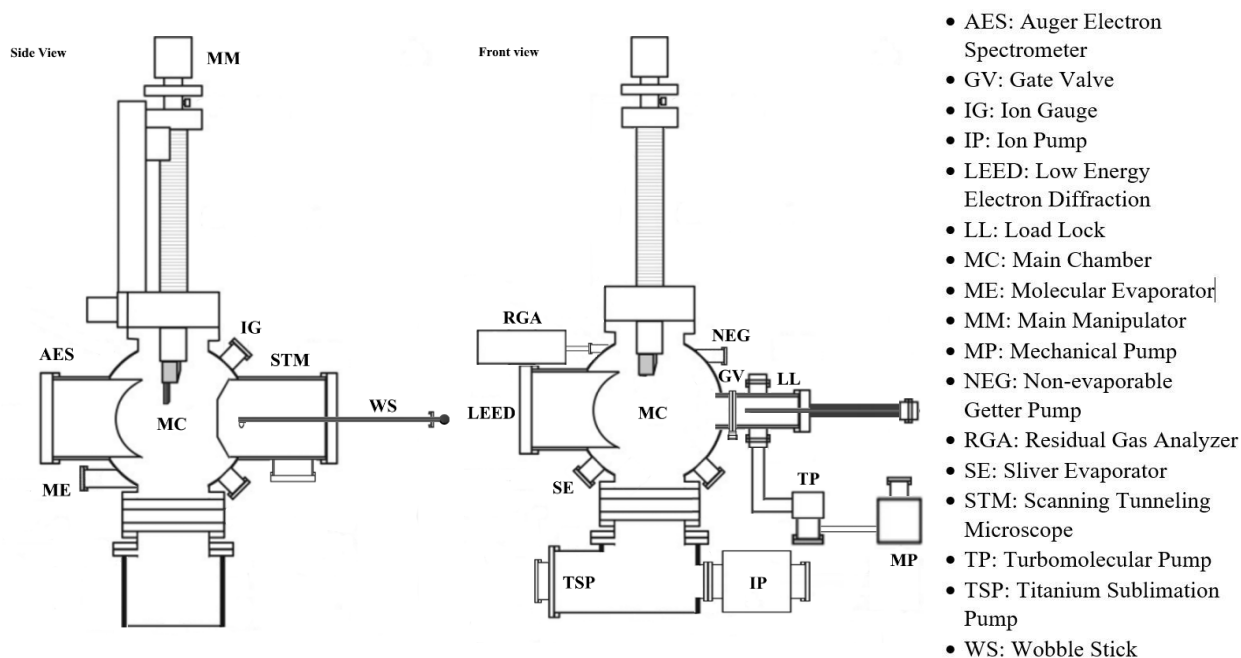


Figure 3.1. A schematic of our UHV system.

3.1.2 Vacuum Pumps

The reduction in pressure from atmosphere (760 Torr) to UHV (below 10^{-10} Torr) means changing the pressure value by ~13-14 orders of magnitude. This requires the work of multiple pumps. In our UHV system, four pumps are used in combination to maintain the base pressure inside the chamber.

A **Rotary Vane Pump** is used for pumping the system from atmospheric pressure down to about 10^{-3} Torr. In our system, it is also employed as a backing pump for a turbomolecular pump. Figure 3.2 shows the principle of the its operation using a schematic diagram*. Rotor and vanes divide the working chamber into two separate spaces having variable volumes. As the rotor turns, gas flows into the enlarging

* Edwards Vacuum (www.edwardsvacuum.com)

suction chamber until it is sealed off by the second vane. The enclosed gas is compressed until the discharge valve opens against atmospheric pressure.

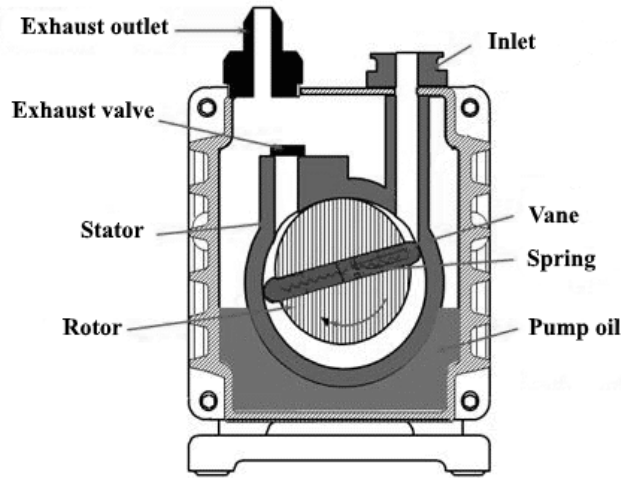


Figure 3.2. A cross-sectional view of the rotary vane pump. The rotor is rotated clockwise.

The turbomolecular pumps can be considered as the first level pump in our system. With a mechanical pump for backing, the pump is used for initial chamber pump down and to pump the fast entry load lock. The turbomolecular pump works on the principle of momentum transfer. High-speed rotating blades transfer momentum to the gas molecules, and the relative velocity between slotted rotor blades and slotted stator blades transports the gas molecules from inlet flange to the outlet (Figure 3.3).

Usually turbo pumps are designed with multiple blades and multiple stages. There are two parameters that characterize the performance of the turbomolecular pump. The first is the maximum compression ratio, which is defined as the ratio of the outlet to inlet pressure with no gas flow. The second parameter is the maximum pumping speed, which is defined as the flow rate of gas at the inlet when the compression ratio across the blades is unity. The ultimate pressure for a turbomolecular pump is determined by the compression ratio for the light gases (usually hydrogen) and the outgassing rate of the metal parts.

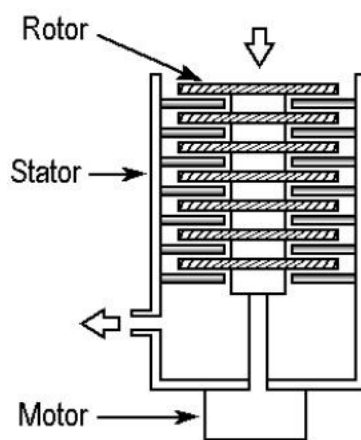


Figure 3.3. A schematic diagram of the design of a turbomolecular pump. Reproduced from Surface Science-An Introduction (K. Oura *et al.* 2003).

Turbomolecular pumps work most efficiently in the molecular flow regime (below 10^{-4} Torr), where the mean free path of the molecules is limited only by the dimensions of the vacuum enclosure. This is the reason a mechanical pump is required for backing. The turbomolecular pump we use in our laboratory is a Varian Turbo-V60*, which has a compression ratio of 5×10^7 and a pumping speed of 65 L per second for nitrogen. The ultimate pressure for this pump is 8×10^{-10} Torr.

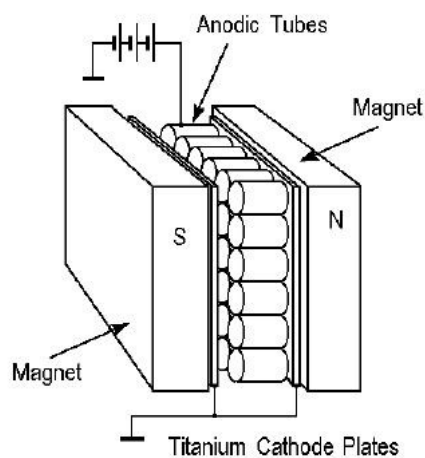


Figure 3.4. A schematic diagram of the design of an ion pump. Reproduced from Surface Science-An Introduction (K. Oura *et al.* 2003).

* Varian, Inc. <http://www.varianinc.com>

The **Ion pump** is the primary pump to maintain UHV conditions in our chamber. It starts to operate at about 10^{-3} Torr and can attain pressures of 10^{-11} Torr. An ion pump operates on the principle of Penning cold-cathode discharge [104]. The basic configuration of an ion pump (Figure 3.4) includes two plates of Ti (cathode) mounted close to the open ends of a collection of short stainless-steel tubes (anode), and two strong magnets.

During operation, high-energy electrons emitted from the cathode elements collide with and ionize gas molecules which are in turn accelerated towards the cathode. Due to the presence of both electric and magnetic fields in each cell, the electrons travel in helical orbits, which increases the path length before they reach the anode. The increased path length improves the chances of electron collision with gas molecules inside the Penning cell. Ionized gas molecules are accelerated to the titanium cathode and many are buried. The ions may also sputter titanium which can produce secondary electrons. The sputtered Ti is in turn deposited on nearby surfaces to getter active gases. Titanium is a very reactive metal, so the sputtered Ti chemically combines with any active gas molecules present (e.g. CO, CO₂, H₂, N₂, O₂) to form stable compounds, and thus removing them from the vacuum vessel. The ion pump in our system is a Varian, VacIon Plus 150* with an ultimate pressure of 10^{-11} Torr, and a pumping speed of 150 L per second for nitrogen.

In addition to the ion pump we use two getter pumps to achieve our base pressure; a titanium sublimation pump (TSP), and a non-evaporable getter pump (NEG).

The **Titanium sublimation pump** sublimates a fresh layer of titanium onto a relatively large surface. As in the ion pump, the titanium layer has a high pumping speed for reactive gases, which either form a chemical compound or are adsorbed. The Ti layer has a finite lifetime and therefore regular deposition is

* Varian, Inc. <http://www.varianinc.com>

required to maintain the pumping efficiency. Normally, at UHV pressures a fresh titanium film can be effective for several days.

The **non-evaporable getter pump** we use is a Capacitorr-D400 NEG pump*. Like the TSP the NEG pumps by chemisorbing active gases. For the NEG this is followed by bulk diffusion. The NEG is made from a sintered porous material (St 172 (Zr-V-Fe) alloy). and when the getter material is saturated it can be reactivated by heating the material to temperatures in the range of 150 °C – 300 °C.

In addition to the pumps mentioned, an extra step is required to attain UHV pressures. The system must undergo a baking step. When the vacuum system is exposed to ambient pressure, gas molecules are absorbed onto the walls of the vacuum chamber. When the pressure is reduced, these molecules desorb. The predominant gas desorbing from an unbaked system is water vapor. The ultimate pressure of the system represents equilibrium between the pumping speed of the system and the outgassing rate of the inner walls and components inside the chamber. Baking actually works to accelerate this outgassing process by heating the entire system. The so-called bakeout procedure is to heat the entire UHV system to a high temperature, typically higher than 100° Celsius, for several days so as to eliminate water vapor on cool down. An ultimate pressure after baking of less than 1×10^{-10} Torr is achieved in our system.

3.1.3 Low Energy Electron Diffraction (LEED)

Low energy electron diffraction (LEED) is one of the most widely used tools to study the geometric structure of both single crystal surfaces and ordered phases of adsorbate overlayers under UHV conditions [105, 106]. In a LEED experiment an electron beam is coherently reflected from a sample surface to form a diffraction pattern on a phosphor screen. In a typical diffraction pattern, we are interested in the bright spots produced by the constructive interference of electrons from surface atoms. The position of these

* SAES Getters, S.P.A, <http://www.seasgetters.com>

bright spots provides information on the size, symmetry and rotational alignment of the 2-dimensional surface net of atoms on the sample surface.

According to the de Broglie relation, the wavelength and the momentum of the electrons can be related by the following equation:

$$\lambda = \frac{h}{p} \quad (3-7)$$

Where p is the electron momentum and can be represented non-relativistically as:

$$p = m \cdot v = \sqrt{2m(K_E)} = \sqrt{2m(eV)} \quad (3-8)$$

Where m is the mass of the electron, v is velocity, K_E is kinetic energy, e is electronic charge and V is the acceleration voltage. Using the Equation (3-7) and (3-8), the wavelength for the electron can be written as:

$$\lambda = \frac{h}{\sqrt{2m(eV)}} \quad (3-9)$$

A LEED instrument has a low energy electron gun that can produce electrons of kinetic energies ranging from 20 eV-200 eV. At these energies the mean free path for electrons is sufficiently short that they can only penetrate two or three atomic layers into the surface (5-10 Å) [107], and therefore the LEED pattern contains information on the surface atoms rather than the structure of the bulk.

The diffraction condition can be visualized in a graphical way by means of the Ewald sphere construction. The Ewald sphere is a geometric construct that demonstrates the relationship between the wavevector of the incident and diffracted x-ray beams. Assuming \mathbf{a} , \mathbf{b} and \mathbf{c} are the lattice vectors for the 3-dimensional unit cell at the crystal surface, the corresponding reciprocal lattice vectors \mathbf{a}^* , \mathbf{b}^* and \mathbf{c}^* are given by [108]:

$$a^* = 2\pi \frac{b \times c}{V} \quad b^* = 2\pi \frac{a \times c}{V} \quad c^* = 2\pi \frac{a \times b}{V} \quad V = a \cdot b \times c \quad (3-10)$$

To obtain a 2-d reciprocal lattice for a surface, let the base vector c approach infinity with the a and b vectors unchanged. As a result, the corresponding reciprocal lattice vector c^* approaches 0. The discrete points parallel to c^* in the reciprocal lattice will be infinitely close and appear as parallel lines, or rods, as shown in Figure 3.5, and the three-dimensional reciprocal lattice vector G_{hkl} reduces to G_{hk} in 2-d defined by:

$$G_{hk} = ha^* + kb^* \quad (3-11)$$

To a first approximation the LEED pattern is a Fourier transform of the real space surface lattice. We can define the incident wavevector of the electron as k_0 and the emerging wavevectors as k . For elastic scattering:

$$k_0^2 = k^2 \quad (3-12)$$

We can also define the component of the wavevector parallel to the surface as k^{\parallel} , and the component perpendicular to the surface as k^{\perp} . So, the condition for momentum conservation in the surface plane and constructive interference for 2-d diffraction becomes:

$$k^{\parallel} - k_0^{\parallel} = G_{hk} \quad (3-14)$$

A modified version of the Ewald sphere construction for 2-d lattice is shown in Figure 3.5.

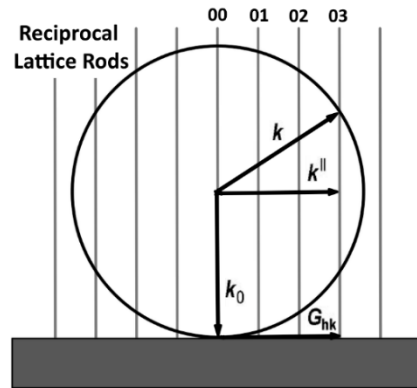


Figure 3.5. The Ewald sphere within the 2-d reciprocal lattice.

Constructive interference and a diffracted beam occurs wherever a reciprocal lattice rod intersects the surface of the Ewald sphere. The diffracted pattern thus reflects the symmetry of the surface unit cell.

For example, the deposition of a monolayer of silver atoms onto a clean Si(111) 7×7 surface held at 600°C results in a $\sqrt{3}\times\sqrt{3}$ $R30^\circ$ diffraction pattern as observed in Figure 3.6.

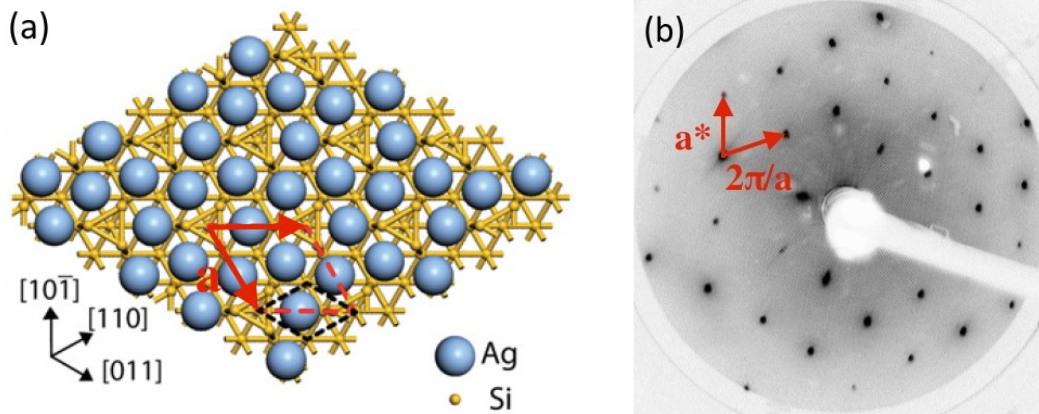


Figure 3. 6. (a) Si (111) $\sqrt{3}\times\sqrt{3}$ – Ag $R30^\circ$ reconstruction in real space. a is one of the unit vectors for $\sqrt{3}$ – Ag layer with a length of a . Graph reproduced from Murphy et al. (2012). (b) LEED diffraction pattern. a^* is one of the unit vectors in reciprocal space lattice, with a length of $2\pi/a$.

A schematic diagram of the LEED (purchased from OCI Vacuum^{*}) used in our laboratory is shown in Figure 3.7. An incident electron beam is produced by a tungsten filament and focused by a series of electrostatic lenses. The first grid of the screen and the last electrode of the electron gun are at the same potential as the sample, so that a field-free space is created for the incident and backscattered electrons to travel. The backscattered electrons are collected by a series of hemispherical grids. After the first grid, the second and third grids produce a retarding potential to reject any inelastically scattered electrons that contain no diffraction information. The elastically scattered electrons pass through the retarding field and are then accelerated by the fourth grid to the fluorescent screen to produce the observed diffraction pattern. In our case the pattern is recorded by a computer-controlled video camera purchased from Electrim Corporation[†].

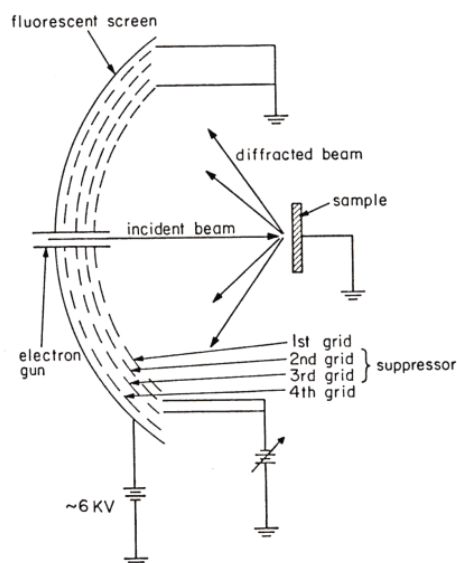


Figure 3.7. A LEED schematic diagram. Reproduced from Low-Energy Electron Diffraction: Experiment, Theory and Surface Structure Determination (VanHove *et al.* 1986).

^{*} OCI Vacuum Microengineering Inc. <http://www.ocivm.com>

[†] Electrim Corporation <http://www/electrim.com>

3.1.4 Auger Electron Spectroscopy (AES)

1) Auger Process

Auger electron spectroscopy is an analytical technique which provides information on the elemental makeup of the surface. An Auger process starts with an electron being ejected by an incident electron (or X-ray) beam to form a vacancy in an otherwise occupied level. To fill the vacancy a second electron from a higher orbital will fall into this state. To conserve energy, two possible processes can take place. The first is radiative via the emission of an x-ray photon, and the second is nonradiative, involving two electrons with one of these electrons (the Auger electron) ejected from the sample carrying the excess energy. (see Figure 3.8) The process illustrated in Figure 3.8 is a KL_2L_3 transition given the three electron energy levels involved.

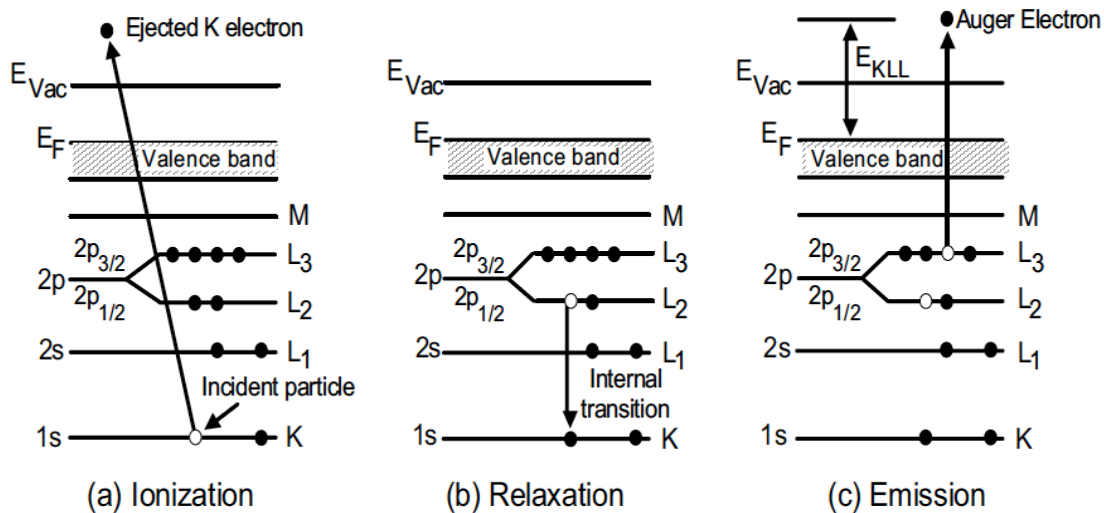


Figure 3.8. A schematic diagram of (a) the ejection of a K-shell electron followed by (b) and (c) a KL_2L_3 Auger transition. Graph reproduced from Handbook of Auger Electron Spectroscopy (Hedberg 1995).

2) Characteristic Auger Electron Energies

The kinetic energy of the Auger electron is approximately the energy difference between the energy lost by the electron making the transition into the vacancy and the energy of the electron shell from which

the Auger electron was ejected. Let E_a , E_b and E_c be the binding energy of electrons in a, b and c levels of the neutral atom respectively, the kinetic energy of the Auger electron can be expressed as:

$$KE = E_a - E_b - E_c - U. \quad (3-15)$$

Here, $E_a - E_b$ is the energy lost by the relaxed electron and E_c is the initial binding energy of the Auger electron. The U term lumps together the hole-hole interaction energy in the final state, and any screening, polarization and relaxation energies present [108]. From Equation (3-15), we see that the Auger electron has a discrete energy which is characteristic of the three energy levels involved of a specific atomic species. By measuring the characteristic kinetic energies of the Auger electrons we can make a spectroscopic identification of the element. For example, the Auger transition energy for the Si KLL transition is:

$$E_{KLL} \approx E_k - E_{L_1} - E_{L_{23}} \quad (3-16)$$

Due to the short mean free path of the relatively low energy Auger electrons, their mean free path in a solid is only a few nm and so Auger electrons can only be detected from atoms near the surface of the material of interest. Thus, AES is a surface sensitive technique.

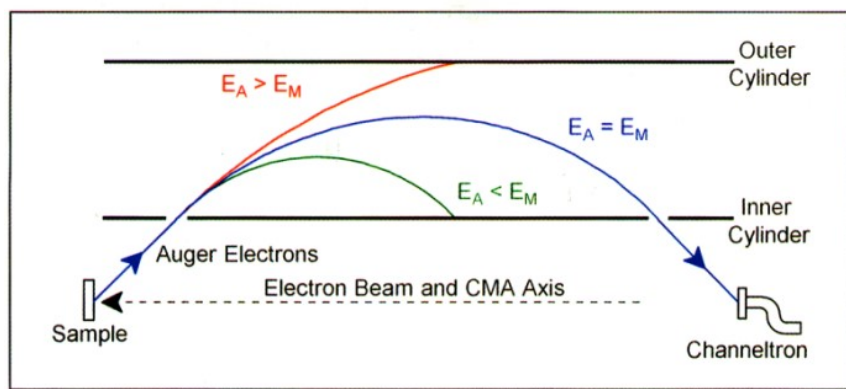


Figure 3.9. A schematic diagram for energy selectivity of the upper half of a cross section of a CMA. Reproduced from Handbook of Auger Electron Spectroscopy (Hedberg 1995).

3) Instrumentation and Spectra

The Auger spectrometer used in our laboratory is an Omicron CMA 100*. The spectrometer includes an integrated electron gun with a tungsten filament to provide a 3000eV electron beam. The electron analyzer is a Cylindrical Mirror Analyzer (CMA). The CMA consists of two coaxial cylinders with a negative potential applied to the outer cylinder and ground potential applied to the inner cylinder. When the electron beam hits the sample, any backscattered electrons which enter the CMA cylinder will be repelled by the negative potential on the outer cylinder and only electrons with the selected or “pass” energy will exit through a second aperture in the inner cylinder to the analyzer (see Figure 3.9). During the scanning process, the electron current as a function of “pass” energy is recorded and Auger transitions are measured.

In addition to Auger electrons, the measured electron current also includes contributions from secondary and backscattered electrons, and thus the signal can exhibit small, broad Auger peaks. For this reason, rather than plotting the number of electrons emitted as a function of the kinetic energy, $N(E)$, it is more common to plot the first derivative $dN(E)/dE$. Figure 3.10 (b) is an example of an Auger spectrum

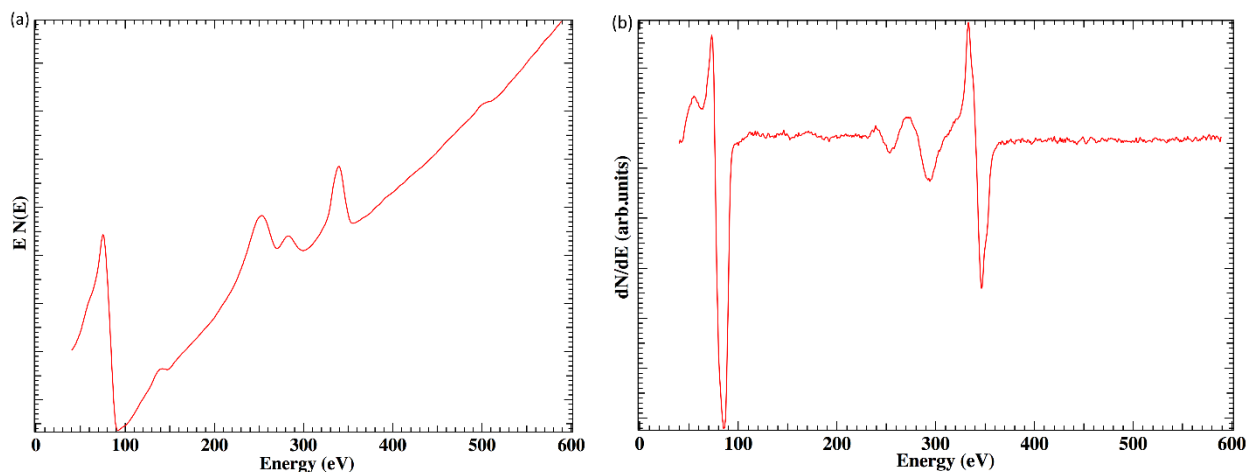


Figure 3.10. An Auger spectrum for one monolayer of Ag on Si(111) plotted as (a) intensity vs. energy and (b) the derivative dN/dE vs. energy.

* Omicron NanoTechnology GmbH. <http://www.omicron.de>

plotted using $dN(E)/dE$. By plotting the data in this mode, Auger transitions peaks are sharper and better defined.

3.1.5 Scanning Tunneling Microscopy (STM)

1) Introduction

STM, invented by Binnig and Rohrer (1982) at IBM [2], was the first Scanning probe microscopy (SPM) technique to be developed. Since its advent, STM has become one of the most powerful laboratory techniques for studies in surface science, and Binnig and Rohrer were awarded the Nobel prize in 1986 for their ground-breaking invention. STM is a surface sensitive, real-space analysis technique with a resolving power at the atomic level. Moreover, in addition to the topography of (semi) conducting surfaces, STM also provides information on the local electronic properties [108-112].

The operating principle: When a metal tip is brought extremely close to a (semi)conducting surface, i.e. within a few Ångströms, electrons can quantum mechanically tunnel from one to the other. The probability of tunneling is exponentially dependent on the separation. After a tunneling current is established, the tip must be scanned across the surface in an extremely precise manner using a crystal called a piezoelectric which changes its size by small amounts when an electric field is applied across it (Figure 3.11). In the case of a piezoelectric tube, the inner and outer surfaces of the surfaces are covered

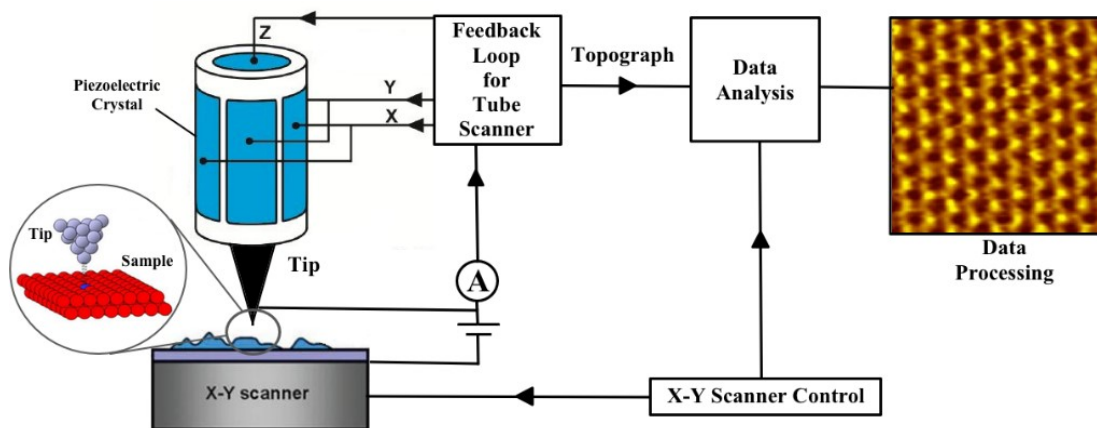


Figure 3.11. A schematic of the working principle of a STM.

by metal electrodes. Applying a voltage between the inner and outer electrodes results in an elongation/contraction in the Z-direction. The outer electrode is also divided into four sectors to allow deflection in X-Y. Applying a differential voltage between opposite sectors deflects the tube in either X or Y. The piezo sensitivities in the X and Y directions for our instrument are 51nm/V, and the sensitivity in Z is 5nm/V. With this precision, even the smallest details on the surface can be reflected as a large change in the tunneling current. STM data are recorded and presented as STM images with the help of specific software on a computer (Figure 3.11).

Tip preparation: the tip used in these experiments was an atomically sharp tungsten tip. A good tip is extremely crucial in our experiment since it directly determines the resolution and image quality. An ideal tip should terminate in a single atom. We used an electrochemical etching technique to produce the tip. A tungsten wire is placed into a solution of 1 molar NaOH and a negative potential is applied to a counter electrode (Figure 3.12). The tungsten wire etches and breaks at the air/solution interface which produces a ragged surface with a high probability of having a single atom at the endpoint. In fact, with a sharp enough tip, atomic scale resolution can be attained.

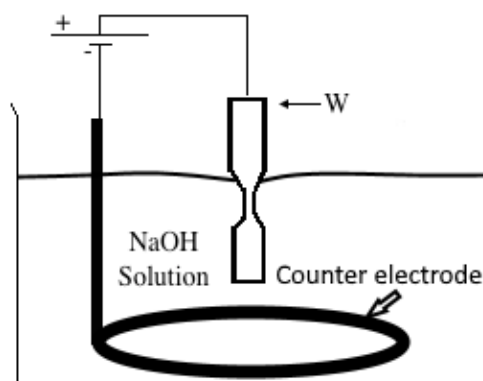


Figure 3.12. A schematic of apparatus for tip preparation setup.

Modes of operation: STM commonly operates in two different imaging modes: constant current mode and constant height mode (Figure 3.13).

In constant-current mode, which is the most widely used mode in STM operation, the tip is scanned over the surface while a feedback loop controls the height of the tip to maintain a constant tunneling current. As the magnitude of the tunneling current is small (a few nA or pA), it is amplified by a tunneling current amplifier prior to entering the feedback loop. The feedback keeps monitoring the tunneling current and adjusting the z position of the tip with respect to the sample by changing the voltage applied to the piezoelectric scanner, so as to maintain a constant tunneling current value. By recording the piezoelectric voltage and thus the height of the tip at each location of the scan area, a topographical image with atomic resolution can be obtained.

In the constant height mode the height of the tip above the surface is held constant and a record of the variation in the tunneling current is made. Variations depend on the topography and local electronic properties of surface. One major drawback of this mode is the risk of crashing the tip if the surface is not atomically flat.

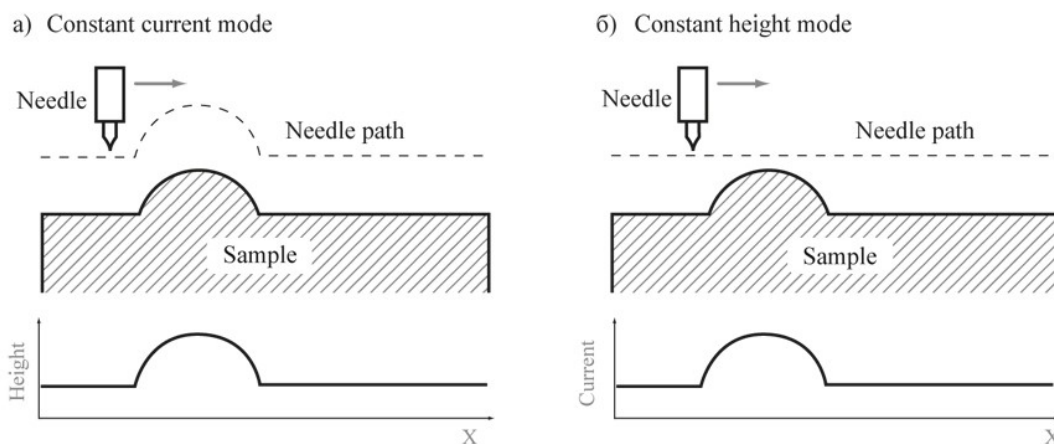


Figure 3.13. Schematic illustration of DTM imaging in (a) constant-current mode and (b) constant-height mode. Figure reproduced from Surface Science-An Introduction (K. Oura *et al.* 2003)

The STM used in our laboratory is an Omicron Micro* SPM and is controlled by RHK Technology† SPM 100 electronics. All the images are obtained in constant-current mode, at room temperature.

2) Tunneling Effect

As stated, the operation of an STM is based on quantum tunneling. In classical physics, particles with an energy less than a potential energy barrier are confined, however quantum mechanics predicts that if the mass of the object is small enough, and the barrier is thin and/or low enough, there is a finite probability that the electron will traverse the barrier. In one dimension, if we describe the electron using a wave function, the decaying solution for the electron wave function inside a rectangular barrier with a width d can be expressed as:

$$\Psi(d) = \Psi(0)e^{-\kappa d} \quad (3-17)$$

The probability of finding an electron beyond the barrier is

$$|\Psi(d)|^2 = |\Psi(0)|^2 e^{-2\kappa d} \quad (3-18)$$

where:

$$\kappa = \frac{\sqrt{2m(V-E)}}{\hbar} \quad (3-19)$$

here V is the height of the barrier and E is the energy of the electron.

* Omicron NanoTechnology GmbH. <http://www.omicron.de>

† RHK Technology. <http://www.rhk-tech.com>

In the case of STM, the vacuum space between the sample and tip acts as the potential barrier between the two electrodes (Figure 3.14(a)). When the sample and tip are electrically connected the Fermi levels align and the work function difference leads to an electric field in the barrier region (Figure 3.14(b)). The height of the barrier can be approximated by the average work function of the sample and tip. When a voltage is applied across the barrier, electrons on the negative side with an energy below the Fermi level can tunnel into the empty states on the positive side (Figure 3.14(c)).

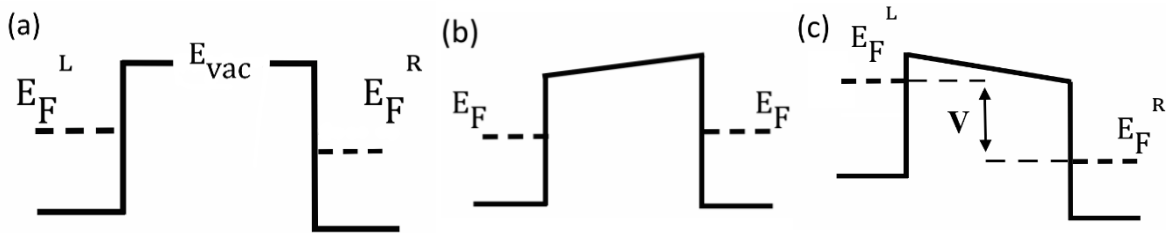


Figure 3.14. A schematic of the potential barrier between probe and surface for vacuum tunneling. (a) When separated the Fermi levels for the two materials differ due to the work function difference. (b) When the two parts are in electrical contact the Fermi levels align. (c) A voltage is applied; the electrons can tunnel in the range of energy indicated by the arrows.

It is known that the tunneling current at small bias and low temperature yields [113]:

$$I \propto e^{-2\kappa d} \quad (3-20)$$

Assuming a typical work function value of $5eV$, from the equation we find that at a typical tip-sample separation of $4 - 7\text{\AA}$ [114], a change of 1\AA in distance between two electrodes reduces the tunneling probability by an order of magnitude. This high sensitivity to separation makes it possible to measure the tip-sample movement very precisely, i.e. at an Ångstrom level. In practical operation, when the tip is scanning over the sample, a feedback controller is used to keep the tunneling current constant as the tip moves along the surface, thus providing a topographic map of the sample surface.

Tersoff and Hamann [115] developed a three dimensional theory for tunneling between a surface and a model tip in their 1985 paper. In this paper, they treat the surface ‘exactly’ and model the tip as a spherical potential well. According to Bardeen [116], the tunneling current can be expressed as:

$$I = \frac{2\pi e}{\hbar} \sum_{\mu, \nu} f(E_{\mu}) [1 - f(E_{\nu} + eV)] |M_{\mu\nu}|^2 \delta(E_{\mu} - E_{\nu}) \quad (3-21)$$

where $f(E)$ is the Fermi function, V is the voltage applied, E_{μ} and E_{ν} are the energies of state ψ_{μ} and ψ_{ν} in the absence of tunneling. $M_{\mu\nu}$ is the tunneling matrix element [116]:

$$M_{\mu\nu} = \frac{\hbar^2}{2m} \int dS \cdot (\psi_{\mu}^* \nabla \psi_{\nu} - \psi_{\nu} \nabla \psi_{\mu}^*) \quad (3-22)$$

where ψ_{μ} and ψ_{ν} are the single particle wavefunctions with respect to the two electrodes. The integral is over any surface lying entirely within the barrier separating the two sides. Though Equation (3-21) resembles first order perturbation theory, it is different in that ψ_{μ} and ψ_{ν} are nonorthogonal and solutions of different Hamiltonians. When the measurements are made at room temperature and at small voltages, we can take the limit of small voltage and temperature and rewrite the Equation (3-21) as:

$$I = \frac{2\pi}{\hbar} e^2 V \sum_{\mu, \nu} |M_{\mu\nu}|^2 \delta(E_{\mu} - E_F) \delta(E_{\nu} - E_F) \quad (3-23)$$

By treating the tip as a point probe, the tip wave functions are arbitrarily localized and the matrix element $M_{\mu\nu}$ is proportional to the amplitude of ψ_{ν} of the sample at position \vec{r}_0 of the tip, so Equation (3-21) can be expressed as:

$$I \propto \sum_{\nu} |\psi_{\nu}(\vec{r}_0)|^2 \delta(E_{\nu} - E_F) \quad (3-24)$$

Thus the current is proportional to the local density of states (LODS) of the sample at E_F at the position of the tip, and thus an STM image is a contour map of constant surface LDOS.

In order to solve Equation (3-23) in general we need to evaluate $M_{\mu\nu}$. Tersoff and Hamann [115] expanded the surface wavefunction as:

$$\psi_{\nu} = \Omega_s^{-1/2} \sum_G a_G \exp [(\kappa^2 + |\vec{\kappa}_G|^2)^{1/2} z] \exp (i\vec{\kappa}_G \cdot \vec{x}) \quad (3-25)$$

Where Ω_s is the sample volume, $\kappa = \hbar^{-1}(2m\phi)^{1/2}$, ϕ is the sample work function, and $\overline{\kappa_G} = \overline{k_{\parallel}} + \vec{G}$, where $\overline{k_{\parallel}}$ is the surface Bloch wave vector of the state and \vec{G} is a surface reciprocal-lattice vector.

Modeling the tip as a spherical potential well, the wave function of the tip is of the form:

$$\psi_{\mu} = \Omega_t^{-\frac{1}{2}} c_t \kappa R e^{\kappa R} (\kappa |\vec{r} - \vec{r}_0|)^{-1} e^{-\kappa |\vec{r} - \vec{r}_0|} \quad (3-26)$$

where Ω_t is the probe volume and κ is the same as in Equation (3-25). Using these wavefunctions Tersoff and Hamann [115] obtained:

$$M_{\mu\nu} = \frac{\hbar^2}{2m} 4\pi\kappa^{-1} \Omega_t^{-\frac{1}{2}} \kappa R e^{\kappa R} \psi_{\nu}(\vec{r}_0) \quad (3-27)$$

Where κ is the inverse decay length of the wavefunctions in vacuum, \vec{r}_0 is the position of the center of curvature of the tip. When substituting Equation (3-27) into Equation (3-23), the tunneling current yields:

$$I = 32\pi^3 \hbar^{-1} e^2 V \phi^2 D_t(E_F) R^2 \kappa^{-4} e^{2\kappa R} \times \sum_{\nu} |\psi_{\nu}(\vec{r}_0)|^2 \delta(E_{\nu} - E_F) \quad (3-28)$$

Where D_t is the density of states per unit volume of probe tip, ϕ is the work function and E_F is the Fermi level. As before the tunneling current is proportional to the surface LDOS.

3.2 Density Functional Theory (DFT)

DFT is a widely known quantum computational technique that gives a description of the ground state properties of an N-atom system using electron charge density [117]. In this thesis, in order to investigate the dimensional differences in the unit cell between our observed cell on Si(111) $\sqrt{3}$ -Ag surface and the cell observed on HOPG by Gatti *et al.* [118], DFT gas phase calculations were conducted. Usually, in self-assembled supramolecular nanostructures, the inter-molecular interactions are expected to dominate when compared with the molecule-substrate interactions. Therefore, we usually ignore the substrate and consider these nanostructures as ‘free standing films’ and modeled in the gas phase. Since calculations for

the entire layer are computationally unfeasible, a supramolecular structure composed of six monomers was used to model the unit cell. Starting with an optimized free-standing unit cell, we adjusted its size by constraining the distance between iodine atoms in four corners, allowing all other geometric parameters to relax. Geometric optimizations were carried out using Gaussian 09 [119]. The three cells we examined in this calculation are: a $1.77 \text{ nm} \times 1.77 \text{ nm}$ cell, a $2.42 \text{ nm} \times 1.77 \text{ nm}$ cell and a $2.42 \text{ nm} \times 2.42 \text{ nm}$ cell. These cells are the three closest commensurate configurations based on the dimensions of our observed cell ($2.07 \pm 0.05 \text{ nm} \times 1.83 \pm 0.05 \text{ nm}$).

All structures were optimized using the hybrid PBE1PBE functional [120] which combines exact Hartree-Fock (HF) exchange with Perdew-Burke-Ernzerhof (PBE) exchange, and uses the PBE correlation functional as formulated within generalized-gradient-approximation (GGA). A basis set is a set of functions used to describe the wavefunction or density. In this calculation, we used the Los Alamos National Laboratory Lanl2DZ basis sets [121-123], developed by Hay and Wadt. Using AIMALL [124], the quantum theory of atoms in molecules (QTAIM) was additionally applied with the aim of identifying the weak bonding interactions present in each hexamer. All calculations were performed using the orca cluster of SHARCNET and the graham cluster of ComputeCanada.

3.3 Sample Preparation

3.3.1 Si (111) $\sqrt{3} \times \sqrt{3}$ R30°-Ag

The Si(111) $\sqrt{3} \times \sqrt{3}$ R30° -Ag surface is obtained by depositing one monolayer of silver onto a clean Si(111) 7×7 surface. The wafers we use in our experiment are n-type Si(111) wafers, miscut by 1° towards $(\overline{112})$ and purchased from Sil'tronix Silicon Technologies*. The samples are mounted on a sample holder

* Sil'tronix Silicon Technologies. <http://www.sil-tronix-st.com>

outside the UHV chamber. Gloves are used to avoid contamination. The wafer is mounted stress free between two Tantalum coils. The sample holder consists of two metal pieces and was designed so that each side is electrically isolated from the other. The sample was mounted via the coils to bridge the two halves of the holder and permit current to flow through the sample. The current is used to heat the sample. The sample is introduced into the main chamber via the fast entry load lock.

The first step in our experiment is to obtain a Si(111) 7×7 surface. Initially the sample is degassed overnight at 690 °C. Since the size of each sample is different, we must find the heating currents to attain the required temperatures. An Ircon Ultimax Plus UX20P pyrometer* with an emissivity setting of 0.4 consistent with Petrovykh *et al.* is used to determine the currents necessary to attain 850, 1060 and 1160 °C [125].

To obtain a Si(111) 7×7 surface with an evenly spaced array of single height atomic steps we use a procedure based on a sequence outlined by Lin *et al.* [126]. The samples are flashed to 1160 °C for 10s to diffuse residual surface carbon into the bulk. The sample is then cooled to 1060 °C within 5s and held for 1 min, where single steps are stable. Finally, the temperature is quenched to 850°C and held for 1 minute. This quench to 850 °C avoids step tripling, and the 1 min anneal and slow cool down helps develop large 7×7 domains and kink-free step edges. LEED and AES are used to ensure long-range order.

After the Si(111) 7×7 surface is obtained, the second step is silver deposition. Silver films are evaporated from a Tantalum basket. The basket was degassed during the baking procedure mentioned previously. The $\sqrt{3} \times \sqrt{3}$ surface can be obtained by depositing 1 ML of Ag and annealing the sample to 600 °C. In this case one ML is defined as the areal density of unreconstructed Si atoms in the topmost layer of the (111) face which is 7.8×10^{14} atoms/cm². To deposit silver, the evaporator is brought up to

* Ircon. <http://www.ircon.com>

the evaporation temperature and preheated for 2 min to allow the flux to stabilize. Then the sample is exposed to the flux for the required time period. Following deposition, the sample is annealed for 2 minutes. LEED and AES are used to check the surface structure and the Ag coverage (Figure 3.15).

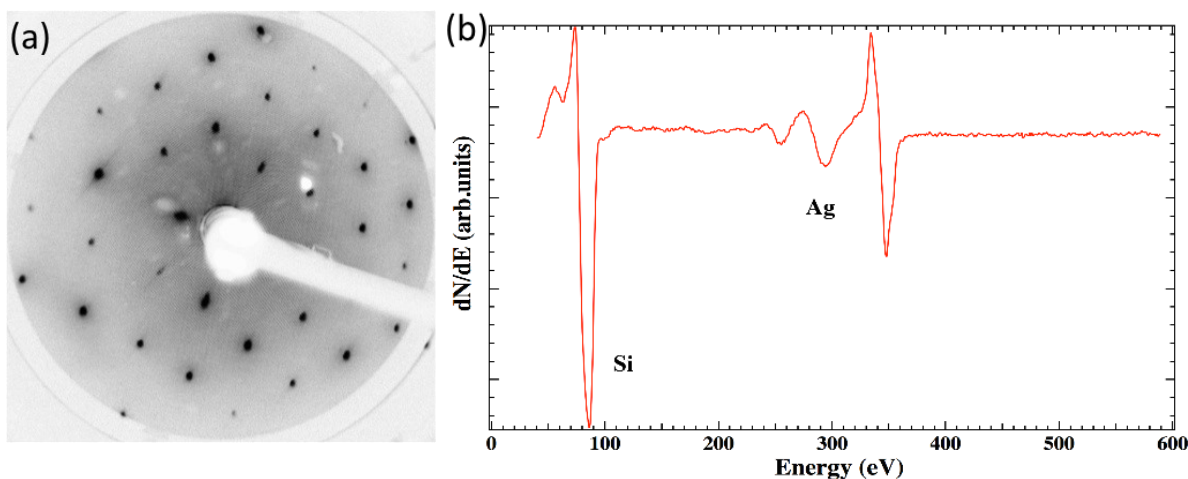


Figure 3.15. (a) A LEED diffraction pattern for the $\sqrt{3} \times \sqrt{3}$ - Ag surface, and (b) the corresponding Auger spectrum showing three Ag MNN transitions

3.3.2 Single Crystals

Au(111) and Ag(111) are the two single crystal surfaces we used in our experiments. A clean surface is obtained by sputtering off contaminants together with the top layers of the metal using noble gas ions (usually Ar^+). To produce an ion beam, Ar gas is leaked into the ion gun via a leak valve. The gas atoms are ionized by the electrons emitted by filament. The resultant ions are accelerated toward the extractor to form the beam and are directed at the sample.

Although ion sputtering is an efficient cleaning technique, one side-effect is degradation of the surface following bombardment. Therefore, subsequent annealing is required to restore the crystallography of the surface and remove Ar atoms. Usually, several sputter-anneal cycles are required to obtain a clean and well-ordered surface. Again, LEED and Auger are performed to ensure the quality of the surface.

3.3.3 Molecular Deposition

The last preparation step in our experiments is molecular deposition. The molecules of interest are placed in an Alumina crucible, which is heated by a tungsten filament. The evaporator we use in our laboratory is an evaporator manufactured by Tectra*. Figure 3.16 is a photograph of the molecular evaporator which shows the components.

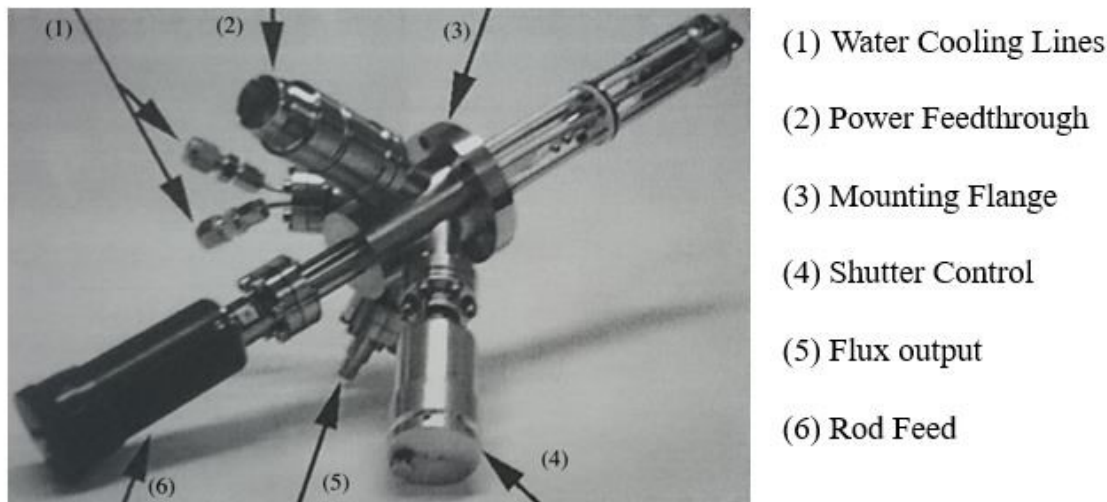


Figure 3.16. A photograph of the molecular evaporator.

The filament is surrounded by a water-cooled copper shroud to shield the chamber from thermal radiation, and to limit the spread of sublimated molecules. A type C thermocouple is connected to monitor the temperature close to the crucible, although the true temperature of the crucible is significantly higher.

We use the following sequence to deposit the molecules. The crucible is preheated to the desired temperature for molecule under study (90 °C for TBTTA, 70 °C for TIPT, 50 °C for TBTANG, all readings are obtained by the thermocouple). At this point the shutter is opened and the sample is exposed to the molecular flux. Following exposure, AES is used to determine the molecular coverage.

* tec tra. <http://www.tecra.de>

Chapter 4

Supramolecular structures of TBTTA on the Si(111) $\sqrt{3}\times\sqrt{3}R30^\circ$ -Ag surface*

* Published result: *Surface Science*, **647** (2016) 51-54.

4.1 Introduction

Two-dimensional (2-d) molecular networks can be used as active layers in hybrid electronic devices. Hybrid devices which combine organic layers with silicon promise a wide variety of functionality incorporated within existing Si electronics technology. A fundamental requirement for hybrid devices is well-defined morphology at the interface to allow for efficient electronic coupling between materials. Although there are many examples of ordered organic supramolecular layers on metal surfaces, such self-assembled structures are significantly more difficult to achieve on Si surfaces since the surfaces are considerably more reactive to organic molecules. For example, STM measurements indicate that thiophene adsorbs onto the Si(111) 7×7 surface via a $[4 + 2]$ cycloaddition reaction [127]. To overcome this reactivity, one approach is to passivate the Si surface to allow for supramolecular ordering of 2-d organic films [26, 128-132].

Supramolecular self-assembly on surfaces is driven by molecule surface and intermolecular interactions. Recently, it has been demonstrated that halogen bonding can drive the self-assembly of organic molecules on metal surfaces [10, 69, 133-136], highly ordered pyrolytic graphite (HOPG) [137-139], and on passivated silicon surfaces [131, 140].

Due in part to efficient electronic conjugation and chemical stability, thiophene-based oligomers have found particular application in organic electronics [85, 141]. For example, poly(3,4-ethylenedioxythiophene), PEDOT, is one of the most industrially important organic conductors, and some thiophene-based semiconductors exhibit hole mobilities up to $\sim 20 \text{ cm}^2 \text{ V}^{-1} \text{ s}^{-1}$ in organic field effect transistors (OFETS) [142-144]. Understanding how thiophene-based building blocks self-assemble onto semiconducting solids, particularly at the interface with other materials (electrodes and dielectrics) is of paramount importance for further progress in the field.

In this chapter, we use STM to study the room temperature adsorption of an organic molecule, tetrabromotetrathienoanthracene (TBTTA) [145] onto a passivated silicon surface. TBTTA, a thiophene based organic molecule with four thiophene rings at the four corners (Figure 4.1), is known to form a halogen-bonded supramolecular layer on HOPG [137], and a π -conjugated 2-d polymer on the Ag(111) surface [146]. The suitability of the Si(111) $\sqrt{3}$ -Ag surface for the growth of hybrid organic-silicon devices is investigated.

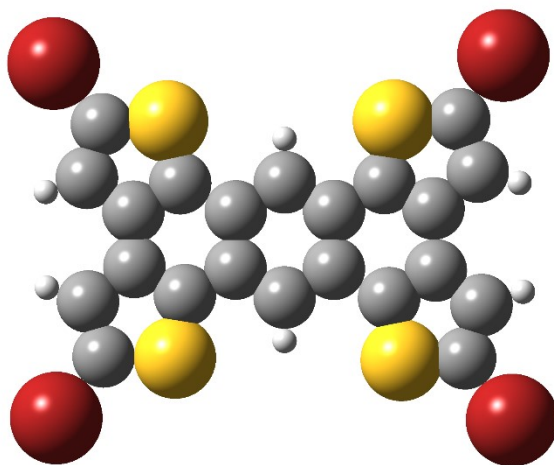


Figure 4.1. The molecular structure of TBTTA. Bromine atoms are indicated in red, carbon atoms in grey, sulfur atoms in yellow and hydrogen atoms in white.

4.2 Experiment

All measurements are performed in a single UHV system with a base pressure of approximately 2×10^{-10} Torr. The annealing sequence is based on a sample cleaning procedure outlined by Viernow *et al.* [147]. Detailed information on sample preparation, techniques used for surface quality assessment, and STM scanning can be found in Section 3.2.

The $\sqrt{3}$ layer is formed by exposing the silicon surface to a net Ag coverage of 1 ML (1ML is defined as 7.8×10^{14} Ag atoms/cm²). The Ag is evaporated from a tantalum basket and, following deposition, the

sample is annealed at 580 °C for 2 min. The resultant surface yields a strong $\sqrt{3}$ diffraction pattern as observed in LEED.

The TBTTA molecules are provided by collaborators and synthesized according to the procedures described by Brusso *et al.* [145]. To deposit TBTTA onto the Si(111) $\sqrt{3}$ -Ag surface, the molecules are sublimed *in-situ* from an alumina crucible onto the sample held at room temperature. The molecular coverage is monitored using AES. The AES spectra reveal an LMM transition at 153 eV due to sulfur, and a carbon KLL transition at 272 eV. However, the KLL transition overlaps a silver transition (MNN) at 351 eV. A rough estimate of the molecular coverage is made by comparing the change in amplitude of the sulfur peak with respect to the silicon LMM transition at 96 eV, Figure 4.2. Bromine also exhibits an Auger transition at 1393 eV; however, this peak was not tracked due to the low signal strength. STM measurements are performed at room temperature using electrochemically etched W tips. STM images

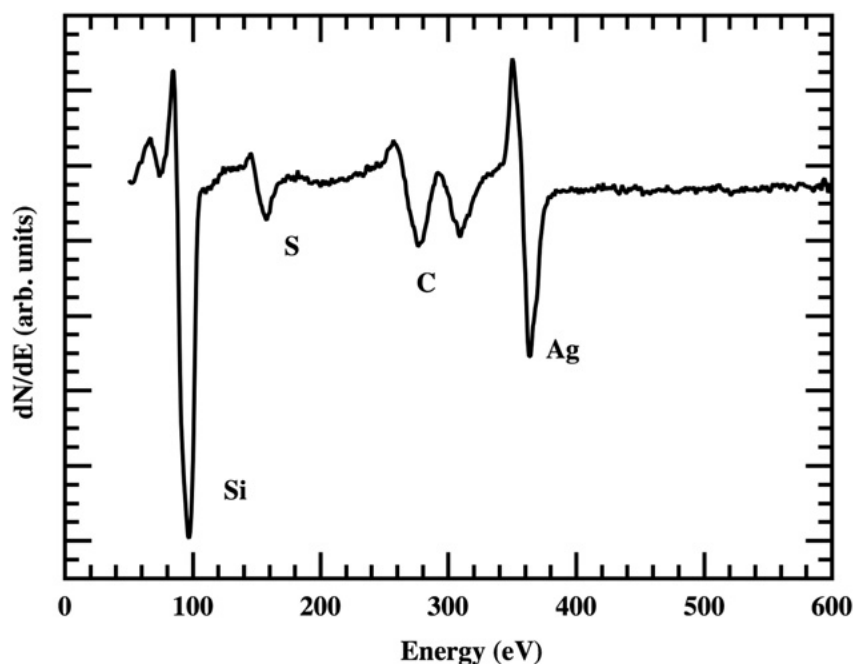


Figure 4.2. An Auger spectrum of a TBTTA covered Si(111) $\sqrt{3} \times \sqrt{3}$ -Ag surface. The size of the sulfur LMM transition at 153 eV relative to the silicon transition at 96 eV was used as an estimate of the molecular coverage.

are obtained using an Omicron Micro SPM* with RHK SPM100† control electronics and all images are taken in constant current mode at room temperature.

4.3 Results and Discussion

The annealed (111) surface of silicon is 7×7 reconstructed and the unit cell contains 19 silicon dangling bonds [33]. The adsorption of oligothiophenes on Si(111) surfaces has rarely been studied due to the fact that thiophene forms covalent bonds with Si surface atoms [127, 148]. To passivate the (111) surface, we adsorb 1 ML of Ag to form a $\sqrt{3} \times \sqrt{3}$ R30° reconstruction. According to the honeycomb chain trimer (HCT) model of the $\sqrt{3}$ reconstruction [36], one monolayer of Ag binds covalently to the Si surface atoms leaving no dangling bonds. An STM image of the Si(111) $\sqrt{3}$ -Ag surface is shown in

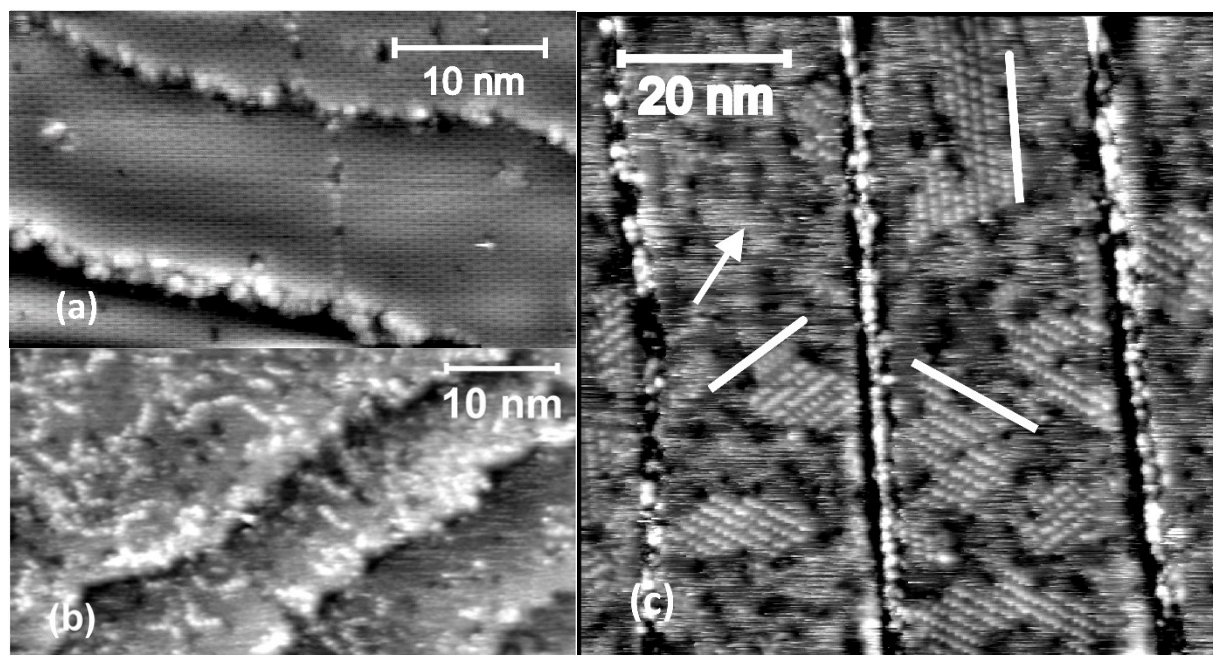


Figure 4.3. (a) An STM image of the $\sqrt{3} \times \sqrt{3}$ -Ag surface ($V_{\text{sample}} = -0.9$ V, $I = 300$ pA). (b) At low coverage, the TBTTA molecules form 1-d structures on the $\sqrt{3}$ -Ag surface ($V_{\text{sample}} = 1.7$ V, $I = 400$ pA). (c) At higher coverage ($V_{\text{sample}} = 1.2$ V, $I = 110$ pA), ordered TBTTA superstructures are formed. The image includes three $\sqrt{3}$ terraces separated by Si atomic steps extending vertically. The horizontal streaks (see arrow) are due to diffusing molecules. The ordered supramolecular islands exist in one of three rotational directions (see white lines).

* Omicron NanoTechnology GmbH. <http://www.omicron.de>

† RHK Technology. <http://www.rhk-tech.com>

Figure 4.3(a). The image reveals the hexagonal $\sqrt{3}$ surface reconstruction in addition to a number of point defects, and a disordered region adjacent to the step edge on the lower terrace which we believe can be attributed to a small amount of contamination.

The data indicates that TBTTA monomers are quite mobile on the Si(111) $\sqrt{3}$ -Ag surface at room temperature. We find no ordered molecular structures at low coverage, however individual molecules are distinguishable, as are small, predominantly chain-like islands (Figure 4.3(b)). These islands are dynamic, and the adsorbed molecules readily migrate and accumulate at step edges or defects in the $\sqrt{3}$ -Ag structure. With increasing TBTTA coverage, more stable 2-d islands are formed (Figure 4.3(c)). Many of the STM images of surfaces with non-zero TBTTA coverage exhibit horizontal bright streaks (Figure 4.3(b) and (c)). This apparent ‘noise’ is attributed to diffusing molecules which remain trapped below the tip during scanning along the fast scan direction [149]. We also observe temporal changes in the STM scans on the order of minutes and can discern the attachment and detachment of TBTTA monomers at the perimeter of supramolecular structures into the 2-d molecular gas on the surface. The dynamic behavior indicates both

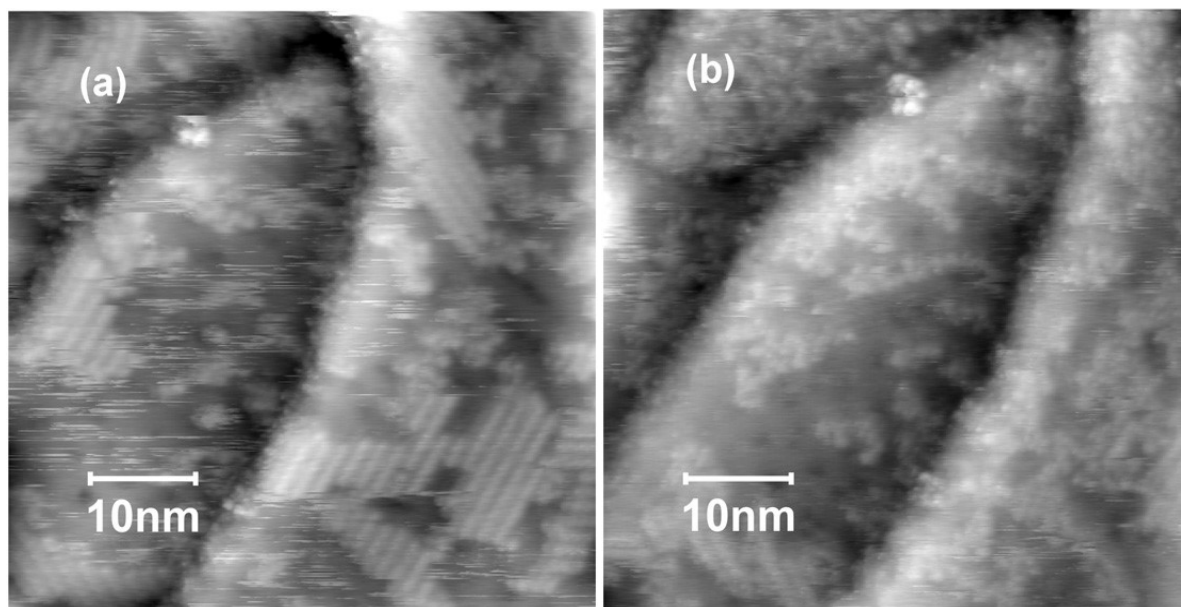


Figure 4.4. Two images taken consecutively in the same region at higher bias. The first image (a), exhibits several ordered molecular islands. After several scans (b), it is apparent that some of these islands have completely decomposed ($V_{\text{sample}} = 1.6 \text{ V}$, $I = 110 \text{ pA}$).

a relatively weak energy for molecular attachment/detachment at the supramolecular domains, and a relatively high mobility for TBTTA monomers on the Si(111) $\sqrt{3}$ -Ag surface.

The supramolecular structures are also quite sensitive to changes in STM bias conditions (Figure 4.4). We observe that the ordered supramolecular domains can decompose when imaged under high bias ($|V_{\text{sample}}| > 2 \text{ V}$) or low ($|V_{\text{sample}}| < 0.7 \text{ V}$) conditions, even though the specific values vary depending on tip conditions. At high bias, we believe the increased electric field leads to the dissolution of the superstructures, whereas at low bias, the monomers are swept away due to physical interactions with the tip. We have no evidence to suggest that the high bias tunneling conditions can induce any chemical changes in the TBTTA monomers. For example, we did not observe the formation of metal-organic or covalent structures of the type seen on the Ag(111) surface following dehalogenation [146]. The bias dependence provides further evidence that the supramolecular domains are weakly held together.

The ordered TBTTA domains can be defined by an oblique primitive cell with a long side of $(1.7 \pm 0.1) \text{ nm}$, a short side of $(1.1 \pm 0.1) \text{ nm}$, and an angle of (113 ± 2) degrees (Figure 4.5(b)). We are not able to obtain sub-molecular resolution in our room temperature measurements; therefore, we cannot experimentally determine the orientation of the TBTTA monomers within the unit cell. In the ball and stick model displayed in Figure 4.5(b), we have assumed a singular orientation and the specific choice displayed is based on DFT calculations for a free-standing TBTTA layer [137] to be discussed. The supramolecular domains exhibit a definite epitaxial relationship with respect to the underlying lattice: the long axis of unit cells are rotated by 40 ± 2 degrees with respect to one of the three high-symmetry $\sqrt{3}$ directions. Therefore, we observe three rotational domains (highlighted in Figure 4.3(c)) consistent with the C_{3v} symmetry of the substrate. The epitaxial relationship also points to the possibility of a commensurate overlayer. Within experimental error, the measured unit cell dimensions are consistent with

a commensurate cell defined by vectors $\mathbf{a}_m = 3\mathbf{a}_{\sqrt{3}} + 2\mathbf{b}_{\sqrt{3}}$, and $\mathbf{b}_m = -\mathbf{a}_{\sqrt{3}} + \mathbf{b}_{\sqrt{3}}$, where $|\mathbf{a}_{\sqrt{3}}| = |\mathbf{b}_{\sqrt{3}}| = 0.67$ nm. Expressing the commensurate cell in matrix form yields:

$$\begin{pmatrix} \mathbf{a}_m \\ \mathbf{b}_m \end{pmatrix} = \begin{pmatrix} 3 & 2 \\ -1 & 1 \end{pmatrix} \begin{pmatrix} \mathbf{a}_{\sqrt{3}} \\ \mathbf{b}_{\sqrt{3}} \end{pmatrix}$$

With increasing coverage, the size and stability of the supramolecular domains increases. Figure 4.5(b) includes a supramolecular island and bare patches exposing the underlying Si(111) $\sqrt{3}$ -Ag substrate. On closer inspection, the structural domains often terminate or have voids when they encounter defects, domain boundaries, or point defects in the underlying $\sqrt{3}$ -Ag layer (see arrows). It is apparent that defects in the $\sqrt{3}$ reconstruction can limit the extent of the supramolecular domains.

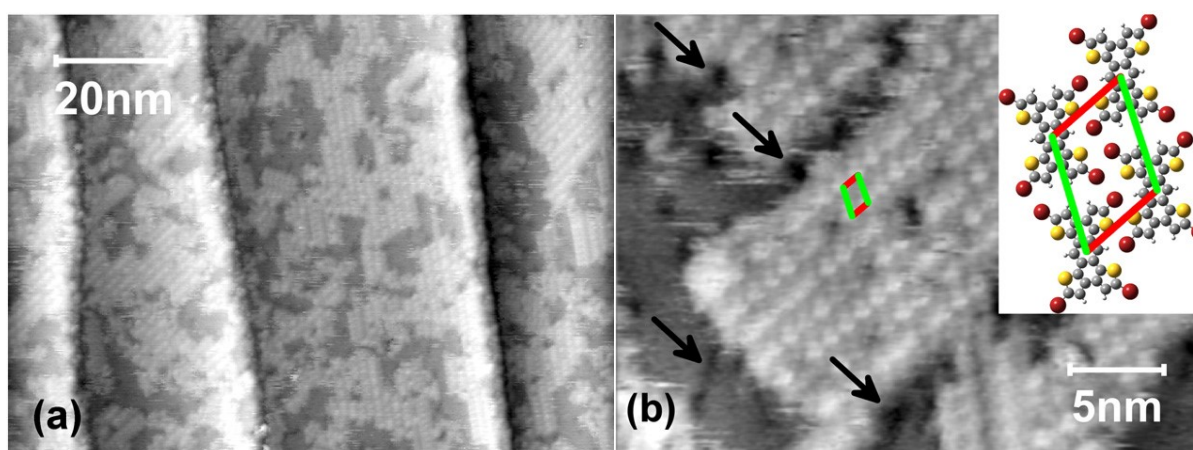


Figure 4.5. STM images of TBTTA superstructures on the $\sqrt{3}$ surface ($V_{\text{sample}} = -1.11$ V, $I = 0.5$ nA). The image in (a) reveals four TBTTA-covered $\sqrt{3}$ terraces separated by single height Si atomic steps running vertically in the image. The zoomed-in image (b) highlights both the unit cell and defects in the $\sqrt{3}$ structure (arrows), which appear to limit the extent of the TBTTA domain.

Gutzler *et al.* investigated the structure of TBTTA layers at the liquid–solid interface [137]. It was observed that TBTTA molecules form a highly ordered 2-d network with an oblique unit cell (1.5 ± 0.1) nm, by (1.1 ± 0.1) nm, with an angle of 114 degrees at the highly oriented pyrolytic graphite (HOPG), 1,2,4-trichlorobenzene interface. They also performed DFT calculations to gain insight into the intermolecular binding of this TBTTA layer and identified non-covalent halogen bonding between monomers as the primary interaction driving the self-assembly in the supramolecular layer.

The unit cell we observe on the Si(111) $\sqrt{3}$ -Ag surface is similar to both the observed cell on HOPG, and the DFT optimized cell [137]. The two experimental cells agree within error, i.e. long side (1.7 ± 0.1) nm on Si(111) $\sqrt{3}$ -Ag versus (1.5 ± 0.1) nm on HOPG; the short side (1.1 ± 0.1) nm versus (1.1 ± 0.1) nm, and an angle of (113 ± 2) ° compared to 114 ° on HOPG. The similarity is striking considering the fact that the two underlying substrates have very different lattice vectors (0.25 nm for HOPG versus 0.67 nm for the Si(111) $\sqrt{3}$ -Ag surface), and surface chemistry. The similarity is a strong indication that the size and symmetry of the TBTTA overlayer on the Si(111) $\sqrt{3}$ -Ag surface is also determined primarily by intermolecular interactions and that the substrate only plays a secondary role, i.e. in orienting the domains. Based on the similarity with HOPG, we conclude that debromination of TBTTA does not occur at room temperature, but rather, intact monomers form 2-d supramolecular domains on the silver terminated silicon surface. Indeed, we have found no experimental evidence of dehalogenation. In contrast, debromination of TBTTA occurs readily on the close-packed Ag(111) surfaces at room temperature [19], and the resultant TTA monomers form a 2-d organometallic network (TTA-Ag-TTA).

4.4 Summary

We find that the Si(111) $\sqrt{3}$ -Ag surface provides an inert, high-mobility template for TBTTA adsorption. At low coverage, TBTTA monomers readily diffuse to step edges and defects in the $\sqrt{3}$ -Ag overlayer and STM images show direct evidence of molecular diffusion at room temperature. At higher coverage, supramolecular structures are formed with an oblique unit cell defined by lattice vectors of (1.7 ± 0.1) nm and (1.0 ± 0.1) nm and an angle of 113 °. The domains exhibit a definite epitaxial relationship to the substrate. The long axis of the unit cell is rotated by 40 ± 2 ° with respect to one of the high-symmetry directions of the substrate. With increasing coverage, we find that the size of the supramolecular domains is often limited by defects in the underlying Si(111) $\sqrt{3}$ -Ag substrate.

Temporal changes and bias-dependent effects indicate that these structures are quite fragile and lack strong intermolecular interactions. The dimensions of the oblique unit cell we observe are similar to the energy minimized structure of a free-standing TBTTA layer obtained by DFT [137] and provides strong evidence that the monomers do not undergo debromination, remain intact, and that the dominant interaction within the domains is intermolecular halogen bonding.

The Si(111) $\sqrt{3}\times\sqrt{3}R30^\circ$ -Ag reconstruction successfully eliminates any covalent interactions between the silicon surface and the oligothiophene molecules. Ordered molecular domains are held together by weak intermolecular bonding. In fact, silver passivation of the Si(111) surface yields a surface which is less reactive to TBTTA monomers than the close packed Ag(111) surface [146]. These results suggest that the Si(111) $\sqrt{3}$ -Ag surface may indeed be an ideal template to explore the molecular self-assembly of halogenated oligothiophene layers with potential application in hybrid organic silicon devices.

Chapter 5

Adsorption of TIPT on Si(111) $\sqrt{3}\times\sqrt{3}R30^\circ$ -Ag and Ag(111)

5.1 Introduction

It has been shown that halogen···halogen interactions can stabilize two-dimensional (2-d) supramolecular networks on inert surfaces [118]. In chapter 4, we reported that the high-mobility of the Si(111) $\sqrt{3}$ -Ag surfaces extends to the adsorption of halogenated organic molecules. As discussed in Chapter 2, one approach to surface confined polymerization is the adsorption of halogenated aromatic precursors onto an atomically flat single-crystal surface. The surface can act to both catalyze the dehalogenation of the aryl-halide, and also confine the subsequent polymerization reaction in two dimensions [18, 150, 151].

Although a number of examples of 2-d polymerization on single crystal metal surfaces have been reported [15-19], very limited work has been done to explore surface confined polymerization on semiconducting surfaces such as silicon. As concluded in Chapter 4, the Si(111) $\sqrt{3}$ -Ag surface is weakly interacting, allowing halogenated organic molecules to remain mobile and interact with each other to create well-ordered overlayers. Well-ordered organic films have been reported on this substrate for several organic molecules [22-26]. An active polymer layer on a silicon surface could form the basis of a hybrid device which could be incorporated into existing Si electronics technology [20, 21].

In this chapter, we compare the adsorption of the halogenated organic molecule 2,4,6-tris(4-iodophenyl)-1,3,5-triazine (TIPT, see Figure 5.1) onto two related surfaces, Ag(111) and the Si(111) $\sqrt{3}$ -Ag surface. The experiments are performed in UHV using room temperature STM, to study the effect of the substrate on the adsorption. TIPT was chosen because it forms a high quality self-assembled molecular network (SAMN) on both HOPG and Au(111) surfaces, and it also forms a 2-d polymer layer on the Cu(111) and Ag(111) surfaces which has been reported by Gianluca et al. [152]. We reproduced the polymerization results on Ag(111) so as to compare with our results on Si(111) $\sqrt{3}$ -Ag.

Moreover, TIPT features a triazine core which includes 3 nitrogen atoms. Triazine based compounds are considered effective electron-transport materials and have been used broadly in organic light-emitting diodes (OLEDs) [153].

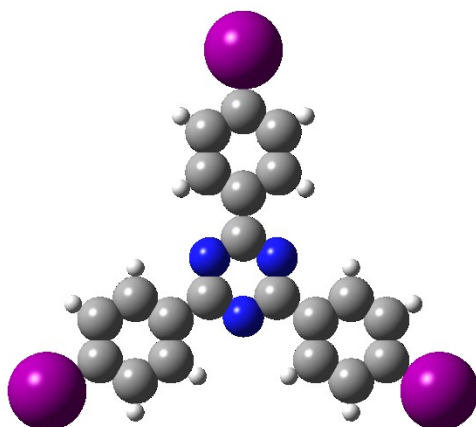


Figure 5.1. The molecular structure of TIPT. Iodine atoms are indicated in purple, carbon atoms in grey, nitrogen atoms in blue and hydrogen atoms in white.

5.2 Experiment

All experiments are performed in a single UHV system discussed previously. Detailed information on sample preparation, techniques used for surface quality assessment, and STM scanning can be found in Section 4.2. A clean Ag(111) single crystal was prepared by repeated cycles of sputtering with Ar⁺ ions and annealing at approximately 330 °C.

The efficacy of this sputter-anneal cycle was verified by AES and LEED.

TIPT deposition

TIPT molecule are synthesized and supplied by collaborators at McGill University. To deposit the TIPT monomers onto the Si(111) $\sqrt{3}$ -Ag and Ag(111) surfaces, the molecules are sublimed *in-situ* from a boron-nitride crucible onto samples at ambient temperature. Molecular deposition is confirmed using AES.

For TIPT on the Si(111) $\sqrt{3}$ -Ag surface, AES spectra reveal an iodine MNN transition at 519 eV, and a carbon KLL transition at 272 eV (Figure 5.2). The carbon transition is partially masked by a silver MNN transition at 351 eV. A crude indicator of molecular coverage is determined by monitoring the change in amplitude of the iodine peak with respect to the silicon LMM transition at 96 eV. A small nitrogen Auger transition at 389 eV is also observed, however this peak was not tracked due to the low signal strength.

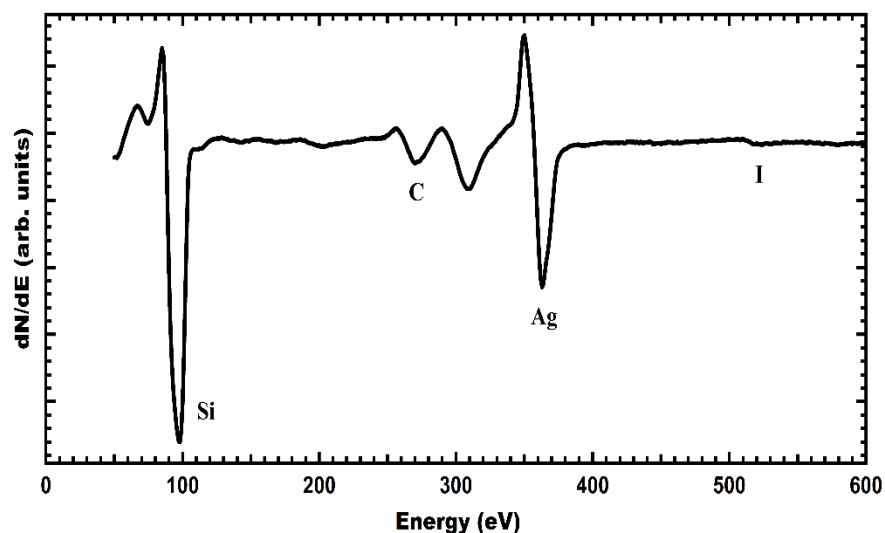


Figure 5.2. An Auger spectrum of a TIPT covered Si(111) $\sqrt{3} \times \sqrt{3}$ -Ag surface. The size of the I MNN transition at 519 eV relative to the silicon transition at 96 eV was used as an estimate of the molecular coverage.

For TIPT on Ag(111), the MNN transition from the silver substrate is substantially stronger than the transition from the single layer silver on Si(111) $\sqrt{3}$ -Ag, and thus the carbon peak from the TIPT molecule is entirely masked. Similarly, the iodine peak is partially masked by an oxygen KLL transition at 509 eV (Figure 5.3). Actually, the small oxygen signal exists prior to molecular deposition and we believe this can be attributed to sample holder.

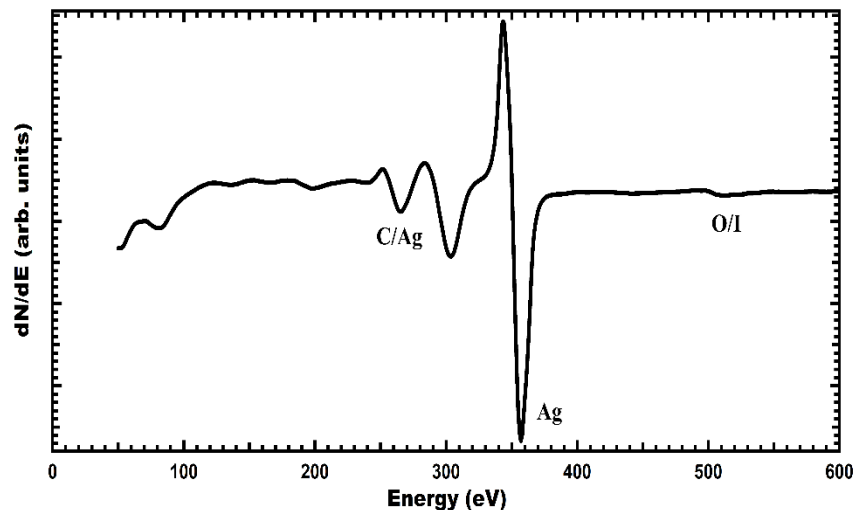


Figure 5.3. An Auger spectrum of a TIPT covered Ag(111) surface.

5.3 Results and Discussion

5.3.1 Adsorption of TIPT on Ag(111)

1) Molecular Adsorption with Substrate at RT

The following Figures are examples of STM images of TIPT molecules deposited on the Ag(111) surface at different coverage, a lower coverage region (Figure 5.4, approximately 0.47ML) and a higher coverage region (Figure 5.5, approximately 0.94ML). In both images, open-pore networks of TIPT can be clearly identified. These networks are composed of polygons, predominantly hexagons and pentagons but also heptagons and octagons.

As seen in Figure 5.4, on closer inspection of the TIPT network, we can clearly discern bright protrusions (red arrow in Figure 5.4) between adjacent TIPT monomers. These bright features are attributed to single silver atoms which coordinate two (and occasionally three) radicals. These organometallic structures consist of non-ordered dehalogenated molecules connected via Ag adatoms of the surface. Those structures have also been referred to as “*proto-polymers*” in similar systems

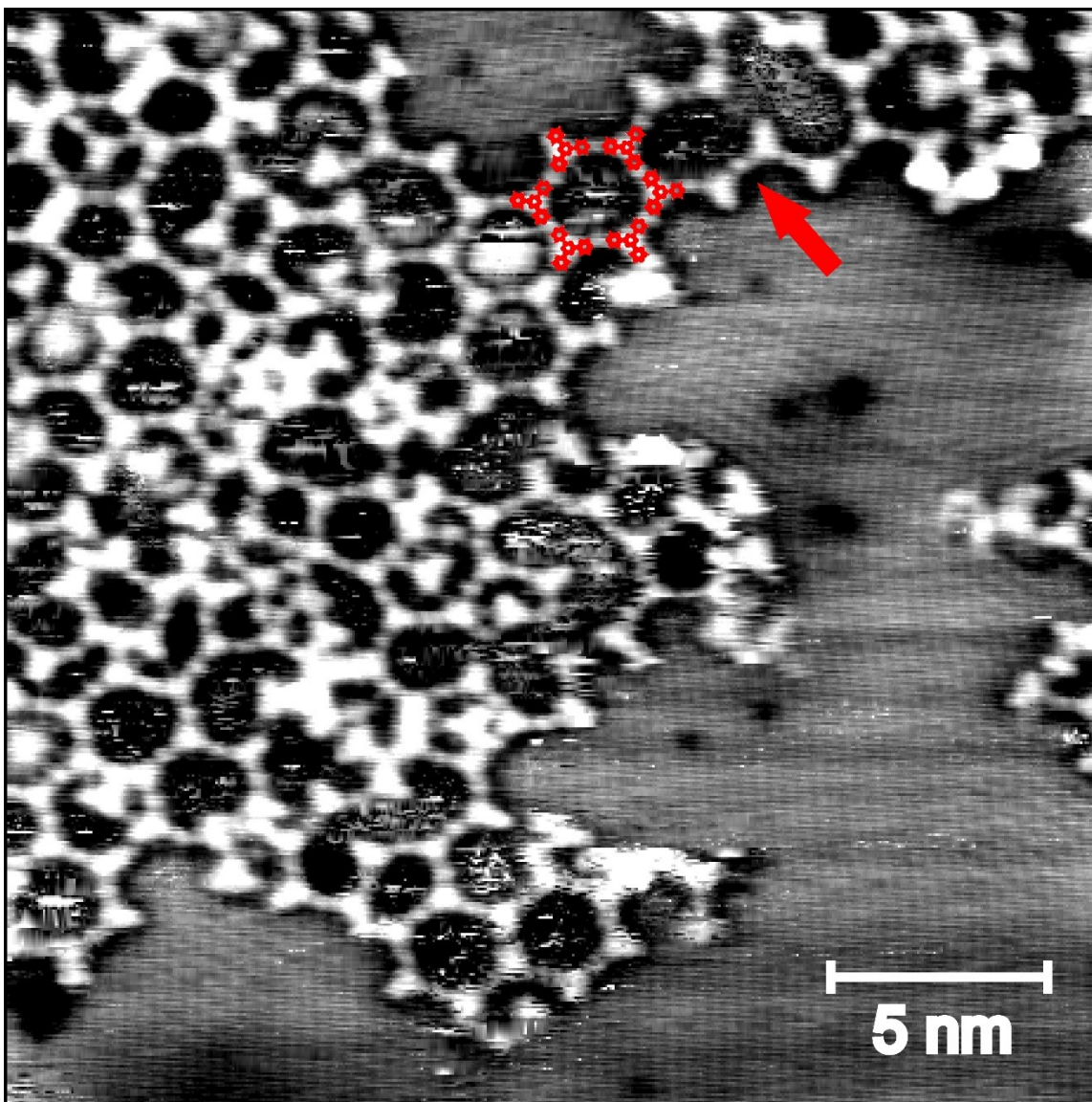


Figure 5.4. STM image Ag(111) surface with lower TIPT coverage. Both opened and closed structures formed by TIPT can be observed. Metallic atoms can be identified at the edge of each molecules. Single molecules are overlapped by TIPT monomers masked in red.

[17, 154, 155]. Other than the molecular structures, we also observed some “corrugations” in the background. We believe these features are due to the diffusing iodine atoms that are liberated after dehalogenation.

Figure 5.5 shows that a region close to the step edge has a relatively higher TIPT coverage. We believe this higher coverage is due to preferred nucleation at the step edge. Free radicals are more likely to attach and initiate growth at step edges [99].

Despite the increased number of molecules on the surface, Figure 5.5 also indicates a high defect density and irregularity in the molecular connectivity in the region. In addition to the open-pore network, we find a large number of dimers and open structures formed on the surface (highlighted by red frames in Figure 5.5).

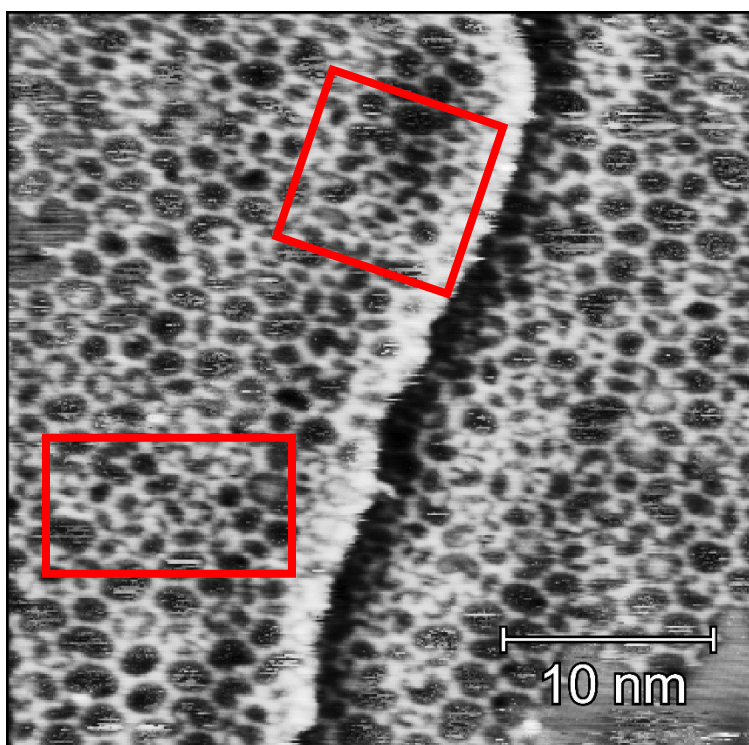


Figure 5.5. An STM image of the Ag(111) surface with higher TIPT coverage. A large number of molecules and higher defect density is observed.

2) Organometallic TIPT Structures on Ag(111)

In order to gain a deeper insight into the character of the TIPT organometallic structures on Ag(111), a high resolution STM image of the organometallic TIPT clusters formed on Ag(111) surface is presented in Figure 5.6(a). This image has a scan area of 3.5 nm by 3.5 nm. At this scale, we can easily identify two

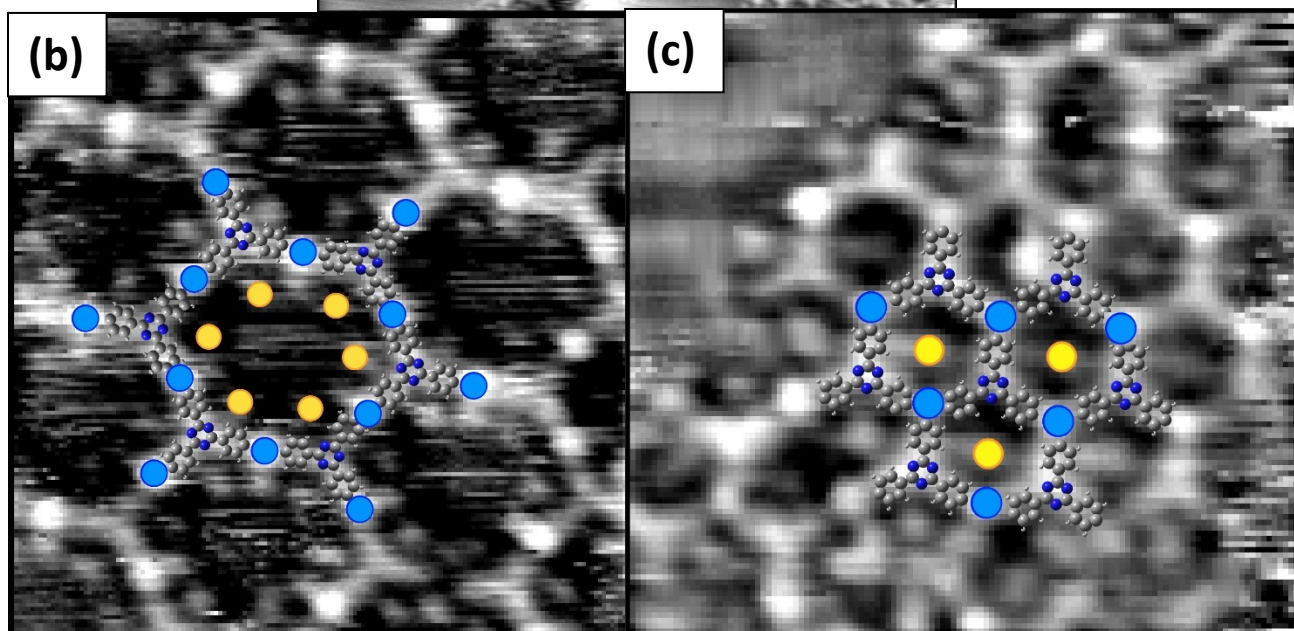
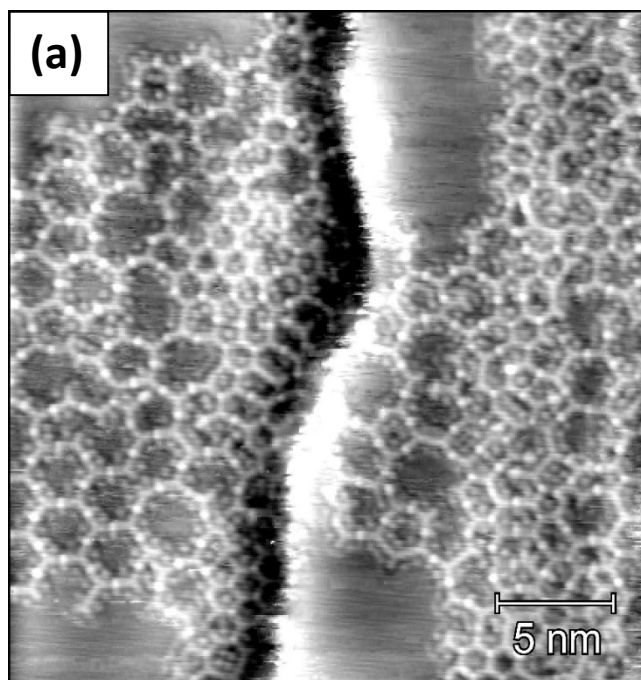


Figure 5.6. (a) A large scan of the organometallic structures of TIPT on Ag(111). (b) A zoomed in image of the organometallic structures. Silver adatoms and iodine atoms are pointed by blue and yellow dots respectively. (c) A region in which one silver adatom is coordinated to three radicals. Single iodine atom is also observed inside the pore.

different types of features in the image. One is the bright protrusions between phenyl groups of adjacent molecules. A similar observation was reported by Gutzler *et al.* [17] for the organometallic structures of 1,3,5-tris(4-bromophenyl)benzene (TBB) on Cu(111) at room temperature where the bright protrusions

between radicals are identified as metal adatoms. In our case, we identified the bright protrusions as silver atoms. These silver atoms can be coordinated with two or even three radicals (see Figure 5.6(b) and (c)). One metal adatom coordinated to three radicals is not commonly observed according to literature previously reported [17]. We think the observation of one Ag adatom coordinated to three TIPT radicals in our system is an example of this phenomenon.

Another set of features are the bright spots (sometimes observed as a halo) around the molecules. We identify these features as iodine adatoms since they appear very similar to dehalogenated adatoms seen on other metallic surfaces [17]. The same feature is also observed in situations where one metal atom is coordinated with three radical structures. In these cases the number of iodine adatoms inside the pore reduces from 6 to 1. Figure 5.6(b) is a zoomed-in image which provides more detail of the organometallic structures. A molecular model of TIPT has been overlaid to indicate a single molecule, while yellow and blue dots have been used to indicate halogen and metallic atoms respectively.

3) Annealing Experiments

The annealing experiments can be separated into two major categories: annealing below, and annealing above the temperatures required for polymerization.

Annealing below the polymerization temperature leads to a more ordered molecular network compared with room temperature deposition. Bieri *et al.* [99] reported that annealing an overlayer of metal-coordinated dimethylmethylene-bridged triphenylamine (DTPA) on Ag(111) to a temperature of 200 °C (below the polymerization point of 300 °C) leads to a more ordered metal-coordinated complex compared to room temperature deposition. We find that C–C bond formation does not occur below 125 °C. As can be seen in Figure 5.7, following an anneal at ~100 °C for 25 min, a more ordered structure characterized by the presence of almost only hexagons is observed on surface. Bright protrusions can still be clearly observed between adjacent phenyl groups in the STM image, which indicates the presence of

the silver atoms between the molecules confirming that C–C bond formation has not occurred. Taking a closer look at the bright features inside the pores, we can clearly see six bright features which is in perfect agreement with the number of halogen atoms we would expect from dehalogenation. Moreover, the center

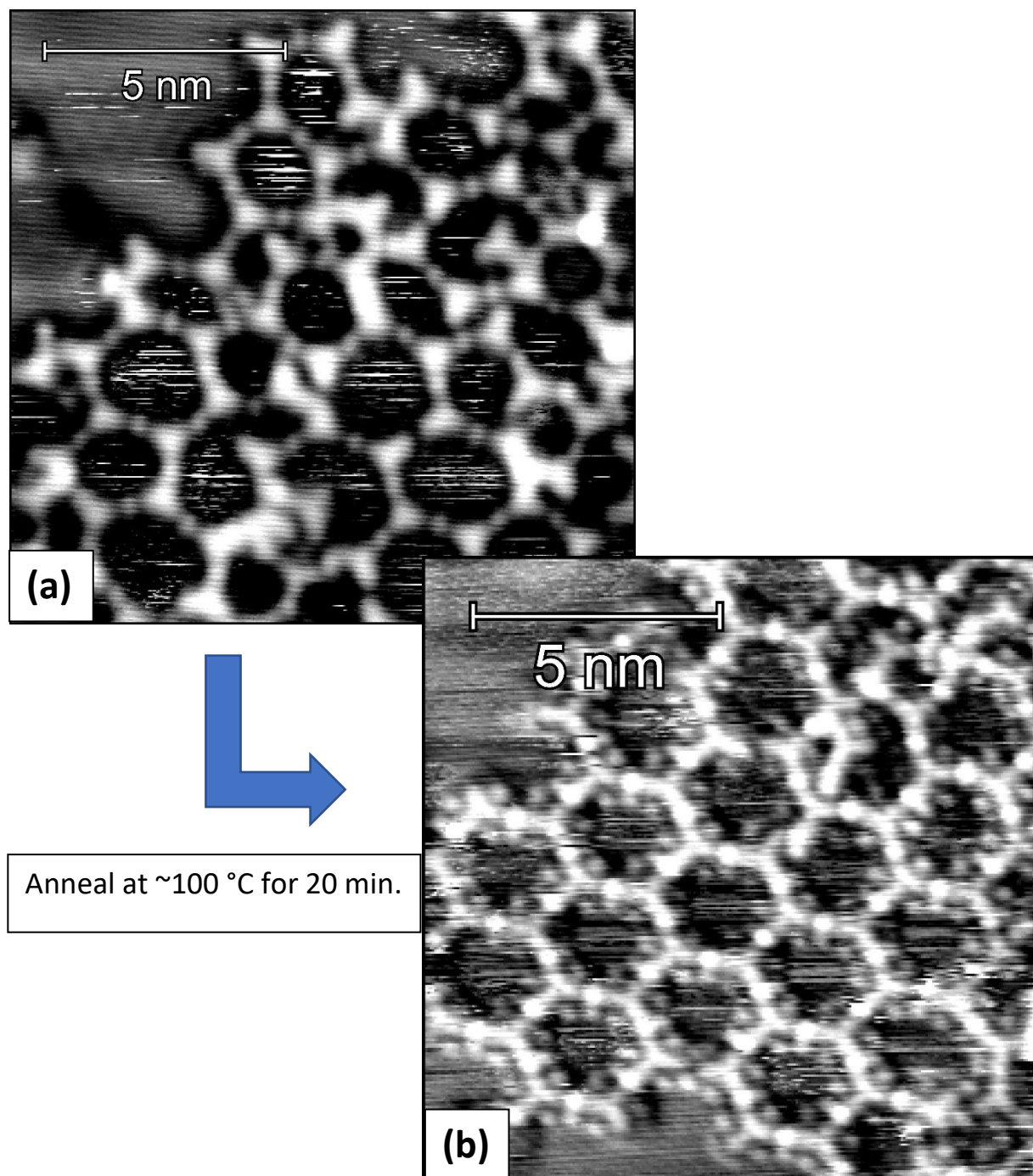


Figure 5.7. (a) Organometallic structure at RT and (b) after annealing at ~100 °C for 20 minutes. An improved order can be clearly observed.

to center distance between two adjacent triazine cores measures $1.55 \text{ nm} \pm 0.1 \text{ nm}$ which is consistent with the result of DFT calculations for the length of the spacing between nitrogen atoms in two adjacent triazines [152]. This further verified that the structure is non-covalent so far.

Further annealing at higher temperatures was carried out in order to trigger direct C–C coupling and polymerization. In our experiment, we find all proto-polymers are converted to polymers by annealing at temperatures between $125 \text{ }^\circ\text{C}$ and $160 \text{ }^\circ\text{C}$ for at least 20 mins. The degree of order is dependent on the degree of order in the preceding proto-polymer. Figure 5.8 is an STM image of a Ag(111) sample with TIPT molecules after annealing at $160 \text{ }^\circ\text{C}$ for 30 minutes. The topography of this STM image is very different from the networks obtained after annealing at $125 \text{ }^\circ\text{C}$. One obvious difference is the absence of the bright features between two molecules indicating a covalent coupling between the molecules without

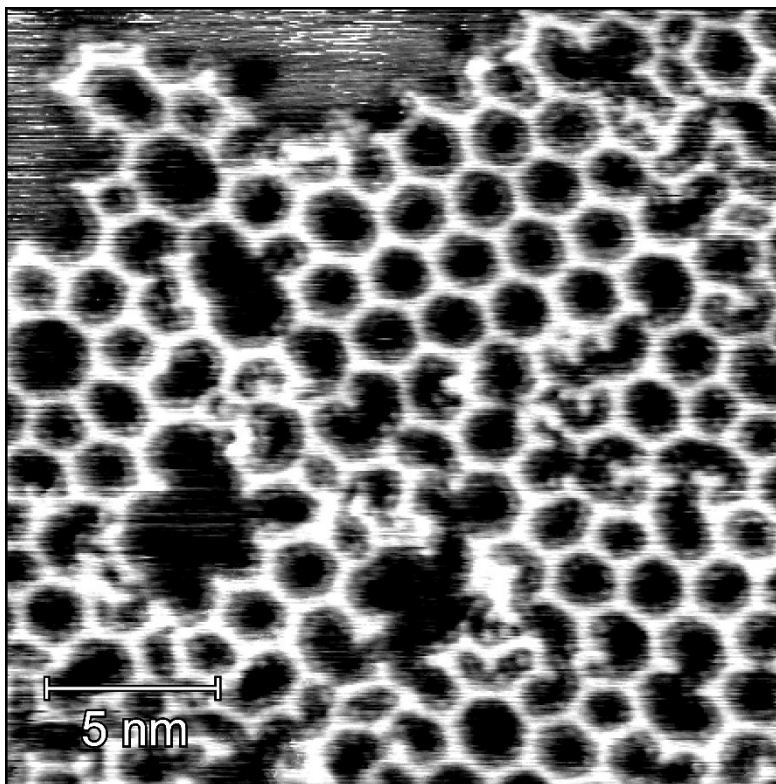


Figure 5.8. Covalent networks of TIPT on Ag(111) surface after post-deposition annealing at $135 \text{ }^\circ\text{C}$ for 30 minutes.

a silver atom. Further evidence of a transition from a proto-polymer to a 2-d polymer is the reduction in the size of both the lattice constant and the spacing between adjacent molecules.

Previously the distance between two adjacent triazine cores on a room temperature network was determined to be $1.55 \text{ nm} \pm 0.1 \text{ nm}$, and this is reduced to $1.35 \text{ nm} \pm 0.1 \text{ nm}$ after annealing. DFT calculations estimate an approximate reduction of 0.25 nm after the removal of the metal atom [152] consistent with our measurements.

A different approach to determine the change in size of molecular networks is by measuring the center-to-center distance between two interconnected molecules. As can be seen in Figure 5.9(a), the line-scan yields a distance of $2.3 \text{ nm} \pm 0.05 \text{ nm}$ between the centers of the hexagons in the room temperature molecular network. whereas the measurement in Figure 5.9(b) yields a center-to-center spacing of $2.2 \text{ nm} \pm 0.05 \text{ nm}$ which is in perfect agreement with the DFT calculations [152].

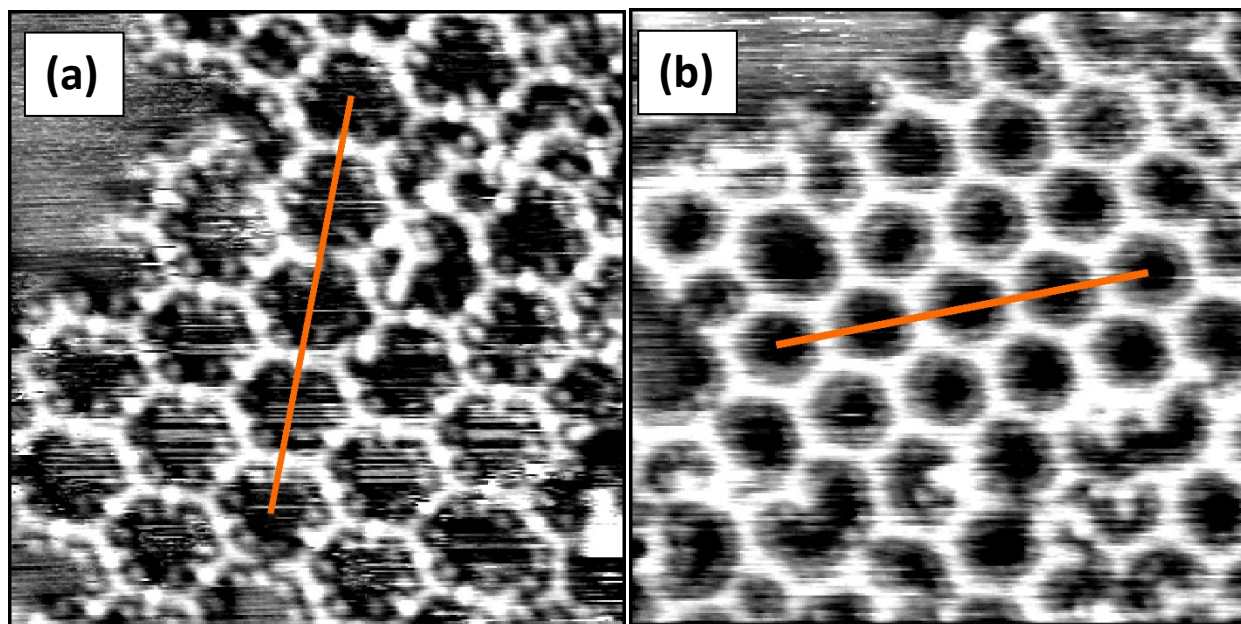


Figure 5.9. Center to center distances between TIPT hexagons for (a) organometallic structure and (b) polymer are measured using STM images

One more interesting observation from the STM data is that after polymerization the halogen atoms still remain on the surface. Figure 5.10 illustrates a high resolution STM image of the TIPT polymer. As discussed, the absence of the bright features between adjacent molecules indicates C–C bond formation, and the presence of the bright spots/halos inside the pores clearly suggests that the halogen atoms do not desorb at 135 °C. Previous studies have demonstrated that it is possible to desorb halogen from the surface following the dehalogenation of certain aryl halides by annealing at ~ 670 °C [69, 102], however it has been shown that TIPT molecules desorb before this temperature [152].

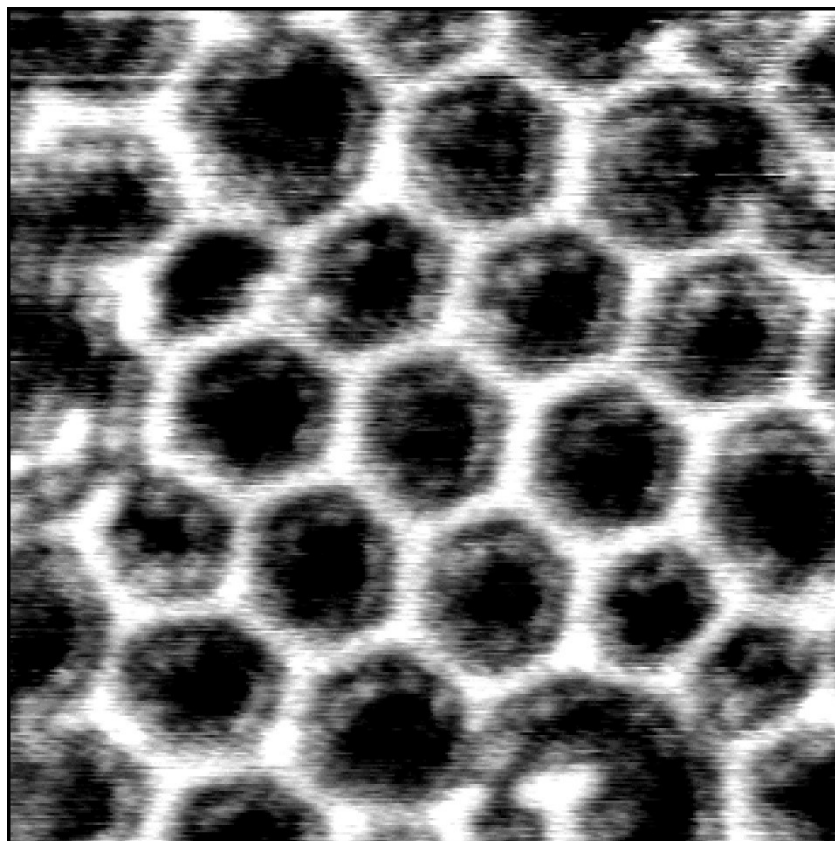


Figure 5.10. Detailed image of the TIPT polymer. Bright spots inside the pores indicate halogen atoms are still on surface.

5.3.2 Adsorption of TIPT on Si(111) $\sqrt{3}\times\sqrt{3}$ R30°-Ag

1) Molecular Adsorption with the substrate at RT

An STM image of the Si(111) $\sqrt{3}$ -Ag surface is shown in Figure 5.11. The image reveals the hexagonal $\sqrt{3}$ -Ag surface reconstruction including a number of point defects. In Chapter 4, we have demonstrated that the Si(111) $\sqrt{3}$ -Ag surface provides an inert, high-mobility template for the adsorption of halogenated organic molecules [27].

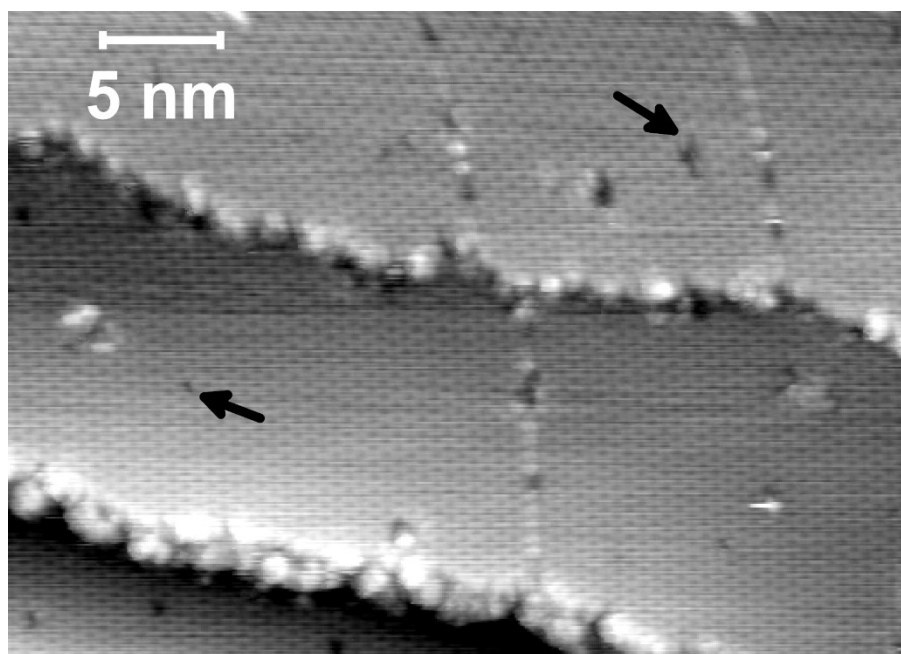


Figure 5.11. STM image of the $\sqrt{3} \times \sqrt{3}$ -Ag surface. ($V_{\text{sample}} = -0.9$ V, $I = 300$ pA). The image includes three $\sqrt{3}$ terraces separated by single height atomic steps. The terraces include a number of point defects (examples indicated by arrows) in the $\sqrt{3}$ reconstruction.

At low coverage our data also indicates that TIPT monomers are also quite mobile on the Si(111) $\sqrt{3}$ -Ag surface at room temperature. Like TBTTA, as we increase the molecular coverage of TIPT, we observe that many of the STM images exhibit horizontal streaks in the fast scan direction (Figure 5.12).

This apparent ‘noise’ is attributed to diffusing species which remain trapped below the tip along the fast scan direction. As discussed in the context of TBTTA adsorption, this phenomenon is not uncommon when imaging weakly bound molecular adsorbates at room temperature [149]. In the case of TIPT, rather

than being randomly dispersed about the $\sqrt{3}$ -Ag terraces, we observe that the streaks tend to form “fuzzy lines” and furthermore, these lines are often regularly spaced with a period on the order of 4 nm. The lines would appear to indicate that there are regions on the surface where the diffusing species spend relatively more time. On further inspection, we observe that many of the lines pass through point defects on the $\sqrt{3}$ reconstruction and suggests that while the point defects are not sufficient to pin the diffusing species, they can lead to an increased residence time for monomers in the vicinity.

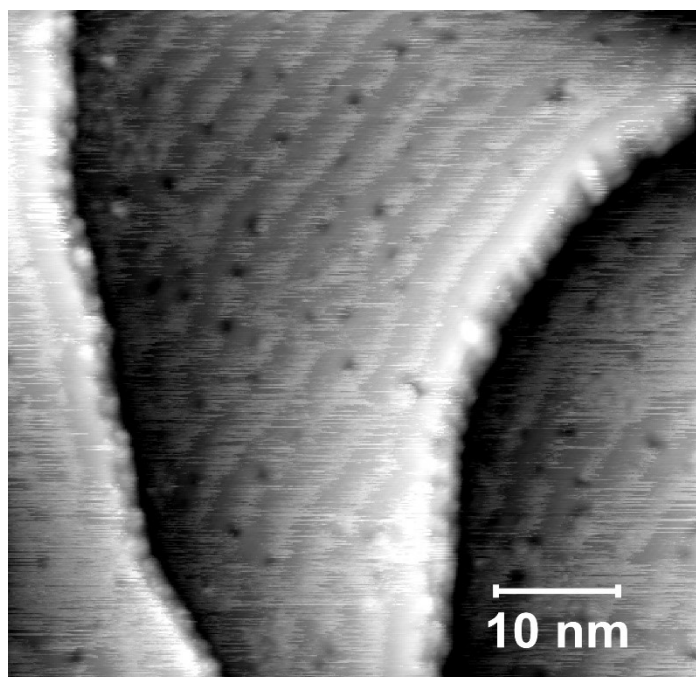


Figure 5.12. An STM image of TIPT on the $\sqrt{3}$ -Ag surface at low coverage. ($V_{\text{sample}} = -1.22$ V, $I = 490$ pA). The image indicates three terraces separated by atomic steps. Dark spots are point defects in the $\sqrt{3}$ -Ag reconstruction and the “Fuzzy lines” indicate diffusing species on the surface.

With a further increase in TIPT exposure, the STM images reveal the formation of ordered domains (Figure 5.13). The ordered TIPT domains are characterized by a parallel row structure. On closer inspection, the parallel rows are actually “zig-zagged” and the domains are defined by a rectangular unit cell containing two bright features per cell (Figure 5.14). The rectangular cell is characterized by a long side of 2.07 ± 0.05 nm, a short side of 1.83 ± 0.05 nm, and an angle of 90 ± 5 degrees. In addition, the zig-zag rows are rotated from the threefold high symmetry directions of the underlying $\sqrt{3}$ reconstruction by

approximately 13 degrees. Interestingly, at this stage, we find the fuzzy lines still exist on the surface, and they also seem to follow the threefold high symmetry directions of the substrate (see Figure 5.13). Unfortunately, due to the still diffusing molecules, we are not able to obtain the resolution we need to determine the exact rotational relationship between those fuzzy lines and $\sqrt{3}$ -Ag lattice, but we suspect that the three-fold arrangement of the fuzzy lines is driven by the weak interaction with the underlying $\sqrt{3}$ substrate.

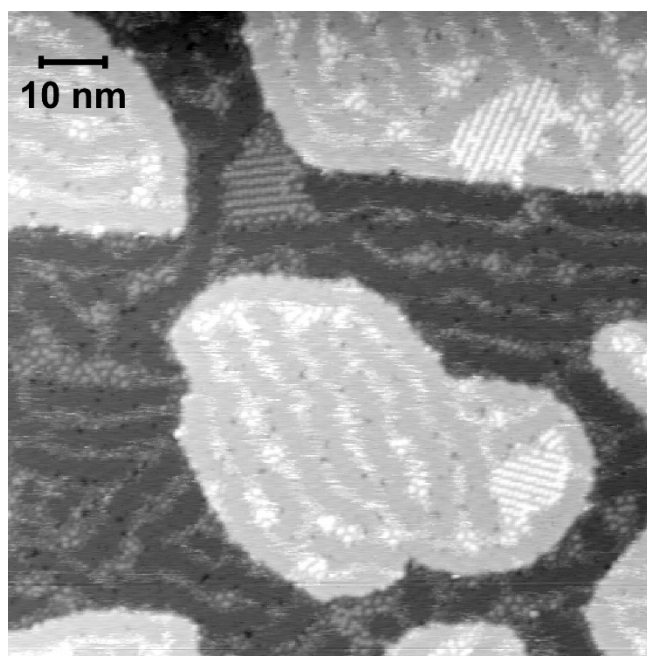


Figure 5.13. STM image of the $\sqrt{3}$ -Ag surface with higher molecular coverage. ($V_{\text{sample}} = -1.42$ V, $I = 500$ pA). In addition to “fuzzy lines” several supramolecular domains are evident.

Gatti *et al.* investigated the adsorption of TIPT molecules at the trichlorobenzene (TCB)-HOPG interface. They found that TIPT forms a SAMN defined by a unit cell of 2.04 ± 0.09 nm, by 1.54 ± 0.09 nm, and an angle of $90^\circ \pm 5^\circ$. To gain further insight into the layer these authors also performed DFT calculations on a free standing 2-d TIPT layer. They found an energy minimized structure characterized by a rectangular two monomer cell held together by $I \cdots H$ hydrogen-bond like contacts with dimensions of 2.41 nm, by 1.38 nm and an angle of 91 degrees.

The unit cell we observe on the Si(111) $\sqrt{3}$ -Ag surface is similar in geometry to both the experimental cell observed on HOPG and the DFT optimized cell [118]. The long dimension agrees within error i.e. 2.07 ± 0.05 nm on the Si(111) $\sqrt{3}$ -Ag versus 2.04 ± 0.09 nm on HOPG, however the short side we observe is significantly expanded, 1.83 ± 0.05 nm versus 1.54 ± 0.09 nm. The mobility of the monomers at low coverage is strong indication that the domains we observe on the Si(111) $\sqrt{3}$ -Ag surface are domains of intact TIPT monomers. We believe the difference in the short dimension of our unit cell is due to the presence of the Si(111) $\sqrt{3}$ -Ag substrate. Thus, DFT calculations are performed to investigate the origin of this difference which will be discussed later.

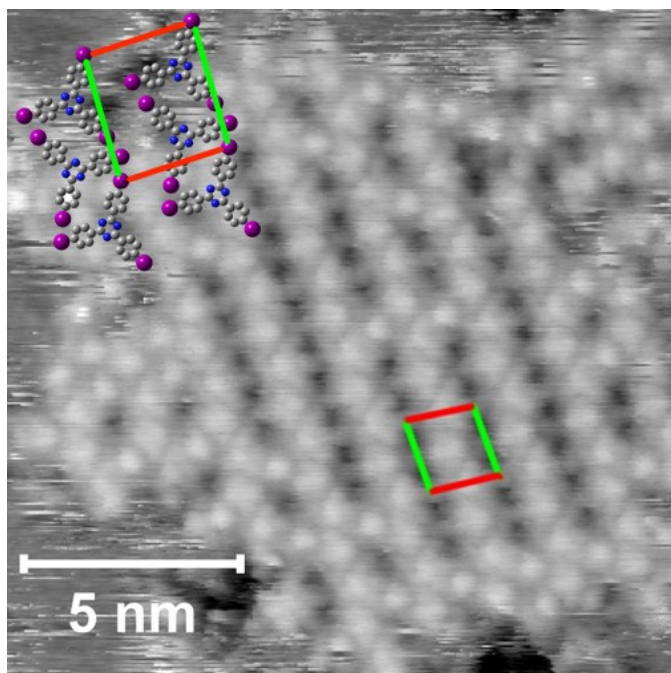


Figure 5.14. STM image of a TIPT supramolecular domain on the $\sqrt{3}$ -Ag surface ($V_{\text{sample}} = -1.30$ V, $I = 300$ pA). The unit cell is highlighted and a proposed two monomer per cell is proposed (see insert).

The fact that the TIPT monomers remain intact on the Si(111) $\sqrt{3}$ -Ag surface rather than de-iodinate is rather surprising. The de-iodination of alkyl-halides on Ag single crystal metal surfaces is known to take place spontaneously at room temperature [97, 154-156]. Indeed, as just presented in Section 5.3.1, TIPT de-iodinates at room temperature on Ag(111) and on Cu(111) [152]. In other words, it appears that

the monolayer of silver atoms at the Si(111) $\sqrt{3}$ -Ag surface is initially less reactive to aryl-halides than the metal. We observed similar behavior with TBTTA which de-brominates readily on Ag(111) [19], however we found no evidence of any significant de-halogenation on the Si(111) $\sqrt{3}$ -Ag surface at room temperature [27].

As the coverage is increased we observe that the extent of the supramolecular domains is often limited by defects in the Si(111) $\sqrt{3}$ -Ag surface. Domains often terminate or have voids where they encounter point defects or domain boundaries in the underlying $\sqrt{3}$ -Ag layer (Figure 5.15). In fact, when the initial density of point defects in the Si(111) $\sqrt{3}$ -Ag exceeds approximately $5 \times 10^{16} \text{ m}^{-2}$ prior to molecular deposition, no ordered domains are observed. The defect density in the $\sqrt{3}$ reconstruction is extremely sensitive to the annealing temperature following Ag deposition. Annealing temperatures above 580 °C leads to higher defect densities. The exact nature of this temperature dependence is currently under study.

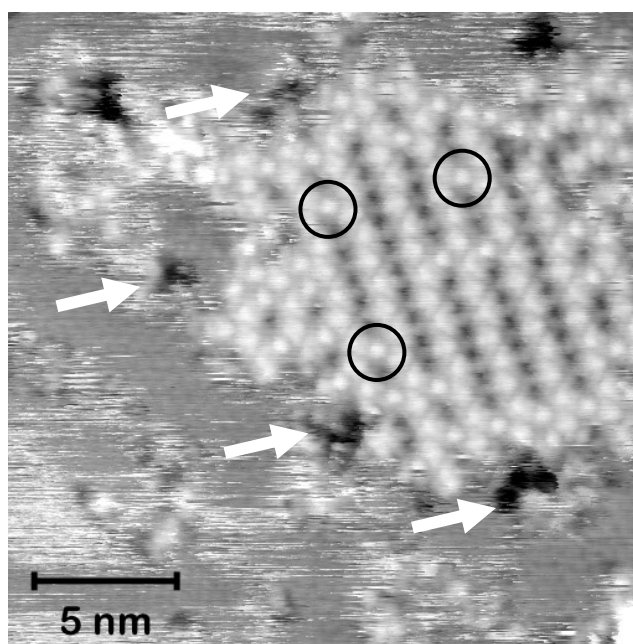


Figure 5.15. STM image of a supramolecular TIPT domain ($V_{\text{sample}} = -1.42 \text{ V}$, $I = 490 \text{ pA}$). The domain contains extra spots between the rows (circles). The extent of the domain appears limited by defects in the $\sqrt{3}$ reconstruction (white arrows).

On closer inspection, the supramolecular domains also exhibit extra, or “*interstitial*” bright spots located between the zig-zag rows (indicated by black circles in Figure 5.15). These interstitial defects are not observed on the HOPG surface, however the spacing between the rows on the Si(111) $\sqrt{3}$ -Ag surface is considerably larger (1.8 nm versus 1.5 nm). We do not believe that the additional space is sufficient to accommodate an additional TIPT molecule, and that it is more likely to be either a silver or iodine adatom. While the mobility of the molecules at low coverage and the formation of ordered supramolecular domains suggests that the majority of TIPT monomers are intact, some TIPT molecules may de-halogenate and the interstitial features we observe may be the resultant iodine atoms. Evidence for a small amount of room temperature dehalogenation will be presented later on in this chapter.

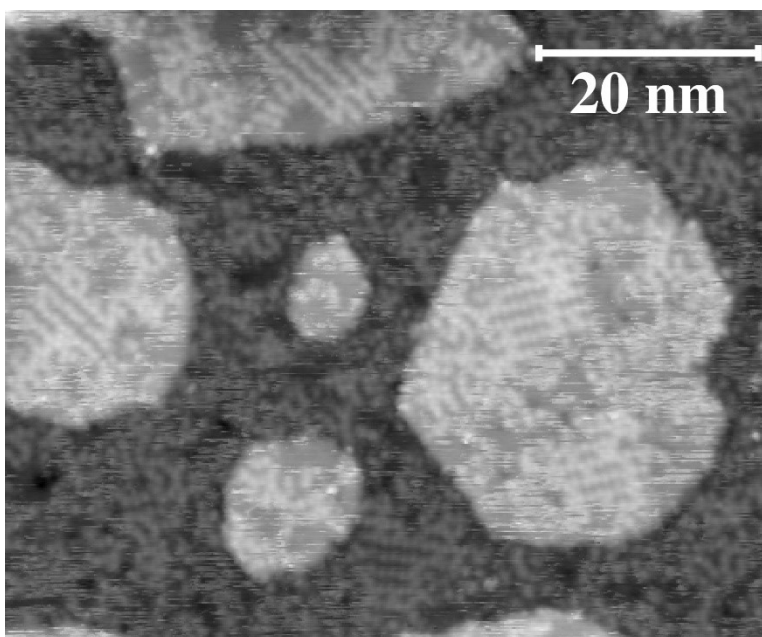


Figure 5.16. STM image revealing several one atomic layer high $\sqrt{3}$ -Ag islands dispersed on a $\sqrt{3}$ -Ag terrace ($V_{\text{sample}} = -1.5\text{V}$, $I_t = 0.5\text{ nA}$). On both the islands and the terraces the supramolecular domains are observed separated by disordered regions.

Increasing the TIPT coverage further (Figure 5.16), results in a surface which is a mix of supramolecular domains separated by disordered regions. Figure 5.16 shows evidence of diffusing molecules (fuzzy lines), however most of the molecules are stationary. It appears the additional coverage

acts to restrict diffusion and “freeze” the molecules in place. Although the number of ordered domains does increase with coverage, the size of each domain rarely exceeds the typical sizes observed at lower coverage. We believe this is due to the fact that point defects in the Si(111) $\sqrt{3}$ -Ag reconstruction ultimately restrict the extent of the domains.

2) DFT results and discussion

As mentioned in the previous section, the unit cell we observe on the Si(111) $\sqrt{3}$ -Ag surface is similar in geometry to both the experimental cell observed on HOPG, and the DFT optimized cell. The long dimension agrees within error (2.07 ± 0.05 nm on the Si(111) $\sqrt{3}$ -Ag versus 2.04 ± 0.09 nm on HOPG), but the short side we observe is significantly expanded (1.83 ± 0.05 nm versus 1.54 ± 0.09 nm). The mobility of the monomers at low coverage is a strong indication that the domains we observe on the Si(111) $\sqrt{3}$ -Ag surface are supramolecular domains of intact TIPT monomers. We suspect the difference in the short dimension of our unit cell is due to the presence of the Si(111) $\sqrt{3}$ -Ag substrate and our hypothesis is that the observed cell is a commensurate overlayer.

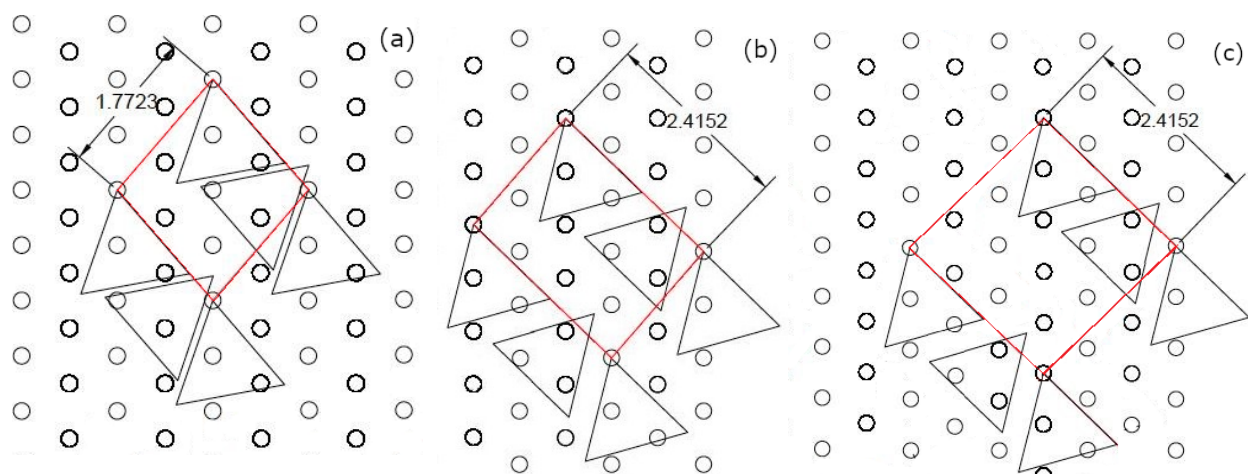


Figure 5.17. Three possible commensurate configurations with dimensions (a) 1.7723 nm \times 1.7723 nm, (b) 2.4152 nm \times 1.7723 nm and (c) 2.4152 nm \times 2.4152 nm. Dots represent the $\sqrt{3}$ lattice points.

Based on this hypothesis, three commensurate configurations are examined using a six-monomer supramolecular model (see Figure 5.17). Figure 5.17(a) represents a cell commensurate with the $\sqrt{3}$ lattice and expressing the commensurate cell in matrix form yields:

$$\begin{pmatrix} a_m \\ b_m \end{pmatrix} = \begin{pmatrix} 2 & 1 \\ -2 & 3 \end{pmatrix} \begin{pmatrix} a_{\sqrt{3}} \\ b_{\sqrt{3}} \end{pmatrix}$$

Figure 5.17(b) represents the commensurate cell closest to our observed cell. The dimensions of this cell agree within error compared to observed cell, which can be expressed in matrix form:

$$\begin{pmatrix} a_m \\ b_m \end{pmatrix} = \begin{pmatrix} 2 & 1 \\ -3 & 4 \end{pmatrix} \begin{pmatrix} a_{\sqrt{3}} \\ b_{\sqrt{3}} \end{pmatrix}$$

The last cell shown in Figure 5.17(c) corresponds to a possible commensurate cell larger than our observed cell, and expressed in matrix form yields:

$$\begin{pmatrix} a_m \\ b_m \end{pmatrix} = \begin{pmatrix} 3 & 1 \\ -3 & 4 \end{pmatrix} \begin{pmatrix} a_{\sqrt{3}} \\ b_{\sqrt{3}} \end{pmatrix}$$

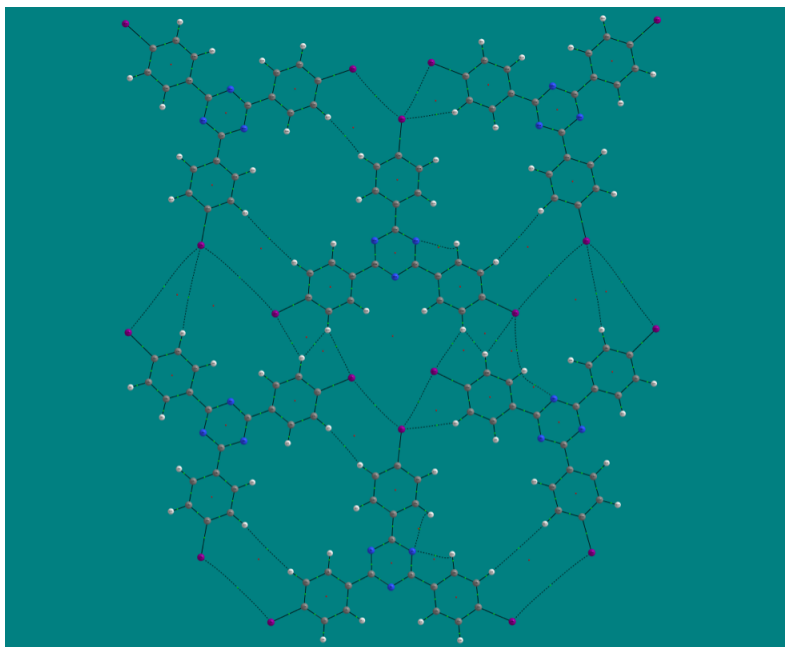


Figure 5. 18. A molecular graph showing all bonding interactions for the 1.77 nm \times 1.77 nm cell.

Based on these three possible commensurate configurations, we performed DFT calculations. Results and discussions are presented as follows. For the $1.7723 \text{ nm} \times 1.7723 \text{ nm}$ cell, the result of the QTAIM calculations indicates that all interactions between the molecules are non-covalent. The molecular structure is mainly driven by the $\text{I} \cdots \text{I} \cdots \text{H}$ triangular binding motifs formed by halogen type bonds ($\text{I} \cdots \text{I}$) and hydrogen type bonds ($\text{H} \cdots \text{I}$). Another hydrogen type bonding ($\text{H} \cdots \text{H}$) is also observed in this cell which can be attributed to the tight intermolecular spacing (Figure 5.18). Geometrically, due to the compact intra-row and inter-row spacing, we see obvious signs of molecular interpenetration which is not consistent with our experimental observations. In addition, this configuration is the least stable and has a large core-core repulsion energy. Thus, we consider the $1.77 \text{ nm} \times 1.77 \text{ nm}$ cell to be a poor representation of our observed cell.

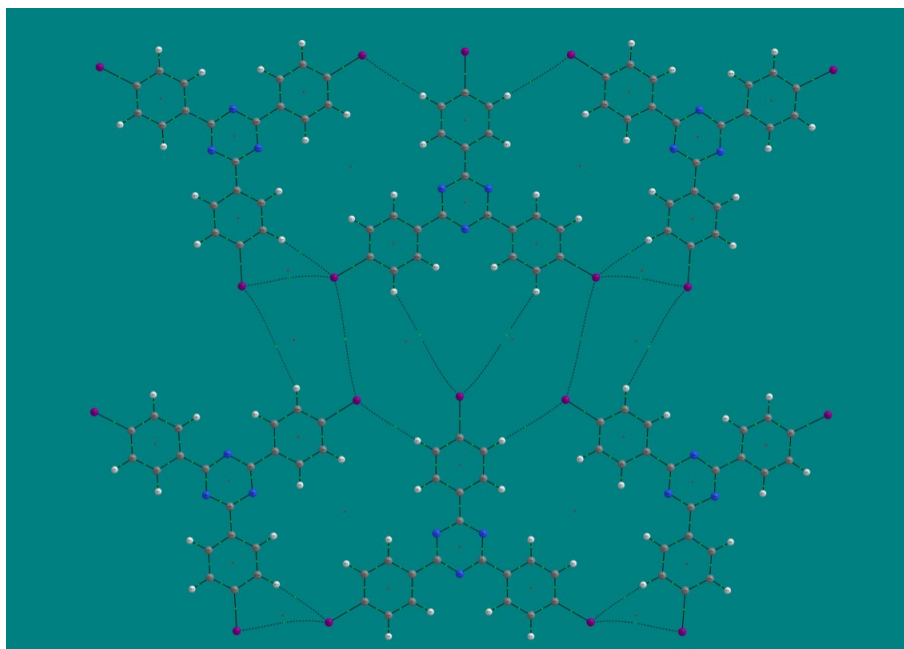


Figure 5.19. A molecular graphing showing all bonding interactions for a $2.42 \text{ nm} \times 1.77 \text{ nm}$ cell.

For the second commensurate configuration, we define a cell with a dimension of $2.42 \text{ nm} \times 1.77 \text{ nm}$. This cell is closest to our observed cell both in dimension and geometry. Similar to the $1.77 \text{ nm} \times 1.77 \text{ nm}$ cell, QTAIM results indicate that the cell is held together primarily by $\text{I} \cdots \text{I}$, $\text{H} \cdots \text{I}$ and

H \cdots H interactions (Figure 5.19). However, the geometry changes considerably compared with the 1.77 nm \times 1.77 nm cell. We find the rows are well defined and the inter-row interactions are very weak. We find the structure has a low relative energy and a lower core-core repulsion energy. It is evident that this configuration is much more stable compared with the 1.77 nm \times 1.77 nm cell and the geometry of the resultant cell is also consistent to our observed cell.

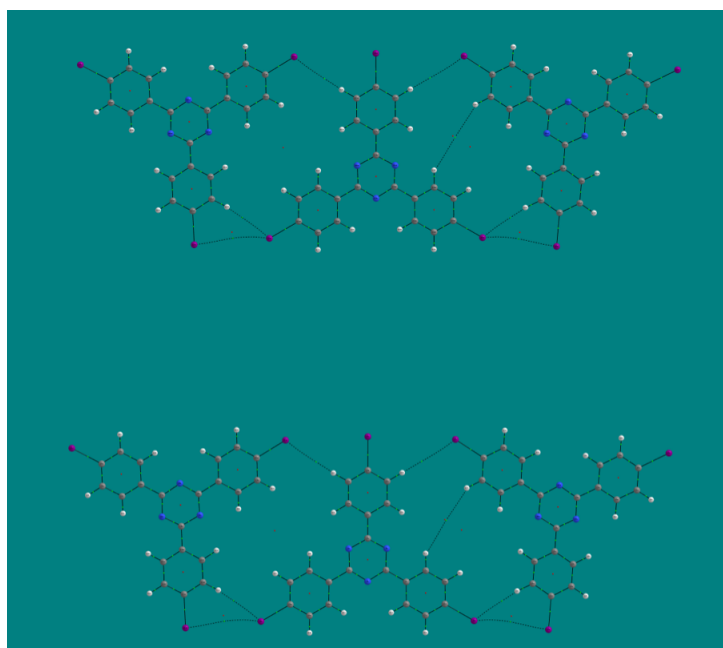


Figure 5. 20. A molecular graphing showing all bonding interactions for a 2.42 nm \times 2.42 nm cell.

In the last commensurate configuration we considered, we expanded the inter-row spacing even more to make a cell with dimensions of 2.42 nm \times 2.42 nm (Figure 5.20). Understandably, due to the larger spacing, we find no appreciable inter-row bonding interactions. However, the structure along the row is still well defined and exhibits the same bonding interactions. The relative energy change and repulsion energy indicates that this structure is the most stable configuration among the three, but is only slightly more stable than the 2.42 nm \times 1.77 nm cell. We can attribute relative stability to a lower nuclear repulsion due the larger inter-row spacing. The annihilation of inter-row interactions and a well-defined geometry along the row reveals that the row structure can be stabilized solely via intra-row interactions.

Table 5.1 PBE1PBE/LANL2DZ relative energy of each configuration and associated nuclear-nuclear repulsion energy (E_{NN}).

	1.77nm×1.77nm	2.42nm×1.77nm	2.42nm×2.42nm
ΔE (kcal·mol⁻¹)	18.2	0.2	0
E_{NN} (Hartree)	27725.0658	26683.9325	24956.9925

Table 5.1 shows the relative computed energies and the nuclear-nuclear repulsion energies for the three possible commensurate configurations. When we compare the two configurations with well defined row structures (both cells with 2.42 nm intra-row spacing), the change in the inter-row spacing from 1.77 nm to 2.42 nm leads only to a 0.2 kcal·mol⁻¹ difference in ΔE and reveals a very flat potential energy curve between the two spacings thus a very weak inter-row interaction. Moreover, considering the fact that the molecular structures are formed at room temperature, we can convert 0.2 kcal·mol⁻¹ to 71.35% Boltzmann population ratio at 298 K. Thus, we find the Boltzmann average inter-row spacing to be 1.956 nm which is very close to experimental observed value (1.83 nm).

To sum up, the results from the DFT calculations suggest that intra-row interactions are the major force in determining the structure of the cell while inter-row interactions are minor. Combining this with our experimental observations, clearly the expansion in the inter-row spacing is a result of the commensurate driving force of the substrate. From previous experiment discussed in Chapter 4, we learned that the Si(111) $\sqrt{3}$ -Ag substrate can have a non-negligible effect on the arrangement of the overlayer molecular structures. Due to the relative strong intra-row interactions, the arrangement of the row structures is similar to the overlayers observed on both the HOPG, and Au surfaces [152]. However, the inter-row interactions are very weak (confirmed by a flat potential energy curve between the two larger cells), allowing the inter-row spacing to expand and adapt to a commensurate conformation with the Si(111) $\sqrt{3}$ -Ag substrate.

In conclusion, DFT calculations validate our hypothesis that the expansion in the inter-row spacing of the observed unit cell is due the periodicity of the underlying $\sqrt{3}$ -Ag substrate.

3) Annealing Experiments

Since most TIPT molecules remain intact on Si(111) $\sqrt{3}$ -Ag surface at RT, we attempted to activate a dehalogenation reaction by annealing the samples. In our annealing experiments, TIPT molecules are deposited onto a Si(111) $\sqrt{3}$ -Ag surface kept at room temperature. Following deposition, then samples are heated to elevated temperatures as desired. Unfortunately, even a gentle anneal to ~ 125 °C for 120 mins leads to a disordered surface. As evident in Figure 5.21, only a very small portion of the ordered structures survives after annealing (white arrows in Figure 5.21). In general, we found it extremely hard to obtain useful information using STM after annealing. It indicates that while annealing the samples may activate dehalogenation, the liberated iodine atoms interact with and break apart the underlying $\sqrt{3}$ -Ag layer. The

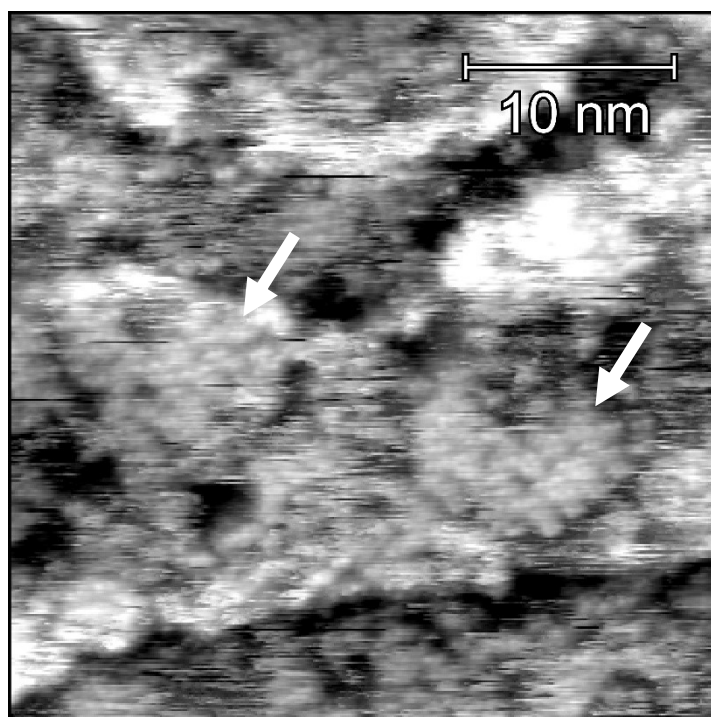


Figure 5.21. A STM image of the surface after annealing at ~ 100 °C. Only very small portion of ordered structures survived pointed out by white arrows.

degradation in Si(111) $\sqrt{3}$ -Ag substrate results in a surface with high defect density and a highly disordered surface.

4) Effect of Deposition on Si(111) $\sqrt{3}\times\sqrt{3}$ R30°-Ag Substrate

In order to clarify how the deposition of molecules, and post-deposition annealing affects the substrate, we compared STM images obtained from the same surface at different stages. Figure 5.22(a) displays a bare Si(111) $\sqrt{3}$ -Ag prior to molecular deposition. We can see large well defined Si(111) $\sqrt{3}$ -Ag terraces with relatively few point defects. Figure 5.22(b) is the same surface after molecular deposition at room temperature. At this point, although some large TIPT supramolecular domains are observed, there is also an increase in the number of point defects in the $\sqrt{3}$ -Ag layer. We attribute this increase to a limited number of molecules that dehalogenate upon deposition. We believe the liberated iodine atoms subsequently interact destructively with the substrate. In fact after annealing, as shown in Figure 5.22(c), we observed no ordered domains and a highly defective surface is produced. Another noticeable change in the STM images is the absence of the horizontal streaks and the $\sqrt{3}$ -Ag layer is better resolved after annealing. This is due to the further dehalogenation of the molecules observed to diffuse on a RT surface. The dehalogenated molecules react strongly with the substrate thus and are no longer mobile.

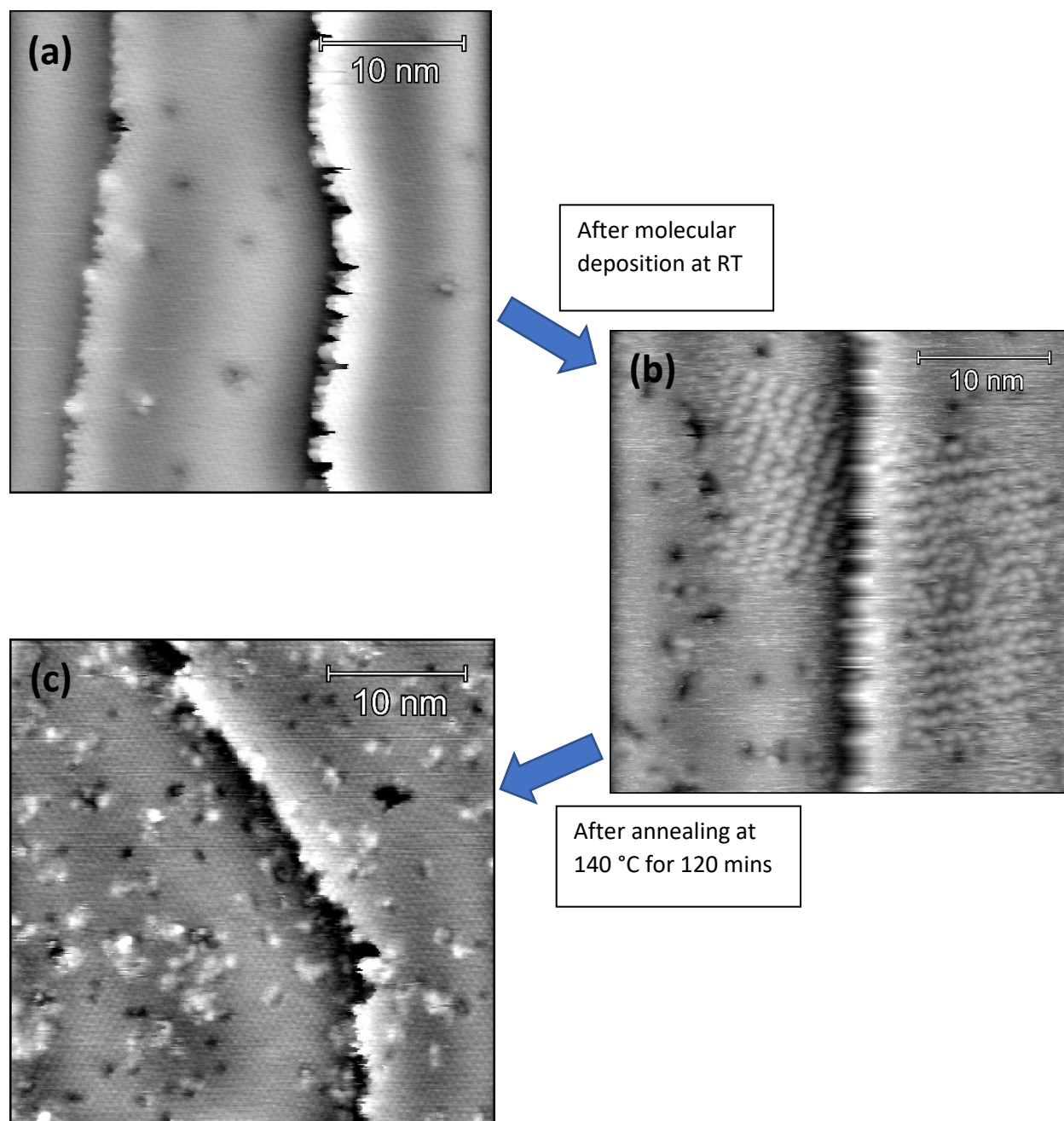


Figure 5.22. Three STM images taken from same sample with conditions (a) bare $\sqrt{3}$ -Ag/Si(111), (b) after molecular deposition at RT and (c) after post-deposition annealing at 140 °C.

5.4 Summary

In this chapter, the interaction between the halogenated molecule, TIPT with both the Ag(111) and Si(111) $\sqrt{3}$ -Ag surfaces have been studied using room temperature STM. On the Ag(111) surface, TIPT molecules dehalogenate spontaneously upon deposition at room temperature and form organometallic

structures with two (and sometimes three) molecules binding to one silver atom. This proto-polymer forms pentagonal, hexagonal, heptagonal, and other polygonal motifs with a low degree of order. Our data indicates that the Iodine atoms still remain on the surface following dehalogenation and often show up as bright spots/halos inside the polygonal motifs. Gentle annealing at ~ 100 °C leads to a more ordered molecular network characterized almost exclusively by hexagons.

Further annealing at ~ 135 °C leads to covalent C–C bond formation and polymerization. Polymerization is confirmed by the absence of bright features between adjacent molecules. Moreover, the reduced size of both the lattice constant (from $2.35 \text{ nm} \pm 0.05 \text{ nm}$ to $2.25 \text{ nm} \pm 0.05 \text{ nm}$) and the spacing between adjacent molecules ($1.55 \text{ nm} \pm 0.1 \text{ nm}$ to $1.35 \text{ nm} \pm 0.1 \text{ nm}$) is another important indication of the transition from proto-polymer to a 2-d polymer.

We also studied the deposition of TIPT molecules onto the Si(111) $\sqrt{3}$ -Ag surface. In contrast to Ag(111), we find that the Si(111) $\sqrt{3}$ -Ag surface provides an inert, high-mobility template for TIPT adsorption at room temperature. TIPT monomers remain largely intact and readily diffuse to step edges and defects in the $\sqrt{3}$ -Ag overlayer. At low coverage, most images display regularly spaced “fuzzy lines” which indicate molecular diffusion at room temperature. At higher coverage, supramolecular domains are formed and defined by a two-monomer rectangular unit cell of $2.07 \pm 0.05 \text{ nm}$ by $1.83 \pm 0.0 \text{ nm}$. The geometry of the cell is similar to an energy optimized structure of a 2-d free-standing TIPT layer determined by DFT. The long side of our cell is almost identical to free standing cell while the short side differs considerably. The similarities in geometry support the idea that de-halogenation does not occur on the Si(111) $\sqrt{3}$ -Ag surface at room temperature and that the supramolecular domains are characterized by intact monomers held together by $\text{I} \cdots \text{H}$ hydrogen-like bonding.

The formation of supramolecular domains on the silicon surface is very sensitive to the quality of the $\sqrt{3}$ reconstruction. The domain size is often limited by point defects in the underlying $\sqrt{3}$ reconstruction,

in fact no ordered structures are observed on surfaces with defect densities in excess of $5 \times 10^{16} \text{ m}^{-2}$. With increasing coverage, the surface consists of ordered supramolecular domains separated by regions of disorder. While the number of domains increases with coverage, the size of domains remains limited by defects in the Si(111) $\sqrt{3}$ -Ag reconstruction.

Annealing sample does not lead to a more ordered network. On the contrary, even after gentle annealing at 100 °C the surface shows obvious sign of degradation. Only a very small portion of the ordered structures survive with most of the surface being disordered. Further annealing at 140 °C leads to a more defective surface with no ordered structures. We believe that an increasing number of molecules dehalogenate and the liberated iodine atoms interact destructively with the substrate, leading to a highly defective surface.

The contrasting behaviour on the Si(111) $\sqrt{3}$ -Ag and Ag(111) surfaces is striking. We believe this contrast may be due to the absence of silver adatoms on Si(111) $\sqrt{3}$ -Ag. The dehalogenation process requires the insertion of a silver atom in-between the molecular species (organometallic intermediate). This metal atom can either be an adatom on the surface or an atom from the outermost layer. On Ag(111), at or above room temperature, there are plenty of adatoms on the surface that can participate in dehalogenation. In contrast, the only silver atoms available on the Si(111) $\sqrt{3}$ -Ag surface are the Ag trimers which are an integral part of the reconstruction. As a result, in order to undergo dehalogenation, silver atoms in the $\sqrt{3}$ -Ag reconstruction must be lifted leading to a break up of the surface.

Chapter 6

**Adsorption of TBTANG on
Si(111) $\sqrt{3}\times\sqrt{3}R30^\circ$ -Ag and Au(111)**

6.1 Introduction

In this chapter, we investigate the adsorption of a halogenated molecule with threefold symmetry, 2,6,10-tribromo-4,8,12-trioxa-3a²-azadibenzo[cd,mn]pyrene (TBTANG, see Figure 6.1) onto the Au(111) and Si(111) $\sqrt{3}$ -Ag surfaces.

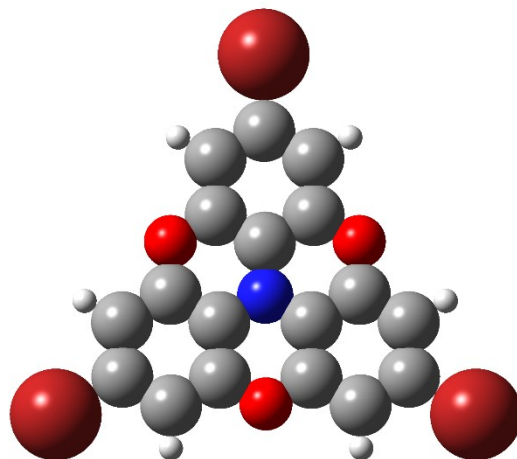


Figure 6.1. The molecular structure of TBTANG. Bromine atoms are indicated in brown red, carbon atoms in grey, nitrogen atoms in blue, oxygen atoms in candy red and hydrogen atoms in white.

For the adsorption of TBTANG on Au(111) surface, we reproduce the unpublished self-assembly results reported by F. DeMarchi and G. Galeotti *et al.* [157] on a room temperature sample. Their results indicate that deposition of TBTANG onto the Au(111) surface, held at room temperature, yields extended domains of a SAMN consisting of intact TBTANG molecules, which follow the herringbone reconstruction of the substrate. We are also able to reproduce their one-step polymerization experiment which results in a complete TBTANG polymer with high degree of order on Au(111) surface [158].

As discussed in the previous two chapters, we have demonstrated that the Si(111) $\sqrt{3}$ -Ag surface can provide a relatively inert template with sufficient mobility for the diffusion of halogenated molecules. Given this knowledge, our primary focus with TBTANG is to investigate the adsorption on the Si(111)

$\sqrt{3}$ -Ag surface and compare the results with those on the Au(111) surface in order to understand both the similarities, and differences between these two very different substrates.

In this work, we explore the interaction of an oxygen-bridged tribromo-substituted triphenylamine molecule, TBTANG, with both the Si(111) $\sqrt{3}$ -Ag and Au(111) surfaces using STM. The TBTANG molecules are thermally sublimed onto the two substrates under UHV conditions. The results demonstrate the important role of the substrate in the molecular patterning of the resultant SAMN. One of the primary reasons we chose to work with TBTANG is that, compared with other triphenylamine systems, the oxygen bridging helps planarize the molecule and leads to improved self-assembly [157]. Moreover, TBTANG contains heteroatoms, i.e. three oxygen and one nitrogen atom. This is particularly attractive since heteroatoms within the supramolecular layer allow for a high level of tunability. Using molecular layers which incorporate different functional groups and heteroatoms into the matrix will be an interesting topic in the field of surface science.

6.2 Experiment

All experiments are performed in a single UHV system discussed previously. Detailed information on the Si(111) $\sqrt{3}$ -Ag sample preparation, techniques used for surface quality assessment, and STM scanning can be found in Section 4.2. The Au sample is cleaned by sputter-anneal cycles very similar to the Ag preparation procedure discussed in Section 5.2. The major difference is that the annealing temperature of the gold is 270 °C, which is lower than the value for silver (330 °C).

TBTANG deposition

To deposit the TBTANG monomers onto the Si(111) $\sqrt{3}$ -Ag and Au(111) surfaces, the molecules are sublimed *in-situ* from a boron-nitride crucible onto the samples. Molecular deposition is confirmed using AES. AES of the $\sqrt{3}$ -Ag surface after TBTANG deposition clearly reveals a carbon KLL transition at

272 eV which indicates successful molecular deposition (see Figure 6.2). As was the case with TBTTA and TIPT, the carbon transition is partially masked by a silver MNN transition at 351 eV. The other two elements which in principle could be tracked are bromine and oxygen. Unfortunately, the bromine LMM transition (at 1393 eV) was not tracked due to the low signal strength. The oxygen KLL transition (at 508 eV) is stronger than bromine but with a broad profile. Thus, in this experiment the change in amplitude of oxygen peak with respect to the silicon LMM transition at 96 eV is used as a crude indicator of molecular coverage. A small nitrogen Auger transition at 389 eV is also observed, however this peak was not tracked due to the low signal strength.

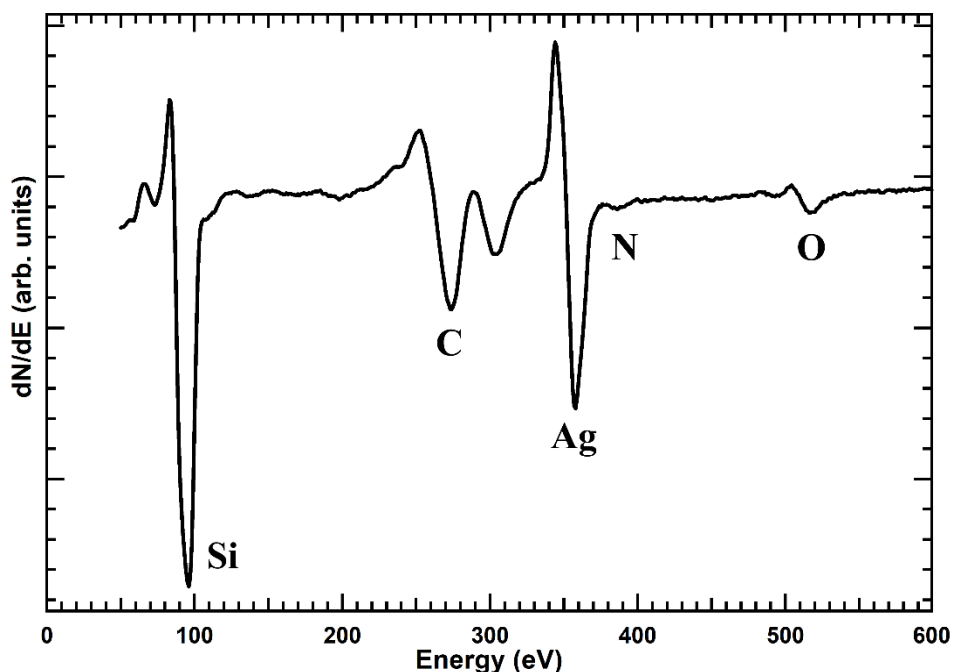


Figure 6.2. An Auger spectrum of a TBTANG covered Si(111) $\sqrt{3} \times \sqrt{3}$ -Ag surface. The size of the MNN transition at 519 eV relative to the silicon transition at 96 eV was used as an estimate of the molecular coverage.

On the Au(111) surface, the carbon KLL transition at 272 eV is partially masked once again by one of the gold transitions (NNV at 252 eV), therefore we used the change in amplitude of oxygen peak with respect to the gold OVV transition at 69 eV as an estimate of molecular coverage (see Figure 6.3).

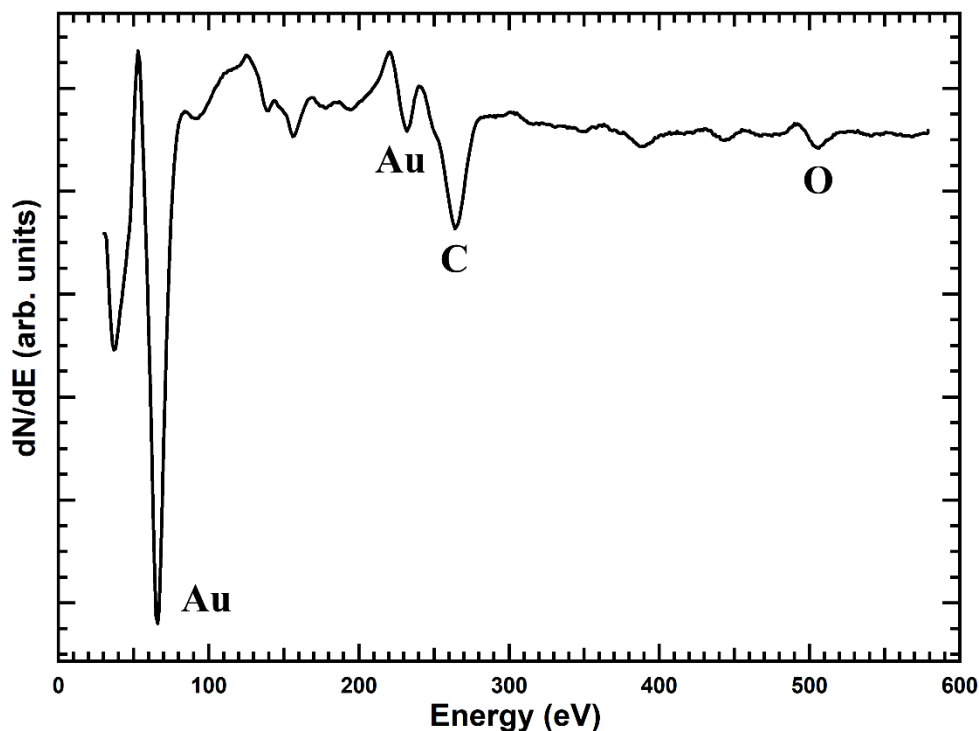


Figure 6.3. An Auger spectrum of a TBTANG covered Au(111) surface.

6.3 Results and Discussion

6.3.1 Adsorption of TBTANG on Au(111)

1) Molecular Adsorption with the Substrate at RT

Dosing TBTANG onto Au(111) held at room temperature yields a self-assembled molecular network consisting of intact molecules, with extended domains that follow the herringbone structure of the substrate. Figure 6.4 is an STM image with a scan area of $36 \text{ nm} \times 36 \text{ nm}$. In this image, triangular features corresponding to intact TBTANG molecules are easily identified. STM line profiles (not shown) reveal a

1 nm separation between two Br atoms in each corner of the molecule, in agreement with a 1.03 nm distance suggested by DFT [157].

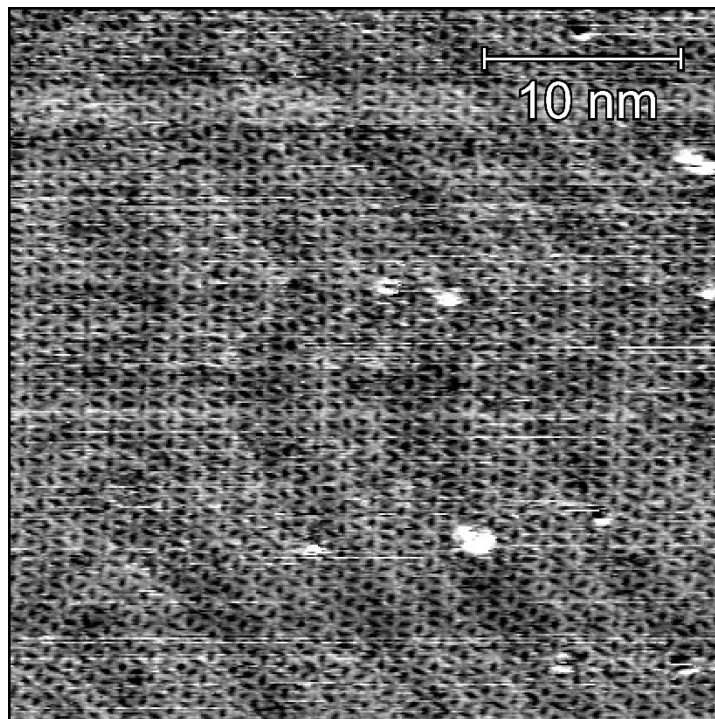


Figure 6.4. Self-assembly of TBATBG on Au(111) at RT. Insert is a demonstration of the elementary structural motif.

On closer inspection, we find that the repeating motif is a pair of three-spoke molecules, rotated by 180° with respect to each other (Figure 6.5). The results are consistent with the unpublished results of DeMarchi and Gianluca *et al.* where it was determined that the molecules interact via non-covalent halogen-halogen interactions [157], with a Br \cdots Br distance of 0.39 nm. The unit cell for this molecular structure is an oblique cell with a long 1.9 nm side and a short 1.5 nm side, consistent with DFT calculations based on a free-standing layer [157]. For further details regarding the properties of the TBTANG SAMN on Au the reader is directed to DeMarchi and Gianluca *et al.* [157].

2) Molecular Adsorption on a Hot Surface

The direct polymerization of TBTANG molecules on Au(111) was studied by depositing the monomers onto a surface held at a temperature above the debromination threshold (130 °C). Upon adsorption, bromine atoms are readily decoupled, resulting in surface-confined triradicals that subsequently undergo polymerization.

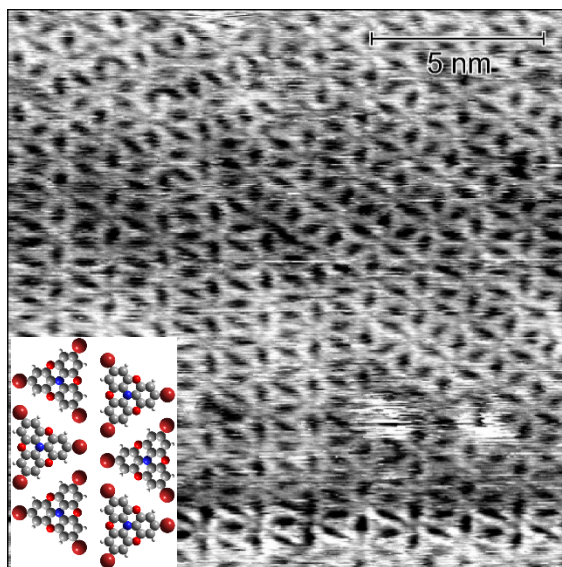


Figure 6.5. A detailed STM image of the RT structure of TBTANG on gold.

As shown in Figure 6.6, dosing TBTANG onto a hot Au(111) surface results in a complete polymeric monolayer. The polymer can be characterized by large honeycomb domains. Such a network is obtained by depositing TBTANG molecules to an Au(111) surface kept at 130 °C. The extent and the quality of the resultant polymeric layer exceeds any surface-confined layer reported in the literature to date [158].

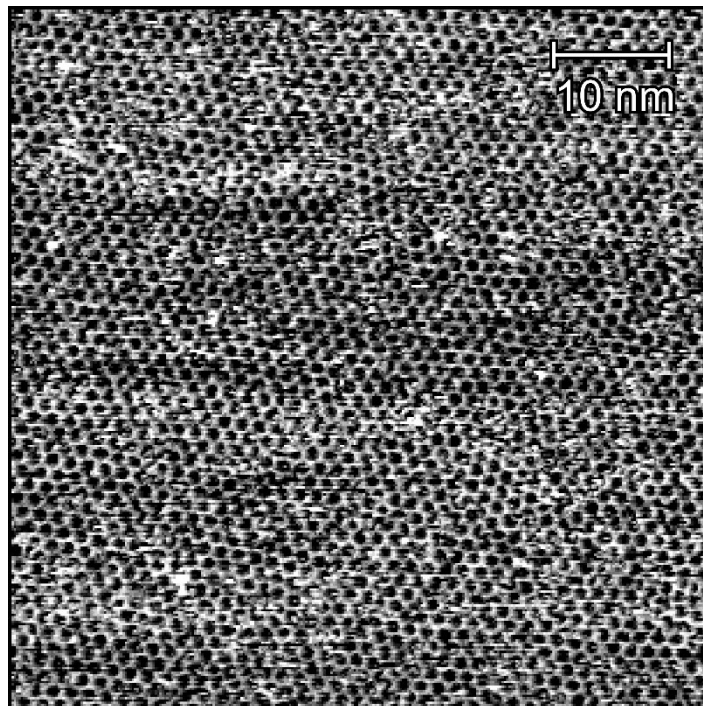


Figure 6. 6. An STM image of 1ML of TBTANG polymer on Au(111).

By analyzing the pore-to-pore distance, we can determine the type of binding between the molecules. In Figure 6.7, the center-to-center spacing between the pores extracted from the STM images gives a length of 1.69 ± 0.05 nm, which is in agreement with the simulated spacing from DFT calculations [158].

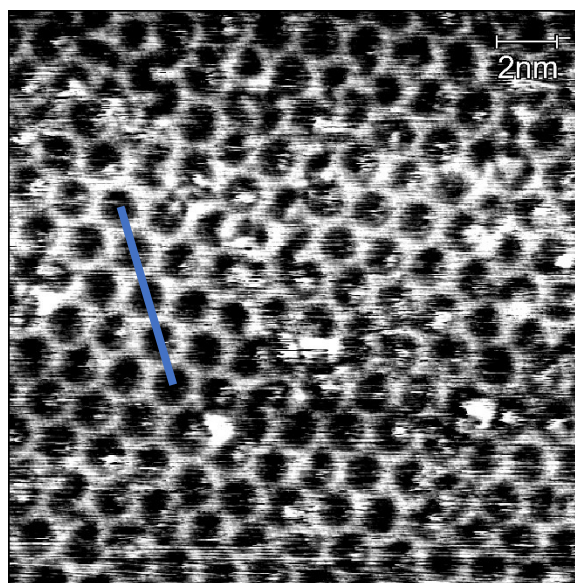


Figure 6.7. A detailed image of the TBTANG polymer. Blue line indicates measurement across four hexagons.

This confirms C–C coupling and the polymeric character of the overlayer formed by TBTANG. Detailed properties of the polymeric layer are discussed in a forthcoming paper by DeMarchi and Galeotti *et al.* [158].

6.3.2 Adsorption of TBTANG onto the Si(111) $\sqrt{3}\times\sqrt{3}$ R30°-Ag Surface

1) Molecular adsorption with Substrate at RT

Surface with one-monolayer of molecules

When 1ML of TBTANG molecules are deposited onto the Si(111) $\sqrt{3}$ -Ag substrate, the molecules self-assemble and extend over the entire surface (Figure 6.8). A number of fuzzy white features are observed indicating weakly bound second layer molecules. Defects due to point defects and domain boundaries in the underlying Si(111) $\sqrt{3}$ -Ag substrate are still observed (white arrows in Figure 6.8). Unlike the adsorption of TBTTA and TIPT molecules onto the Si(111) $\sqrt{3}$ -Ag surface discussed in Chapters 4 and 5, where we found that the self-assembly of molecules is extremely sensitive to the degree

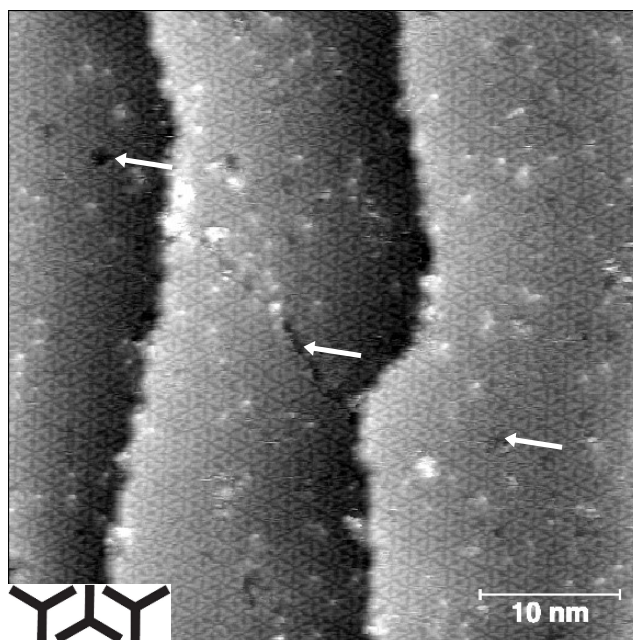


Figure 6.8. STM image of $\sqrt{3}$ -Ag surface covered by one complete layer of TBTANG ($V_{\text{sample}} = -1.13$ V, $I = 1000$ pA). Defects due to a domain boundary and point defects in the substrate are indicated by white arrows.

of perfection of the substrate, this does not appear to be the case for TBTANG. In the case of TBTTA and TIPT, the size of the domains is often limited by the number of point defects and domain boundaries in the Si(111) $\sqrt{3}$ -Ag substrate. In contrast, we find that although defects in the $\sqrt{3}$ -Ag layer do affect the integrity of the domains, they do not limit their extent.

On closer inspection, the ordered structure is characterized by parallel rows of intact TBTANG molecules. Within the rows the repeating motif is a pair of three-spoke molecules, rotated by 180° with respect to each other. The molecules are close-packed with the end-groups of one molecule lying adjacent the end-groups of the adjacent molecules (see insert in Figure 6.8).

The geometry of the unit cell we observe for the 1ML of TBTANG on Si(111) $\sqrt{3}$ -Ag surface is, $|\vec{a}| = 19.1 \pm 0.5 \text{ \AA}$, $|\vec{b}| = 15.3 \pm 0.5 \text{ \AA}$ and $\gamma = 60^\circ \pm 2^\circ$ (Figure 6.9). Note, the grey dots in this figure are just a representation of the $\sqrt{3}$ lattice. We are not assigning them to any particular feature in the $\sqrt{3}$ -Ag layer since we do not have images to determine the exact registry between the molecular overlayer and the $\sqrt{3}$ -Ag substrate. The size and symmetry of the unit cell is identical to the cell observed on the

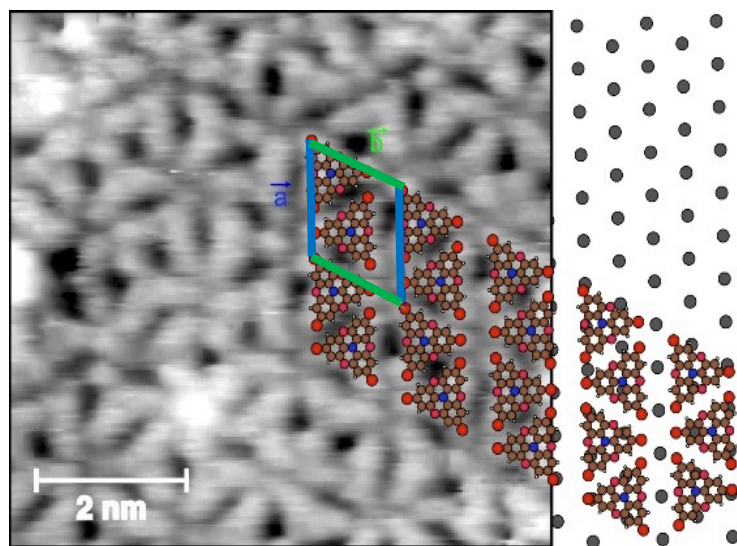


Figure 6.9. $10\text{ \AA} \times 10\text{ \AA}$ STM image of self-assembly structure observed for TBTANG on $\sqrt{3}$ -Ag ($V_{\text{sample}} = -0.84 \text{ V}$, $I = 384 \text{ pA}$). The grey dots in the substrate represent the $\sqrt{3}$ lattice.

Au(111) surface and suggests that the unit cell on Si(111) $\sqrt{3}$ -Ag is determined primarily by intermolecular interactions and that the structure of the overlayer is relatively independent of the substrate.

Sub-monolayer coverage

Figure 6.10 shows an STM image of the surface with a molecular coverage of approximately 0.9 ML. As with a complete layer, large self-assembled domains of intact molecules extend over the entire surface. That said, some ‘gaps’ (black arrows) are present between molecular rows. On closer inspection, we find that the size of the gaps is not random, and we believe the variation is due to a misfit between the row spacing of the overlayer and periodicity of underlying $\sqrt{3}$ -Ag lattice. As can be seen in Figure 6.9, for a complete layer two rows of molecules correspond to the spacing between five rows of $\sqrt{3}$ -Ag lattice, thus every second row is commensurate with the substrate. At sub-monolayer coverage, depending on how the molecular domains start or terminate, the spacing difference between the $\sqrt{3}$ -Ag spacing and the molecular rows can lead to misfit dislocations and thus “gaps”.

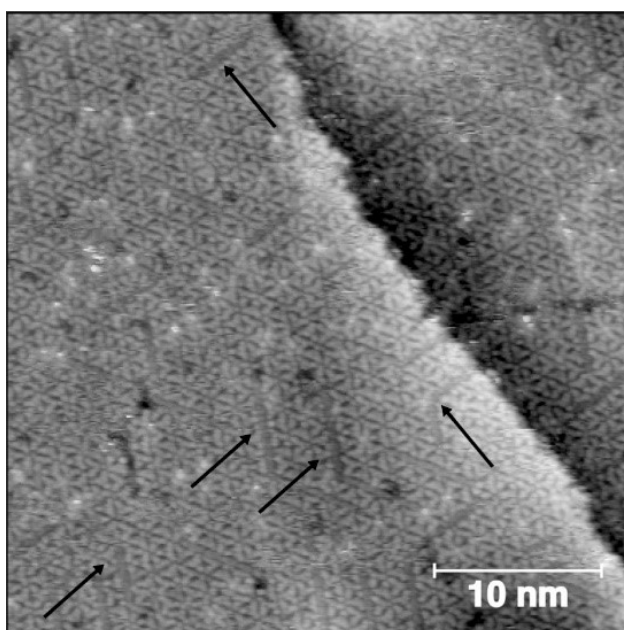


Figure 6.10. STM image of ~ 0.9 ML of TBTANG on $\sqrt{3}$ -Ag surface ($V = -1.24$ V, $I = 487$ pA). The ‘gaps’ between the domains are pointed out with black arrows.

For instance, if two domains are separated by a single $\sqrt{3}$ -Ag row this yields a gap of ~ 0.58 nm. The lower gap in Figure 6.11 is an example of this scenario. Another possibility exists if two domains meet and neither of the end rows have a commensurate relationship with substrate. In this instance a gap of ~ 0.68 nm results (see upper gap in Figure 6.11). Note, we are not able to determine the relative position of the molecules with respect to the underlying $\sqrt{3}$ -Ag lattice. Experimental measurements of the gap size from all available data can be grouped into either a “short gap” with a range of $0.59 \text{ nm} \leq d_{\text{gap}} \leq 0.64 \text{ nm}$, or a “long gap” in the range of $0.66 \text{ nm} \leq d_{\text{gap}} \leq 0.71 \text{ nm}$. Note that the size of the gaps is consistent with two misfit dislocations discussed above.

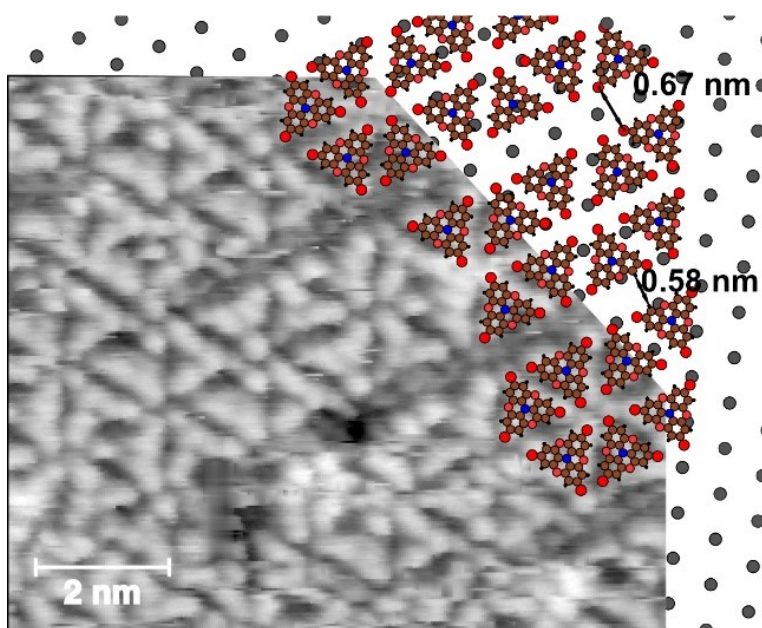


Figure 6.11. A zoomed-in image of the gaps ($V_{\text{sample}} = -1.13 \text{ V}$, $I = 560 \text{ pA}$). The upper gap corresponding to a “long gap” with a width of 6.7 \AA . Lower gap corresponding to an “short gap” with a width of 5.8 \AA . Extension part of the image shows the proposed molecular configuration with respect to the $\sqrt{3}$ lattice in the substrate.

This phenomenon indicates that while the self-assembly of molecules is dominated by the inter-molecular interaction at complete coverage, when the molecular coverage is decreased, the overlayer exhibit features (gaps) which have a definite commensurate relation with the underlying substrate.

Lower coverage surface

Figure 6.12 shows an image with a coverage of ~ 0.7 ML. The size of the domains decreases and more empty regions in addition to gaps are observed between the domains. At this coverage, the molecular structures are still quite stable and survive repeated scanning.

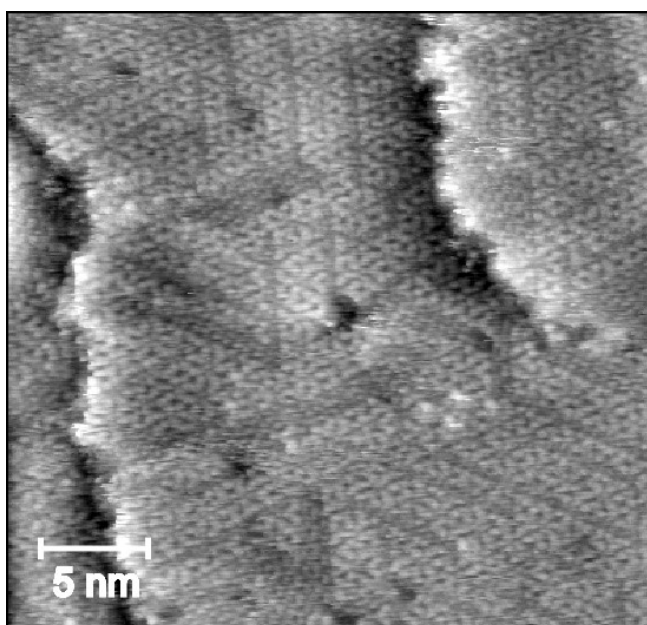


Figure 6.12. TBTANG overlayer at ~ 0.7 ML coverage shows decreased domain size and more empty space between the domains. ($V_{\text{sample}} = -1.27$ V, $I = 483$ pA).

At still lower coverage (0.3 ML), only a mixture of one and two molecular row structures of TBTANG are observed (Figure 6.13). At this stage, the supramolecular structures are not as robust. With repeated scanning we observe single molecules attaching or detaching from the chains. The attachment/detachment of monomers indicates a relatively weak molecule-molecule interaction. We ascribe the additional corrugations/rows to diffusing molecules. From STM images (see yellow lines in Figure 6.13), we find the molecular rows are observed in three rotational domains consistent with the C_{3v} symmetry of the underlying substrate.

We find that both the intra-row spacing along the rows and inter-row spacing between the rows differs somewhat from what was measured on a complete layer. The dimensions of the intra-row and inter-row

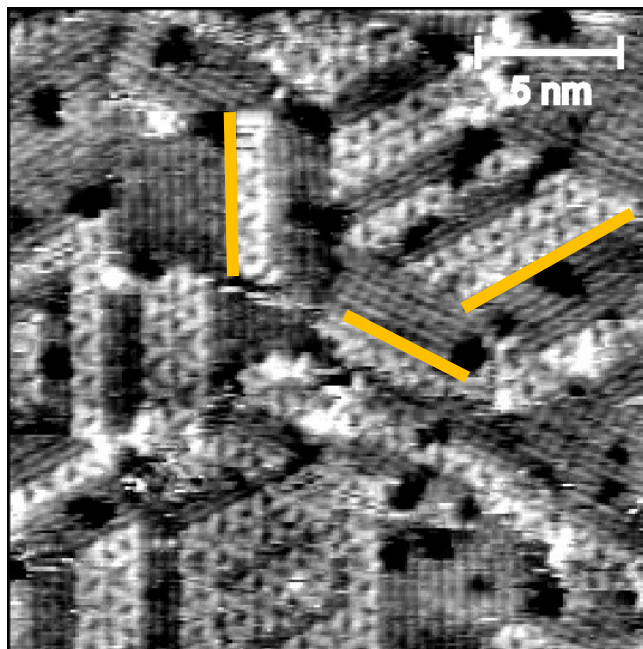


Figure 6. 13. Image of the self-assembled structures on $\sqrt{3}$ -Ag at 0.3ML coverage. Only 1-d and 2-d rows are observed at low coverage.

spacing are highlighted in the low coverage STM image (Figure 6.14) and found to be $|\vec{a}| = 17.4 \pm 0.5 \text{ \AA}$ and $|\vec{b}| = 12.8 \pm 0.5 \text{ \AA}$. Both dimensions are more compressed in comparison with the unit cell observed on the complete layer. The reduction is assumed to be due to a reduction in the number of nearest neighbor molecules at low coverage. In a complete layer each molecule interacts with six nearest neighbors while the number drops to four when the structure only contains two rows.

By comparing the STM images obtained from surfaces with different molecular coverages, we can make some interesting observations. On surfaces with a coverage of $< 1\text{ML}$, we find that the substrate has a templating effect on the resultant supramolecular structure. Considering our experience with the adsorption of TBTTA and TIPT (Chapters 4 and 5 respectively), it is not surprising that the Si(111) $\sqrt{3}$ -Ag substrate can affect the molecular arrangement of the overlayer. However, in these previous studies, defects in the Si(111) $\sqrt{3}$ -Ag substrate limited the size of the supramolecular domains. In the case

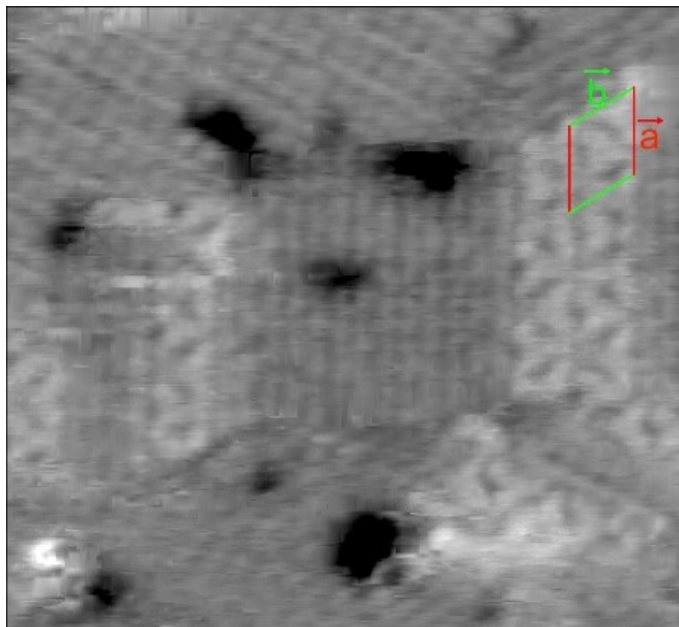


Figure 6.14. A detailed image of a low coverage surface. Intra-row spacing a and inter-row spacing b .

of TBTANG, this did not seem to be the case. Both the size and the symmetry of the unit cell are identical to that observed on Au(111) and DFT calculations of a free standing layer [157]. This indicates that the molecular arrangement of TBTANG on the Si(111) $\sqrt{3}$ -Ag surface at one monolayer is primarily determined by the inter-molecular forces. The substrate acts as an inert template to support the self-assembly and has a negligible effect on the layer structure.

2) Effect of Annealing

As discussed, similar to the behavior on Au(111) surface, TBTANG molecules stay intact on the Si(111) $\sqrt{3}$ -Ag surface at room temperature. Therefore, additional thermal energy is needed to activate dehalogenation. Preliminary post-deposition annealing experiments are discussed below.

Annealing at ~90 °C

We have investigated the structure of the molecular overlayer following annealing to ~90 °C. The molecular overlayer on much of the terraces appears to remain unaffected. However, disordered regions appear at the lower part of the atomic steps (Figure 6.15). As we know step-edges can provide active sites [159, 160] which can trigger many catalytic processes [161, 162]. In our case, we identify the step-edges as active sites which promote the dissociation of the C–Br bond in the TBTANG molecules adjacent to the step-edges first. The liberated bromine atoms appear to interact destructively with the substrate, leading to a defective substrate starting from step-edges which then spreads to the terraces as observed.

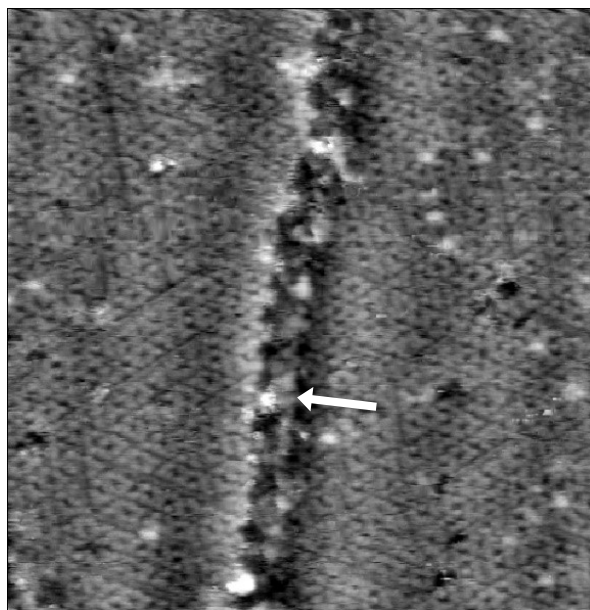


Figure 6. 15. Surface after annealing at 90°C for 30 minutes ($V_{\text{sample}} = -1.16$ V, $I = 740$ pA). Accumulation of the molecules started by the lower part of the step edge (white arrow).

Anneal at ~100 °C

Following further annealing to ~100 °C, the extent of these disordered regions continues to expand (Figure 6.15). We believe that at this temperature, a larger fraction of the TBTANG molecules

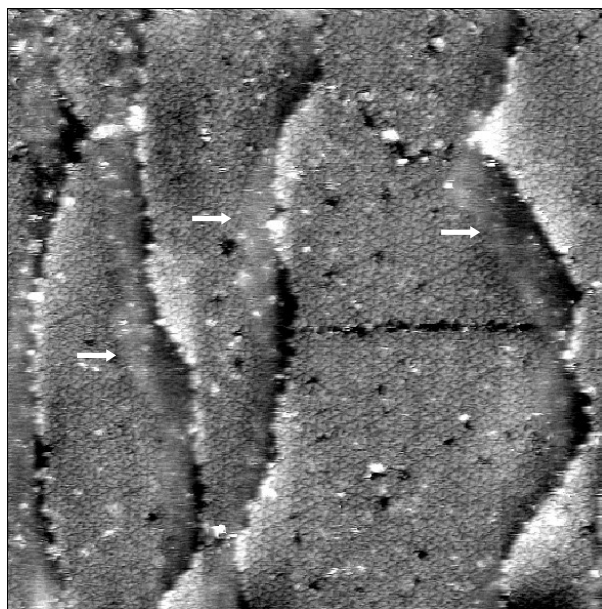


Figure 6.16. Surface after annealing at 100°C for 30 minutes ($V_{\text{sample}} = -1.18$ V, $I = 800$ pA). Disordered regions started to extend from step edges to terraces.

dehalogenate. As we observed with TIPT (Chapter 5), the free halogen atoms on the surface can then react with the silver atoms in the substrate and can lead to a more defective substrate and a dramatic decrease in molecular mobility.

6.4 Summary

In this chapter, we discussed the adsorption of a halogenated molecule, TBTANG, on both a single crystal Au(111) surface, and the semiconducting Si(111) $\sqrt{3}$ -Ag surface. Dosing TBTANG molecules onto a RT Au(111) surface leads to the self-assembly of intact molecules, stabilized by Br \cdots Br interactions. The repeating motif of the SAMN is a pair of three-spoke molecules, rotated by 180° with respect to each other. The unit cell is an oblique cell with dimensions of 1.9 nm by 1.5 nm and are consistent with DFT calculations based on a free-standing layer [157].

Deposition of TBTANG onto a hot Au(111) surface yields a complete polymer layer. By measuring the pore-to-pore distance extracted from STM and comparing the result with DFT calculations, we confirm

the polymeric character of the TBTANG overlayer. The quality, and extent of the polymer domains exceeds any previous reports elsewhere [158].

TBTANG molecules remain intact following deposition onto a Si(111) $\sqrt{3}$ -Ag surface kept at RT. At 1ML, TBTANG forms a complete SAMN characterized by an oblique unit cell defined by lattice vectors of $(19.1 \pm 0.5 \text{ \AA})$ and $(15.3 \pm 0.5 \text{ \AA})$ and an angle of 60° . This unit cell is almost identical to the SAMN observed on the Au(111) surface at RT. In contrast to previous results with TBTTA and TIPT, we found that point defects and domain boundaries in the Si(111) $\sqrt{3}$ -Ag substrate do not limit the size of the supramolecular domains. At sub-monolayer coverage ($\sim 0.9\text{ML}$), the molecular layer extends over the entire surface with domains separated by “gaps”. At low coverage, only single or double molecular rows are observed on surface. The spacing between molecules extracted from these low coverage molecular structures is smaller than in the complete monolayer SAMN. We believe this is due to a reduction in the number of nearest neighbors.

At 1ML coverage, inter-molecular interactions dominate the structure of the complete SAMN on Si(111) $\sqrt{3}$ -Ag substrate. However, when coverage drops below 1ML, a clear influence from the substrate is observed, i.e. the observation of ‘gaps’, with definite epitaxial relationships to the $\sqrt{3}$ lattice, and the growth of molecular rows along one of the three C_{3v} high-symmetry directions. In other words, the Si(111) $\sqrt{3}$ -Ag substrate primarily acts as a physical support at 1ML coverage while it does affect the arrangement of molecules at lower coverage.

Unlike the behavior on Au(111), preliminary annealing experiments do not lead to polymerization of the TBTANG layer. Rather, annealing at $\sim 90^\circ\text{C}$ leads to disordered regions which nucleate primarily at step edges. These disordered regions expand with further annealing at a higher temperature. We believe step-edges can provide active sites which lead to the liberation of bromine atoms. The disordered region

is the result of a breakup of the $\sqrt{3}$ -Ag layer due to the chemical interaction between silver and bromine atoms.

Chapter 7

Conclusions and Outlook

Continuous progress in nanoscience opens exciting new pathways for the development of novel functional materials. Among them, is the creation of surface confined low-dimensional molecular structures as a promising alternative to top-down approaches in electronic device fabrication. Highly ordered molecular networks can be obtained either by non-covalent supramolecular self-assembly, or by covalent on-surface synthesis of polymer frameworks.

In this thesis a number of adsorption studies of halogenated organic molecules have been presented both on single crystal metal and passivated silicon surfaces. Three distinct molecular systems have been investigated in detail by a combination of scanning tunneling microscopy (STM), Auger electron spectroscopy (AES).

In chapter 4, we presented a study of the adsorption of brominated tetrathienoanthracene (TBTTA) molecules onto the Si(111) $\sqrt{3}$ -Ag surface at room temperature. The two-dimensional $\sqrt{3}$ -Ag adlayer acts to passivate the silicon surface and provides a high-mobility template for TBTTA adsorption. STM images reveal that at low coverage, the molecules readily migrate to step edges and defects in the $\sqrt{3}$ -Ag overlayer. With increasing coverage, the molecules eventually form compact supramolecular structures. In terms of the hexagonal $\sqrt{3}$ lattice vectors ($\mathbf{a}_{\sqrt{3}}$ and $\mathbf{b}_{\sqrt{3}}$), the oblique unit cell of these structures can be defined by lattice vectors $\mathbf{a}_m = 3\mathbf{a}_{\sqrt{3}} + 2\mathbf{b}_{\sqrt{3}}$, and $\mathbf{b}_m = -\mathbf{a}_{\sqrt{3}} + \mathbf{b}_{\sqrt{3}}$. The structures are quite fragile and can decompose under repeated STM imaging. This is particularly true at higher bias and suggests an electric field-induced dissociation in these instances. With increasing molecular dose, the size and stability of the structures increases. At higher coverage, the spatial extent of the supramolecular structures is often limited by defects in the underlying $\sqrt{3}$ -Ag layer. Our results suggest that the Si(111) $\sqrt{3}$ -Ag surface does provide a relatively inert substrate for the adsorption of TBTTA molecules, and that the supramolecular structures are held together by relatively weak intermolecular forces.

In chapter 5, we studied the complex interactions between adsorbates and surfaces, to demonstrate how the reactivity of the substrate can play a major role in molecular arrangement on surfaces. The adsorption of a halogenated organic molecule, 2,4,6-tris(4-iodophenyl)-1,3,5-triazine (TIPT), on the Ag(111) and Si(111) $\sqrt{3}$ -Ag surfaces was compared both at room temperature and following annealing.

Our results indicate that on Ag(111), TIPT molecules dehalogenate upon deposition at RT and form organometallic structures stabilized by silver adatoms. STM images reveal a disordered organometallic network and the atoms between the two adjacent phenyl groups are identified as Ag atoms from the substrate. The effect of post-deposition annealing indicates that polymerization does not occur below 100 °C. A two-dimensional (2-d) polymer can be formed by annealing the sample to between 100 °C and 135 °C for at least 20 minutes, and indicates that additional thermal energy is necessary for the formation of covalent bonds between TIPT radicals.

In contrast to adsorption on Ag metal surfaces, on the Si(111) $\sqrt{3}$ -Ag surface we find that TIPT monomers remain largely intact at room temperature. Many STM images show evidence of diffusing species on the surface. In fact, parallel row features are observed due to diffusing molecules. Ordered supramolecular domains are formed with increasing coverage. The size and symmetry of the unit cell associated with these supramolecular features is consistent with domains of intact monomers held together primarily by intermolecular forces. DFT calculations reveal a very weak inter-row interaction thus very small energy is needed to adapt inter-row spacing to the underlying substrate. This explains the origin of the expanded inter-row spacing in our observed cell. The formation of supramolecular domains is extremely sensitive to the quality of the underlying $\sqrt{3}$ -Ag reconstruction. Point defects in the Si(111) $\sqrt{3}$ -Ag reconstruction ultimately restrict the extent of the domains. We also observe that the adsorption of TIPT can in turn produce a small increase in defect density of the $\sqrt{3}$ -Ag layer. We believe

these additional defects are the result of interactions between the Si(111) $\sqrt{3}$ -Ag surface and free iodine, which is the by-product of the dehalogenation of a small fraction of the adsorbed TIPT molecules.

Annealing the supramolecular layer does not lead to a polymerization, but rather leads to a more disordered surface. Increased dehalogenation leads to a dramatic increase in the amount of free iodine atoms on the surface and these iodine atoms can interact with silver atoms in the $\sqrt{3}$ -Ag layer and result in a surface with higher defect density. The lower mobility results in a more disordered molecular overlayer.

In chapter 6, we presented an investigation of the adsorption of another halogenated molecule with threefold symmetry, TBTANG, on the Au(111) and Si(111) $\sqrt{3}$ -Ag surfaces. We were able to confirm both the self-assembly and polymerization results on Au(111) to be published by F. DeMarchi and G. Galeotti *et al.* [157, 158]. Dosing TBTANG onto Au(111) at room temperature yields a long-range self-assembled structure consisting of intact molecules stabilized primarily by Br \cdots Br halogen bonding interactions, with extended domains that follow the herringbone structure of the gold substrate. The repeating motif of the structure is a pair of these molecules, rotated by 180° with respect to each other, with a Br \cdots Br separation of 0.39 nm.

A complete monolayer of honeycomb polymer can be obtained by depositing TBTANG molecules onto a hot Au(111) surface above the de-halogenation temperature. Instead of a two-step Ullman reaction, which is the most common route for the preparation of ordered 2-d conjugated polymers, the approach allows for a one-step polymerization. In the case of TBTANG, this approach overcomes a negative templating effects that occurs with the intermediate proto-polymer, and achieves an ideal coupling-to-diffusion ratio that reduces the formation of defects, and thus produces a dramatically improved polymer.

We extended the study of TBTANG to the Si(111) $\sqrt{3}$ -Ag surface. At room temperature TBTANG molecules behave similarly on Si(111) $\sqrt{3}$ -Ag compared with the Au(111) surface. Upon deposition, the molecules display a high mobility, and with increasing coverage, TBTANG exhibits the long-range self-assembly of intact molecules. At one monolayer, the repeating motif is almost identical to that observed on Au(111) at room temperature. The self-assembled layer extends over the entire surface and while defects in the $\sqrt{3}$ -Ag substrate affect the integrity of domains, they do not limit the size. Unlike the gold surface, post-deposition annealing does not lead to polymerization. In contrast, disordered regions are observed to grow out from the step edges.

As a consequence of this work, it became apparent that the Si(111) $\sqrt{3}$ -Ag does provide a suitable template for the self-assembly of halogenated molecules at room temperature. Unfortunately, any attempts to polymerize the molecules via an Ullman type reaction proved unsuccessful. Unlike single crystal metal surfaces (i.e. Au(111) and Ag(111)), the $\sqrt{3}$ -Ag surface reacts more dramatically with the halogen atoms cleaved from molecules after dehalogenation. The results indicate that that Ullmann type polymerization is not an option on the Si(111) $\sqrt{3}$ -Ag surface. In order to realize the ultimate goal of producing a polymer with a high degree of order and electronic conjugation in 2-d on a semiconducting surface, several alternate approaches should be attempted.

One approach would be to stay with halogenated molecules which give promising results on metal surfaces (TBTANG), but deposit them onto another passivated silicon surfaces such as the Si(111) $\sqrt{3}$ -B surface which has already been shown to provide enough mobility for the diffusion of halogenate molecules [140, 163-165]. However, the drawback with this approach may be that without the presence of a noble metal catalyst, considerable energy will be required for dehalogenation. Whether the halogen bonds will cleave while still keeping the integrity of the rest of the molecules intact is an open question.

One alternative would be to synthesize highly ordered polymers on a different substrate and subsequently transfer them to desired semiconducting surface. Since most successful examples of 2-d Ullmann type coupling have taken place on metal substrates, transferring highly ordered polymers to semiconducting/insulating could be a feasible way to produce a hybrid system. One pioneering example is the atomically precise synthesis of graphene nanoribbons (GNR) on gold films subsequently transferred onto a SiO₂ substrate [166]. However, this requires sacrificing the gold substrate used for GNR synthesis, and the process is relatively complex.

Another path would be to explore other approaches to polymerization. i.e. via condensation reactions. One recent example demonstrated the self-dehydration reaction of benzene-1,4-diboronic acid (BDDBA) leads to the formation of boroxine rings and to an extended 2-d polymer under UHV by Clair *et al.* [91]. Other approaches to coupling like Glaser-type reactions and intermolecular dehydrogenation are also being widely explored, however to date the results are far less successful than Ullmann coupling.

Recently, great effort has been devoted to exploring an approach to create molecular architectures based on chemical components that interact through more robust, yet reversible bonds [167]. Compared to conventional covalent chemistry which operates under kinetic control, dynamic covalent chemistry (DCC) is a thermodynamically controlled process which shares a number of features with supramolecular chemistry [167-170]. For example, dynamic covalent bonds are reversible and can be reconstructed. Guan and coworkers [171] synthesized highly ordered boronic acid-based surface covalent organic frameworks (SCOFs) of large extent on HOPG using biphenyldiboronic (BPDA) as precursor. By introducing a small amount of water, the chemical equilibrium of the dehydration reaction of boronic acid can be manipulated. Conceptually similar procedures could be applied to the semiconducting substrates we are interested in. However, some semiconducting surfaces can only be investigated under ultra-high vacuum. Thus how to make experiments using this DCC approach compatible with UHV system remains challenging.

References

- [1] A. Gourdon, *On-Surface Synthesis*, Springer, Switzerland, 2016.
- [2] G. Binnig, H. Rohrer, *SCANNING TUNNELING MICROSCOPY*, *Helvetica Physica Acta*, 55 (1982) 726-735.
- [3] R.P. Feynman, *There's Plenty of Room at the Bottom*, *Engineering and Science*, 23 (1960) 14.
- [4] G.M. Whitesides, J.P. Mathias, C.T. Seto, *Molecular self-assembly and nanochemistry: a chemical strategy for the synthesis of nanostructures*, *Science*, 254 (1991) 1312-1319.
- [5] G.M. Whitesides, B. Grzybowski, *Self-Assembly at All Scales*, *Science*, 295 (2002) 2418-2421.
- [6] J.V. Barth, G. Costantini, K. Kern, *Engineering atomic and molecular nanostructures at surfaces*, *Nature*, 437 (2005) 671.
- [7] J.V. Barth, *Molecular Architectonic on Metal Surfaces*, *Annual Review of Physical Chemistry*, 58 (2007) 375-407.
- [8] K.S. Mali, J. Adisojoso, E. Ghijsens, I. De Cat, S. De Feyter, *Exploring the Complexity of Supramolecular Interactions for Patterning at the Liquid–Solid Interface*, *Accounts of Chemical Research*, 45 (2012) 1309-1320.
- [9] D.E. Hooks, T. Fritz, M.D. Ward, *Epitaxy and Molecular Organization on Solid Substrates*, *Adv. Mater.*, 13 (2001) 227-241.
- [10] T.A. Pham, F. Song, M.-T. Nguyen, M. Stöhr, *Self-assembly of pyrene derivatives on Au(111): substituent effects on intermolecular interactions*, *Chem. Commun.*, 50 (2014) 14089-14092.
- [11] S. De Feyter, F.C. De Schryver, *Self-Assembly at the Liquid/Solid Interface: STM Reveals*, *The Journal of Physical Chemistry B*, 109 (2005) 4290-4302.
- [12] B.J. Gyarfas, B. Wiggins, M. Zosel, K.W. Hipps, *Supramolecular Structures of Coronene and Alkane Acids at the Au(111)–Solution Interface: A Scanning Tunneling Microscopy Study*, *Langmuir*, 21 (2005) 919-923.
- [13] M.J.E. Resendiz, J.C. Noveron, H. Disteldorf, S. Fischer, P.J. Stang, *A Self-Assembled Supramolecular Optical Sensor for Ni(II), Cd(II), and Cr(III)*, *Organic Letters*, 6 (2004) 651-653.
- [14] J.T. Davis, G.P. Spada, *Supramolecular architectures generated by self-assembly of guanosine derivatives*, *Chemical Society Reviews*, 36 (2007) 296-313.
- [15] L. Grill, M. Dyer, L. Lafferentz, M. Persson, M.V. Peters, S. Hecht, *Nano-architectures by covalent assembly of molecular building blocks*, *Nature Nanotechnology*, 2 (2007) 687-691.
- [16] M. Treier, N.V. Richardson, R. Fasel, *Fabrication of Surface-Supported Low-Dimensional Polyimide Networks*, *J. Am. Chem. Soc.*, 130 (2008) 14054-14055.
- [17] R. Gutzler, H. Walch, G. Eder, S. Kloft, W.M. Heckl, M. Lackinger, *Surface mediated synthesis of 2D covalent organic frameworks: 1,3,5-tris(4-bromophenyl)benzene on graphite(001), Cu(111), and Ag(110)*, *Chem. Commun.*, DOI 10.1039/b906836h(2009) 4456-4458.
- [18] W. Wang, X. Shi, S. Wang, M.A. Van Hove, N. Lin, *Single-Molecule Resolution of an Organometallic Intermediate in a Surface-Supported Ullmann Coupling Reaction*, *J. Am. Chem. Soc.*, 133 (2011) 13264-13267.
- [19] R. Gutzler, L. Cardenas, J. Lipton-Duffin, M. El Garah, L.E. Dinca, C.E. Szakacs, C.Y. Fu, M. Gallagher, M. Vondracek, M. Rybachuk, D.F. Perepichka, F. Rosei, *Ullmann-type coupling of brominated tetrathienoanthracene on copper and silver*, *Nanoscale*, 6 (2014) 2660-2668.
- [20] T. Leftwich, A. Teplyakov, *Chemical manipulation of multifunctional hydrocarbons on silicon surfaces*, *Surf. Sci. Rep.*, 63 (2007) 1-71.
- [21] A. Vilan, O. Yaffe, A. Biller, A. Salomon, A. Kahn, D. Cahen, *Molecules on Si: Electronics with Chemistry*, *Adv. Mater.*, 22 (2010) 140-159.
- [22] M.D. Upward, P. Moriarty, P.H. Beton, *Double domain ordering and selective removal of C₆₀ on Ag/Si(111)-(√3×√3)R30°*, *Phys. Rev. B*, 56 (1997) R1704-R1707.

- [23] P. Guaino, D. Carty, G. Hughes, P. Moriarty, A.A. Cafolla, Scanning tunneling microscopy study of pentacene adsorption on Ag/Si(1 1 1)-(√3 × √3)R30°, *Applied Surface Science*, 212-213 (2003) 537-541.
- [24] D.L. Keeling, N.S. Oxtoby, C. Wilson, M.J. Humphry, N.R. Champness, P.H. Beton, Assembly and Processing of Hydrogen Bond Induced Supramolecular Nanostructures, *Nano Letters*, 3 (2003) 9-12.
- [25] J.A. Theobald, N.S. Oxtoby, M.A. Phillips, N.R. Champness, P.H. Beton, Controlling molecular deposition and layer structure with supramolecular surface assemblies, *Nature*, 424 (2003) 1029.
- [26] T. Suzuki, T. Lutz, D. Payer, N. Lin, S.L. Tait, G. Costantini, K. Kern, Substrate effect on supramolecular self-assembly: from semiconductors to metals, *Physical Chemistry Chemical Physics*, 11 (2009) 6498-6504.
- [27] R. Liu, C. Fu, D.F. Perepichka, M.C. Gallagher, Supramolecular structures of halogenated oligothiophenes on the Si(111)-root 3 x root 3-Ag surface, *Surface Science*, 647 (2016) 51-54.
- [28] T. Nakayama, S. Watanabe, M. Aono, Structure and stability of the out-of-phase boundary in a surface superlattice, Si(111)root 3x root 3R30 degrees-Ag, *Surface Science*, 344 (1995) 143-148.
- [29] F.D. Marchi, G. Galeotti, M. Simenas, M.C. Gallagher, E. Hamzehpoor, D. Dettmann, G. Contini, M. Ebrahimi, E.E. Tornau, D.F. Perepichka, F. Rosei, Supramolecular Ordering of a Heterotriangulene molecule on Au(111) To be published.
- [30] K. Yagi, K. Takayanagi, K. Kobayashi, N. Osakabe, Y. Tanishiro, G. Honjo, Surface study by an UHV electron microscope, *Surface Science*, 86 (1979) 174-181.
- [31] C. Wöll, S. Chiang, R.J. Wilson, P.H. Lippel, Determination of atom positions at stacking-fault dislocations on Au(111) by scanning tunneling microscopy, *Phys. Rev. B*, 39 (1989) 7988-7991.
- [32] A.R. Sandy, S.G.J. Mochrie, D.M. Zehner, K.G. Huang, D. Gibbs, Structure and phases of the Au(111) surface: X-ray-scattering measurements, *Phys. Rev. B*, 43 (1991) 4667-4687.
- [33] K. Takayanagi, Y. Tanishiro, S. Takahashi, M. Takahashi, STRUCTURE-ANALYSIS OF SI(111)-7X7 RECONSTRUCTED SURFACE BY TRANSMISSION ELECTRON-DIFFRACTION, *Surface Science*, 164 (1985) 367-392.
- [34] D.E. Brown, D.J. Moffatt, R.A. Wolkow, Isolation of an intrinsic precursor to molecular chemisorption, *Science*, 279 (1998) 542-544.
- [35] T. Takahashi, S. Nakatani, N. Okamoto, T. Ishikawa, S. Kikuta, STUDY ON THE SI(111) SQUARE-ROOT-3 X SQUARE-ROOT-3-AG SURFACE-STRUCTURE BY X-RAY-DIFFRACTION, *Japanese Journal of Applied Physics Part 2-Letters*, 27 (1988) L753-L755.
- [36] T. Takahashi, S. Nakatani, N. Okamoto, T. Ishikawa, S. Kikuta, A STUDY OF THE SI(111)-SQUARE-ROOT-3X-SQUARE-ROOT-3-AG SURFACE BY TRANSMISSION-X-RAY DIFFRACTION AND X-RAY-DIFFRACTION TOPOGRAPHY, *Surface Science*, 242 (1991) 54-58.
- [37] T. Takahashi, S. Nakatani, REFINEMENT OF THE SI(111)ROOT-3X-ROOT-3-AG STRUCTURE BY SURFACE X-RAY-DIFFRACTION, *Surface Science*, 282 (1993) 17-32.
- [38] H. Aizawa, M. Tsukada, N. Sato, S. Hasegawa, Asymmetric structure of the Si(111)-3x3-Ag surface, *Surface Science*, 429 (1999) L509-L514.
- [39] J. Wang, K. Liu, L. Ma, X. Zhan, Triarylamine: Versatile Platform for Organic, Dye-Sensitized, and Perovskite Solar Cells, *Chem. Rev.*, 116 (2016) 14675-14725.
- [40] K.-H. Chung, J. Park, K.Y. Kim, J.K. Yoon, H. Kim, S. Han, S.-J. Kahng, Polymorphic porous supramolecular networks mediated by halogen bonds on Ag(111), *Chem. Commun.*, 47 (2011) 11492-11494.
- [41] S. Menzli, B. Ben Hamada, I. Arbi, A. Souissi, A. Laribi, A. Akremi, C. Chefi, Adsorption study of copper phthalocyanine on Si(111)(√3 × √3)R30°Ag surface, *Applied Surface Science*, 369 (2016) 43-49.
- [42] D.V. Gruznev, A.V. Matetskiy, L.V. Bondarenko, A.V. Zotov, A.A. Saranin, J.P. Chou, C.M. Wei, Y.L. Wang, Dim C60 fullerenes on Si(111) 3x3-Ag surface, *Surface Science*, 612 (2013) 31-36.
- [43] A. Jahanbekam, B. Chilukuri, U. Mazur, K.W. Hipps, Kinetically Trapped Two-Component Self-Assembled Adlayer, *The Journal of Physical Chemistry C*, 119 (2015) 25364-25376.
- [44] Y. Lu, H. Li, X. Zhu, W. Zhu, H. Liu, How Does Halogen Bonding Behave in Solution? A Theoretical Study Using Implicit Solvation Model, *The Journal of Physical Chemistry A*, 115 (2011) 4467-4475.

- [45] P. Politzer, J.S. Murray, Enthalpy and entropy factors in gas phase halogen bonding: compensation and competition, *CrystEngComm*, 15 (2013) 3145-3150.
- [46] R. Gutzler, L. Cardenas, F. Rosei, Kinetics and thermodynamics in surface-confined molecular self-assembly, *Chem. Sci.*, 2 (2011) 2290-2300.
- [47] A.G. Slater, Y. Hu, L. Yang, S.P. Argent, W. Lewis, M.O. Blunt, N.R. Champness, Thymine functionalised porphyrins, synthesis and heteromolecular surface-based self-assembly, *Chem. Sci.*, 6 (2015) 1562-1569.
- [48] L. Xu, X. Miao, X. Ying, W. Deng, Two-Dimensional Self-Assembled Molecular Structures Formed by the Competition of van der Waals Forces and Dipole–Dipole Interactions, *The Journal of Physical Chemistry C*, 116 (2012) 1061-1069.
- [49] L.-y. Liao, X.-m. Zhang, F.-y. Hu, S. Wang, S.-D. Xu, Q.-d. Zeng, C. Wang, Two-Dimensional Supramolecular Self-Assembly of Stilbene Derivatives with Ester Groups: Molecular Symmetry and Alkoxy Substitution Effect, *The Journal of Physical Chemistry C*, 118 (2014) 7989-7995.
- [50] H.-Y. Gao, H. Wagner, P.A. Held, S. Du, H.-J. Gao, A. Studer, H. Fuchs, In-plane Van der Waals interactions of molecular self-assembly monolayer, 106 (2015) 081606.
- [51] T. Yokoyama, S. Yokoyama, T. Kamikado, S. Mashiko, Nonplanar adsorption and orientational ordering of porphyrin molecules on Au(111), *The Journal of Chemical Physics*, 115 (2001) 3814-3818.
- [52] T. Yokoyama, S. Yokoyama, T. Kamikado, Y. Okuno, S. Mashiko, Selective assembly on a surface of supramolecular aggregates with controlled size and shape, *Nature*, 413 (2001) 619.
- [53] E. Arunan, G. Desiraju, R. A. Klein, J. Sadlej, S. Scheiner, I. Alkorta, D. Clary, R. Crabtree, J. J. Duannenberg, P. Hobza, H. G. Kiaergaard, A. Legon, B. Mennucci, D. Nesbitt, Definition of the Hydrogen Bond, 2010.
- [54] G.R. Desiraju, Chemistry beyond the molecule, *Nature*, 412 (2001) 397.
- [55] G.R. Desiraju, Hydrogen Bridges in Crystal Engineering: Interactions without Borders, *Accounts of Chemical Research*, 35 (2002) 565-573.
- [56] E. Arunan, Desiraju, G. R., Klein, R. A., Sadlej, J., Scheiner, S., Alkorta, I., Clary, D. C., Crabtree, R. H., Dannenberg, J. J. and Hobza, P., Definition of the hydrogen bond (IUPAC Recommendations 2011), *Pure Appl. Chem.*, 83 (2011) 4.
- [57] T. Neuheuser, B.A. Hess, C. Reutel, E. Weber, Ab Initio Calculations of Supramolecular Recognition Modes. Cyclic versus Noncyclic Hydrogen Bonding in the Formic Acid/Formamide System, *The Journal of Physical Chemistry*, 98 (1994) 6459-6467.
- [58] C.-S. Wang, Y. Zhang, K. Gao, Z.-Z. Yang, A new scheme for determining the intramolecular seven-membered ring N–H···O C hydrogen-bonding energies of glycine and alanine peptides, 123 (2005) 024307.
- [59] M.W. Feyereisen, D. Feller, D.A. Dixon, Hydrogen Bond Energy of the Water Dimer, *The Journal of Physical Chemistry*, 100 (1996) 2993-2997.
- [60] G.R.a.T.S. Desiraju, *The weak hydrogen bond*, Oxford: Oxford University Press, 1999.
- [61] G.A. Jeffrey, *An introduction to hydrogen bonding*, Oxford University Press, New York, 1997.
- [62] G. Pawin, K.L. Wong, K.-Y. Kwon, L. Bartels, A Homomolecular Porous Network at a Cu(111) Surface, 313 (2006) 961-962.
- [63] W. Xu, M. Dong, H. Gersen, E. Rauls, S. Vázquez-Campos, M. Crego-Calama, D.N. Reinhoudt, I. Stensgaard, E. Laegsgaard, T.R. Linderoth, F. Besenbacher, Cyanuric Acid and Melamine on Au(111): Structure and Energetics of Hydrogen-Bonded Networks, 3 (2007) 854-858.
- [64] N.A. Wasio, R.C. Quardokus, R.P. Forrest, C.S. Lent, S.A. Corcelli, J.A. Christie, K.W. Henderson, S.A. Kandel, Self-assembly of hydrogen-bonded two-dimensional quasicrystals, *Nature*, 507 (2014) 86.
- [65] P. Politzer, J.S. Murray, T. Clark, Halogen bonding: an electrostatically-driven highly directional noncovalent interaction, *Physical Chemistry Chemical Physics*, 12 (2010) 7748-7757.
- [66] S.M. Huber, J.D. Scanlon, E. Jimenez-Izal, J.M. Ugalde, I. Infante, On the directionality of halogen bonding, *Physical Chemistry Chemical Physics*, 15 (2013) 10350-10357.

- [67] A. Priimagi, G. Cavallo, P. Metrangolo, G. Resnati, The Halogen Bond in the Design of Functional Supramolecular Materials: Recent Advances, *Accounts of Chemical Research*, 46 (2013) 2686-2695.
- [68] E. Bosch, C.L. Barnes, Triangular Halogen–Halogen–Halogen Interactions as a Cohesive Force in the Structures of Trihalomesitylenes, *Crystal Growth & Design*, 2 (2002) 299-302.
- [69] H. Walch, R. Gutzler, T. Sirtl, G. Eder, M. Lackinger, Material- and Orientation-Dependent Reactivity for Heterogeneously Catalyzed Carbon-Bromine Bond Homolysis, *Journal of Physical Chemistry C*, 114 (2010) 12604-12609.
- [70] R. Gutzler, C.Y. Fu, A. Dadvand, Y. Hua, J.M. MacLeod, F. Rosei, D.F. Perepichka, Halogen bonds in 2D supramolecular self-assembly of organic semiconductors, *Nanoscale*, 4 (2012) 5965-5971.
- [71] K.W. Kolasinski, *Surface Science: Foundations of catalysis and nanoscience*, A John Wiley & Sons, LTd., Publication, 2012.
- [72] E. Umbach, M. Sokolowski, R. Fink, Substrate-interaction, long-range order, and epitaxy of large organic adsorbates, *Applied Physics a-Materials Science & Processing*, 63 (1996) 565-576.
- [73] J.V. Barth, J. Weckesser, C.Z. Cai, P. Gunter, L. Burgi, O. Jeandupeux, K. Kern, Building supramolecular nanostructures at surfaces by hydrogen bonding, *Angewandte Chemie-International Edition*, 39 (2000) 1230-1234.
- [74] F.S. Tautz, Structure and bonding of large aromatic molecules on noble metal surfaces: The example of PTCDA, *Progress in Surface Science*, 82 (2007) 479-520.
- [75] T.A. Jung, R.R. Schlittler, J.K. Gimzewski, Conformational identification of individual adsorbed molecules with the STM, *Nature*, 386 (1997) 696.
- [76] C. Liu, L. Yang, Y. Wang, S. Lei, W. Hu, Substrate Effects in the Supramolecular Self-Assembly of 2,4,6-Tris(4-bromophenyl)-1,3,5-triazine on Graphite and Graphene, *The Journal of Physical Chemistry C*, 122 (2018) 12307-12314.
- [77] D. Fujita, T. Yakabe, H. Nejoh, T. Sato, M. Iwatsuki, Scanning tunneling microscopy study on the initial adsorption behavior of C₆₀ molecules on a reconstructed Au(111)-(23 × √3) surface at various temperatures, *Surface Science*, 366 (1996) 93-98.
- [78] M. Böhringer, K. Morgenstern, W.-D. Schneider, R. Berndt, F. Mauri, A. De Vita, R. Car, Two-Dimensional Self-Assembly of Supramolecular Clusters and Chains, *Physical Review Letters*, 83 (1999) 324-327.
- [79] J. Eichhorn, T. Strunskus, A. Rastgoo-Lahrood, D. Samanta, M. Schmittel, M. Lackinger, On-surface Ullmann polymerization via intermediate organometallic networks on Ag(111), *Chem. Commun.*, 50 (2014) 7680-7682.
- [80] A. Scheybal, K. Müller, R. Bertschinger, M. Wahl, A. Bendounan, P. Aebi, T.A. Jung, Modification of the Cu(110) Shockley surface state by an adsorbed pentacene monolayer, *Phys. Rev. B*, 79 (2009) 115406.
- [81] M. Stöhr, M. Gabriel, R. Möller, Investigation of the growth of PTCDA on Cu(110): an STM study, *Surface Science*, 507-510 (2002) 330-334.
- [82] B.K. Min, X. Deng, D. Pinnaduwege, R. Schalek, C.M. Friend, Oxygen-induced restructuring with release of gold atoms from Au(111), *Phys. Rev. B*, 72 (2005) 121410.
- [83] P. Maksymovych, D.C. Sorescu, J.T. Yates, Gold-Adatom-Mediated Bonding in Self-Assembled Short-Chain Alkanethiolate Species on the Au(111) Surface, *Physical Review Letters*, 97 (2006) 146103.
- [84] A. Gourdon, On-surface covalent coupling in ultrahigh vacuum, *Angewandte Chemie-International Edition*, 47 (2008) 6950-6953.
- [85] D.F. Perepichka, F. Rosei, Extending Polymer Conjugation into the Second Dimension, *Science*, 323 (2009) 216-217.
- [86] J.W. Colson, W.R. Dichtel, Rationally synthesized two-dimensional polymers, *Nature Chemistry*, 5 (2013) 453.
- [87] S. Weigelt, C. Busse, C. Bombis, M.M. Knudsen, K.V. Gothelf, T. Strunskus, C. Wöll, M. Dahlbom, B. Hammer, E. Lægsgaard, F. Besenbacher, T.R. Linderoth, Covalent Interlinking of an Aldehyde and an Amine on a Au(111) Surface in Ultrahigh Vacuum, *Angewandte Chemie International Edition*, 46 (2007) 9227-9230.

- [88] F. Bebensee, C. Bombis, S.-R. Vadapoo, J.R. Cramer, F. Besenbacher, K.V. Gothelf, T.R. Linderoth, On-Surface Azide–Alkyne Cycloaddition on Cu(111): Does It “Click” in Ultrahigh Vacuum?, *J. Am. Chem. Soc.*, 135 (2013) 2136-2139.
- [89] H.-Y. Gao, H. Wagner, D. Zhong, J.-H. Franke, A. Studer, H. Fuchs, Glaser Coupling at Metal Surfaces, *Angewandte Chemie International Edition*, 52 (2013) 4024-4028.
- [90] A.L. Pinaridi, G. Otero-Irurueta, I. Palacio, J.I. Martinez, C. Sanchez-Sanchez, M. Tello, C. Rogero, A. Cossaro, A. Preobrajenski, B. Gómez-Lor, A. Jancarik, I.G. Stará, I. Starý, M.F. Lopez, J. Méndez, J.A. Martin-Gago, Tailored Formation of N-Doped Nanoarchitectures by Diffusion-Controlled on-Surface (Cyclo)Dehydrogenation of Heteroaromatics, *ACS Nano*, 7 (2013) 3676-3684.
- [91] S. Clair, M. Abel, L. Porte, Growth of boronic acid based two-dimensional covalent networks on a metal surface under ultrahigh vacuum, *Chem. Commun.*, 50 (2014) 9627-9635.
- [92] J.V. Barth, Fresh perspectives for surface coordination chemistry, *Surface Science*, 603 (2009) 1533-1541.
- [93] M. Di Giovannantonio, M. El Garah, J. Lipton-Duffin, V. Meunier, L. Cardenas, Y. Fagot Revurat, A. Cossaro, A. Verdini, D.F. Perepichka, F. Rosei, G. Contini, Insight into Organometallic Intermediate and Its Evolution to Covalent Bonding in Surface-Confined Ullmann Polymerization, *ACS Nano*, 7 (2013) 8190-8198.
- [94] Q. Fan, C. Wang, Y. Han, J. Zhu, J. Kuttner, G. Hilt, J.M. Gottfried, Surface-Assisted Formation, Assembly, and Dynamics of Planar Organometallic Macrocycles and Zigzag Shaped Polymer Chains with C–Cu–C Bonds, *ACS Nano*, 8 (2014) 709-718.
- [95] E.C.H. Sykes, P. Han, S.A. Kandel, K.F. Kelly, G.S. McCarty, P.S. Weiss, Substrate-Mediated Interactions and Intermolecular Forces between Molecules Adsorbed on Surfaces, *Accounts of Chemical Research*, 36 (2003) 945-953.
- [96] H. von Schenck, J. Weissenrieder, S. Helldén, B. Åkermark, M. Göthelid, Reactions of iodobenzene on Pd(1 1 1) and Pd(1 1 0), *Applied Surface Science*, 212-213 (2003) 508-514.
- [97] M. Bieri, M.T. Nguyen, O. Groning, J.M. Cai, M. Treier, K. Ait-Mansour, P. Ruffieux, C.A. Pignedoli, D. Passerone, M. Kastler, K. Mullen, R. Fasel, Two-Dimensional Polymer Formation on Surfaces: Insight into the Roles of Precursor Mobility and Reactivity, *J. Am. Chem. Soc.*, 132 (2010) 16669-16676.
- [98] S. Schlogl, W.M. Heckl, M. Lackinger, On-surface radical addition of triply iodinated monomers on Au(111)-the influence of monomer size and thermal post-processing, *Surface Science*, 606 (2012) 999-1004.
- [99] M. Bieri, S. Blankenburg, M. Kivala, C.A. Pignedoli, P. Ruffieux, K. Müllen, R. Fasel, Surface-supported 2D heterotriangulene polymers, *Chem. Commun.*, 47 (2011) 10239-10241.
- [100] A. Saywell, W. Greñ, G. Franc, A. Gourdon, X. Bouju, L. Grill, Manipulating the Conformation of Single Organometallic Chains on Au(111), *The Journal of Physical Chemistry C*, 118 (2014) 1719-1728.
- [101] F. Ullmann, J. Bielecki, Ueber Synthesen in der Biphenylreihe, *Berichte der deutschen chemischen Gesellschaft*, 34 (1901) 2174-2185.
- [102] M.M. Blake, S.U. Nanayakkara, S.A. Claridge, L.C. Fernández-Torres, E.C.H. Sykes, P.S. Weiss, Identifying Reactive Intermediates in the Ullmann Coupling Reaction by Scanning Tunneling Microscopy and Spectroscopy, *The Journal of Physical Chemistry A*, 113 (2009) 13167-13172.
- [103] J. Björk, F. Hanke, S. Stafström, Mechanisms of Halogen-Based Covalent Self-Assembly on Metal Surfaces, *J. Am. Chem. Soc.*, 135 (2013) 5768-5775.
- [104] G. Landauer, Generation of harmonics of the electron-gyrofrequency in a penning discharge, *J. Nucl. Energy, Part C Plasma Phys*, 4 (1962) 395.
- [105] M.K. K. Oura, A. V. Zotov, V. G. Lifshits, A. A. Saranin, *Surface Science - An Introduction*, Springer-Verlag, 2004.
- [106] J.C. Vickerman, I.S. Gilmore, *Surface Analysis – The Principal Techniques*, 2nd Edition, John Wiley & Sons, Ltd., 2009.
- [107] M.P. Seah, W.A. Dench, Quantitative electron spectroscopy of surfaces: A standard data base for electron inelastic mean free paths in solids, *Surface and Interface Analysis*, 1 (1979) 2-11.

- [108] D.P. Woodruff, T.A. Delchar, *Modern Techniques of Surface Science - Second Edition*, The Press Syndicate of The University of Cambridge, Cambridge, 1994.
- [109] R.J. Hamers, *Atomic-Resolution Surface Spectroscopy with the Scanning Tunneling Microscope*, 40 (1989) 531-559.
- [110] C.J. Chen, *Introduction to Scanning Tunneling Microscopy*, Oxford University Press, 1993.
- [111] F. Besenbacher, *Scanning tunnelling microscopy studies of metal surfaces*, *Reports on Progress in Physics*, 59 (1996) 1737-1802.
- [112] H. Neddermeyer, *Scanning tunnelling microscopy of semiconductor surfaces*, *Reports on Progress in Physics*, 59 (1996) 701-769.
- [113] R. Wiesendanger, *Scanning Probe Microscopy and Spectroscopy: Methods and Applications*, First ed., The Press Syndicate of The University of Cambridge, Cambridge, 1994.
- [114] C.J. Chen, *Introduction to Scanning Tunneling Microscopy*, Second Edition ed., Oxford University Press; 2008.
- [115] J. Tersoff, D.R. Hamann, *THEORY OF THE SCANNING TUNNELING MICROSCOPE*, *Phys. Rev. B*, 31 (1985) 805-813.
- [116] J. Bardeen, *Tunnelling from a many-particle point of view*, *Physical Review Letters*, 6 (1961) 57-59.
- [117] R.G. Parr, Y. Weitao, *Density-functional theory of atoms and molecules*, Oxford University Press, 1989.
- [118] R. Gatti, J.M. MacLeod, J.A. Lipton-Duffin, A.G. Moiseev, D.F. Perepichka, F. Rosei, *Substrate, Molecular Structure, and Solvent Effects in 2D Self-Assembly via Hydrogen and Halogen Bonding*, *Journal of Physical Chemistry C*, 118 (2014) 25505-25516.
- [119] M. J. Frisch, G. W. Trucks, H. B. Schlegel, G. E. Scuseria, M. A. Robb, J. R. Cheeseman, G. Scalmani, V. Barone, G. A. Petersson, H. Nakatsuji, X. Li, M. Caricato, A. V. Marenich, J. Bloino, B. G. Janesko, R. Gomperts, B. Mennucci, H. P. Hratchian, J. V. Ortiz, A. F. Izmaylov, J. L. Sonnenberg, D. Williams-Young, F. Ding, F. Lipparini, F. Egidi, J. Goings, B. Peng, A. Petrone, T. Henderson, D. Ranasinghe, V. G. Zakrzewski, J. Gao, N. Rega, G. Zheng, W. Liang, M. Hada, M. Ehara, K. Toyota, R. Fukuda, J. Hasegawa, M. Ishida, T. Nakajima, Y. Honda, O. Kitao, H. Nakai, T. Vreven, K. Throssell, J. J. A. Montgomery, J. E. Peralta, F. Ogliaro, M. J. Bearpark, J. J. Heyd, E. N. Brothers, K. N. Kudin, V. N. Staroverov, T. A. Keith, R. Kobayashi, J. Normand, K. Raghavachari, A. P. Rendell, J. C. Burant, S. S. Iyengar, J. Tomasi, M. Cossi, J. M. Millam, M. Klene, C. Adamo, R. Cammi, J. W. Ochterski, R. L. Martin, K. Morokuma, O. Farkas, J. B. Foresman, D. J. Fox, *Gaussian 09*, revision B.01; Gaussian, Inc.: Wallingford, CT, 2009.
- [120] J.P. Perdew, K. Burke, M. Ernzerhof, *Generalized Gradient Approximation Made Simple*, *Physical Review Letters*, 77 (1996) 3865-3868.
- [121] P.J. Hay, W.R. Wadt, *Ab initio effective core potentials for molecular calculations. Potentials for the transition metal atoms Sc to Hg*, *The Journal of Chemical Physics*, 82 (1985) 270-283.
- [122] P.J. Hay, W.R. Wadt, *Ab initio effective core potentials for molecular calculations. Potentials for K to Au including the outermost core orbitals*, *The Journal of Chemical Physics*, 82 (1985) 299-310.
- [123] W.R. Wadt, P.J. Hay, *Ab initio effective core potentials for molecular calculations. Potentials for main group elements Na to Bi*, *The Journal of Chemical Physics*, 82 (1985) 284-298.
- [124] T.A. Keith, *TK Gristmill Software*, Overland Park KS, USA, 2019.
- [125] D.Y. Petrovykh, K.N. Altmann, J.L. Lin, F.J. Himpsel, F.M. Leibsle, *Single domain Ca-induced reconstruction on vicinal Si(111)*, *Surface Science*, 512 (2002) 269-280.
- [126] J.L. Lin, D.Y. Petrovykh, J. Viernow, F.K. Men, D.J. Seo, F.J. Himpsel, *Formation of regular step arrays on Si(111)7x7*, *Journal of Applied Physics*, 84 (1998) 255-260.
- [127] Y. Cao, K.S. Yong, Z.Q. Wang, W.S. Chin, Y.H. Lai, J.F. Deng, G.Q. Xu, *Dry thienylation of the silicon (111)-(7 x 7) surface*, *J. Am. Chem. Soc.*, 122 (2000) 1812-1813.
- [128] J.B. Gustafsson, H.M. Zhang, L.S.O. Johansson, *STM studies of thin PTCDA films on Ag/Si(111)-root 3x root 3*, *Phys. Rev. B*, 75 (2007) 7.

- [129] T. Suzuki, T. Lutz, G. Costantini, K. Kern, Terephthalic acid adsorption on Si(111)-($\sqrt{3} \times \sqrt{3}$)-Bi surfaces: Effect of Bi coverage, *Surface Science*, 605 (2011) 1994-1998.
- [130] S.R. Wagner, P.P. Zhang, Nucleation and evolution of zinc phthalocyanine thin films on the deactivated Si(111)- $\sqrt{3} \times \sqrt{3}$ R30 degrees surface, *Surface Science*, 630 (2014) 22-27.
- [131] A. Rochefort, Y. Makoudi, A. Maillard, J. Jeannoutot, J. Blier, F. Cherioux, F. Palmino, Anisotropic growth of the thiophene-based layer on Si(111)-B, *Chem. Commun.*, 50 (2014) 5484-5486.
- [132] T. Yokoyama, M. Kawasaki, T. Asari, S. Ohno, M. Tanaka, Y. Yoshimoto, Adsorption and self-assembled structures of sexithiophene on the Si(111)- 3×3 -Ag surface, *The Journal of Chemical Physics*, 142 (2015) 204701.
- [133] M. El Garah, J. Lipton-Duffin, J.M. MacLeod, R. Gutzler, F. Palmino, V. Luzet, F. Cherioux, F. Rosei, Self-Assembly of a Halogenated Molecule on Oxide-Passivated Cu(110), *Chem.-Asian J.*, 8 (2013) 1813-1817.
- [134] Q.T. Fan, C.C. Wang, L.M. Liu, Y. Han, J. Zhao, J.F. Zhu, J. Kuttner, G. Hilt, J.M. Gottfried, Covalent, Organometallic, and Halogen-Bonded Nanomeshes from Tetrabromo-Terphenyl by Surface-Assisted Synthesis on Cu(111), *Journal of Physical Chemistry C*, 118 (2014) 13018-13025.
- [135] Y. Zhang, Y. Zhang, G. Li, J. Lu, X. Lin, Y. Tan, X. Feng, S. Du, K. Müllen, H.-J. Gao, Construction of single-crystalline supramolecular networks of perchlorinated hexa-peri-hexabenzocoronene on Au(111), *The Journal of Chemical Physics*, 142 (2015) 101911.
- [136] Q. Fan, T. Wang, L. Liu, J. Zhao, J. Zhu, J.M. Gottfried, Tribromobenzene on Cu(111): Temperature-dependent formation of halogen-bonded, organometallic, and covalent nanostructures, *The Journal of Chemical Physics*, 142 (2015) 101906.
- [137] R. Gutzler, O. Ivasenko, C.Y. Fu, J.L. Brusso, F. Rosei, D.F. Perepichka, Halogen bonds as stabilizing interactions in a chiral self-assembled molecular monolayer, *Chem. Commun.*, 47 (2011) 9453-9455.
- [138] F. Silly, Selecting Two-Dimensional Halogen Halogen-Bonded Self-Assembled 1,3,5-Tris(4-iodophenyl)benzene Porous Nanoarchitectures at the Solid-Liquid Interface, *Journal of Physical Chemistry C*, 117 (2013) 20244-20249.
- [139] W. Song, N. Martsinovich, W.M. Heckl, M. Lackinger, Thermodynamics of halogen bonded monolayer self-assembly at the liquid–solid interface, *Chem. Commun.*, 50 (2014) 13465-13468.
- [140] Y. Makoudi, M. Beyer, J. Jeannoutot, F. Picaud, F. Palmino, F. Cherioux, Supramolecular self-assembly of brominated molecules on a silicon surface, *Chem. Commun.*, 50 (2014) 5714-5716.
- [141] R.D. McCullough, The chemistry of conducting polythiophenes, *Adv. Mater.*, 10 (1998) 93-116.
- [142] P. He, Z. Tu, G. Zhao, Y. Zhen, H. Geng, Y. Yi, Z. Wang, H. Zhang, C. Xu, J. Liu, X. Lu, X. Fu, Q. Zhao, X. Zhang, D. Ji, L. Jiang, H. Dong, W. Hu, Tuning the Crystal Polymorphs of Alkyl Thienoacene via Solution Self-Assembly Toward Air-Stable and High-Performance Organic Field-Effect Transistors, *Adv. Mater.*, 27 (2015) 825-830.
- [143] Y. Miyata, E. Yoshikawa, T. Minari, K. Tsukagoshi, S. Yamaguchi, High-performance organic field-effect transistors based on dihexyl-substituted dibenzo d,d ' thieno 3,2-b;4,5-b ' dithiophene, *J. Mater. Chem.*, 22 (2012) 7715-7717.
- [144] C.L. Wang, H.L. Dong, W.P. Hu, Y.Q. Liu, D.B. Zhu, Semiconducting pi-Conjugated Systems in Field-Effect Transistors: A Material Odyssey of Organic Electronics, *Chem. Rev.*, 112 (2012) 2208-2267.
- [145] J.L. Brusso, O.D. Hirst, A. Dadvand, S. Ganesan, F. Cicoira, C.M. Robertson, R.T. Oakley, F. Rosei, D.F. Perepichka, Two-dimensional structural motif in thienoacene semiconductors: Synthesis, structure, and properties of tetrathienoanthracene isomers, *Chemistry of Materials*, 20 (2008) 2484-2494.
- [146] L. Cardenas, R. Gutzler, J. Lipton-Duffin, C. Fu, J.L. Brusso, L.E. Dinca, M. Vondráček, Y. Fagot-Revurat, D. Malterre, F. Rosei, D.F. Perepichka, Synthesis and electronic structure of a two dimensional π -conjugated polythiophene, *Chem. Sci.*, 4 (2013) 3263-3268.
- [147] J. Viernow, J.-L. Lin, D.Y. Petrovykh, F.M. Leibsle, F.K. Men, F.J. Himpsel, Regular step arrays on silicon, *Applied Physics Letters*, 72 (1998) 948-950.

- [148] X. Lu, X.L. Wang, Q.H. Yuan, Q. Zhang, Diradical mechanisms for the cycloaddition reactions of 1,3-butadiene, benzene, thiophene, ethylene, and acetylene on a Si(111)-7x7 surface, *J. Am. Chem. Soc.*, 125 (2003) 7923-7929.
- [149] M. Schunack, E. Lægsgaard, I. Stensgaard, F. Besenbacher, Bonding and ordering of decacyclene molecules on Cu(110) studied by scanning tunneling microscopy, *The Journal of Chemical Physics*, 117 (2002) 8493-8498.
- [150] E.A. Lewis, C.J. Murphy, M.L. Liriano, E.C.H. Sykes, Atomic-scale insight into the formation, mobility and reaction of Ullmann coupling intermediates, *Chem. Commun.*, 50 (2014) 1006-1008.
- [151] M. Chen, J. Xiao, H.-P. Steinrück, S. Wang, W. Wang, N. Lin, W. Hieber, J.M. Gottfried, Combined Photoemission and Scanning Tunneling Microscopy Study of the Surface-Assisted Ullmann Coupling Reaction, *The Journal of Physical Chemistry C*, 118 (2014) 6820-6830.
- [152] G. Galeotti, Two-dimensional polymer formation upon metallic surfaces with low Miller index, Faculty of Science, University of Rome Tor Vergata (Master dissertation). Rome, Italy, 2012.
- [153] N. Chakravarthi, U.K. Aryal, K. Gunasekar, H.-Y. Park, Y.-S. Gal, Y.-R. Cho, S.I. Yoo, M. Song, S.-H. Jin, Triazine-based Polyelectrolyte as an Efficient Cathode Interfacial Material for Polymer Solar Cells, *ACS Applied Materials & Interfaces*, 9 (2017) 24753-24762.
- [154] J.A. Lipton-Duffin, O. Ivasenko, D.F. Perepichka, F. Rosei, Synthesis of Polyphenylene Molecular Wires by Surface-Confined Polymerization, *Small*, 5 (2009) 592-597.
- [155] G.S. McCarty, P.S. Weiss, Formation and Manipulation of Protopolymer Chains, *J. Am. Chem. Soc.*, 126 (2004) 16772-16776.
- [156] B.E. Bent, Mimicking Aspects of Heterogeneous Catalysis: Generating, Isolating, and Reacting Proposed Surface Intermediates on Single Crystals in Vacuum, *Chem. Rev.*, 96 (1996) 1361-1390.
- [157] F. De Marchi, G. Galeotti, M. Simenas, M.C. Gallagher, E. Hamzehpoor, D. Dettmann, G. Contini, M. Ebrahimi, E. E. Tornau, D.F. Perepichka, F. Rosei, Supramolecular Ordering of a Heterotriangulene molecule on Au(111) DOI (To be published).
- [158] F. De Marchi, G. Galeotti, E. Hamzehpoor, O. MacLean, D. Dettmann, N. Preetha Genesh, L. V. Besteiro, R. Liu, R. M. Rao, Y. Chen, L. Ferrari, F. Frezza, P. M. Sheverdyeva, A.K. Kundu, P. Moras, M. Ebrahimi, M.C. Gallagher, G. Contini, D.F. Perepichka, F. Rosei, Energy-band dispersions of a mesoscale porous 2D graphene-like polymer obtained by on-surface polymerization, DOI (To be published).
- [159] H.S. Taylor, E.F. Armstrong, A theory of the catalytic surface, *Proceedings of the Royal Society of London. Series A, Containing Papers of a Mathematical and Physical Character*, 108 (1925) 105-111.
- [160] G. Ertl, H. Knözinger, F. Schuth, J. Weitkamp, *Handbook of Heterogeneous Catalysis*, Wiley-VCH, 2008.
- [161] G.A. Somorjai, The surface science of heterogeneous catalysis, *Surface Science*, 299-300 (1994) 849-866.
- [162] J.T.Y. Jr., Surface chemistry at metallic step defect sites, *Journal of Vacuum Science & Technology A*, 13 (1995) 1359-1367.
- [163] Y. Makoudi, B. Baris, J. Jeannoutot, F. Palmino, B. Grandidier, F. Cherioux, Tailored Molecular Design for Supramolecular Network Engineering on a Silicon Surface, *Chemphyschem*, 14 (2013) 900-904.
- [164] G. Copie, F. Cleri, Y. Makoudi, C. Krzeminski, M. Berthe, F. Cherioux, F. Palmino, B. Grandidier, Surface-Induced Optimal Packing of Two-Dimensional Molecular Networks, *Physical Review Letters*, 114 (2015) 066101.
- [165] G. Copie, Y. Makoudi, C. Krzeminski, F. Chérioux, F. Palmino, S. Lamare, B. Grandidier, F. Cleri, Atomic Scale Modeling of Two-Dimensional Molecular Self-Assembly on a Passivated Si Surface, *The Journal of Physical Chemistry C*, 118 (2014) 12817-12825.
- [166] J.M. Cai, P. Ruffieux, R. Jaafar, M. Bieri, T. Braun, S. Blankenburg, M. Muoth, A.P. Seitsonen, M. Saleh, X.L. Feng, K. Mullen, R. Fasel, Atomically precise bottom-up fabrication of graphene nanoribbons, *Nature*, 466 (2010) 470-473.
- [167] Y. Jin, C. Yu, R.J. Denman, W. Zhang, Recent advances in dynamic covalent chemistry, *Chemical Society Reviews*, 42 (2013) 6634-6654.

- [168] J.-M. Lehn, Dynamic Combinatorial Chemistry and Virtual Combinatorial Libraries, *Chemistry – A European Journal*, 5 (1999) 2455-2463.
- [169] B.L. Miller, *Dynamic Combinatorial Chemistry in Drug Discovery, Bioorganic Chemistry, and Materials Science*, Wiley, Hoboken, 2009, pp. 1-42.
- [170] P.T. Corbett, J. Leclaire, L. Vial, K.R. West, J.-L. Wietor, J.K.M. Sanders, S. Otto, *Dynamic Combinatorial Chemistry*, *Chem. Rev.*, 106 (2006) 3652-3711.
- [171] C.-Z. Guan, D. Wang, L.-J. Wan, Construction and repair of highly ordered 2D covalent networks by chemical equilibrium regulation, *Chem. Commun.*, 48 (2012) 2943-2945.